Deformation Mechanisms in Pure and Alloyed Copper Films

Von der Fakultät Chemie der Universität Stuttgart
zur Erlangung der Würde eines Doktors der Naturwissenschaften
(Dr. rer. nat.) genehmigte Abhandlung

vorgelegt von

Dirk Weiss

aus Kapstadt

Hauptberichter: Prof. Dr. phil. E. Arzt
Mitberichter: Prof. Dr. rer. nat. F. Aldinger
Tag der mündlichen Prüfung: 28. Juli 2000

Max-Planck-Institut für Metallforschung und
Institut für Metallkunde der Universität Stuttgart

2000

Dirk Weiss

Deformation Mechanisms in Pure and Alloyed Copper Films

157 pages, 76 figures, 12 tables

Abstract

In this work, the evolution of microstructure and the thermo-mechanical behavior of copper and dilute copper alloy thin films was investigated. 0.3 to 2.0 µm thick films were deposited by magnetron sputtering under ultra high vacuum conditions onto diffusion-barrier coated silicon substrates and subjected to wafer curvature measurements.

Pure copper films annealed in ultra high vacuum exhibited a large grain size, a sharp (111) texture, and very few twin grains. Grain growth in the single-phase copper-aluminum system was similar to that in pure copper films; abnormal grain growth and inhibition of normal grain growth was observed in the two-phase copper-yttrium system.

The thermal stress evolution in pure copper films was described for the first time with a constitutive law for diffusional creep in a thin film under the constraint of a substrate. Diffusional creep was suppressed by aluminum alloying. This was accounted for by the inhibition of surface diffusion due to a segregation layer of aluminum oxide. Creep voiding occurred in oxidized copper-aluminum alloy films. Creep voiding, which was observed for the first time in a two-dimensional grain structure, was ascribed to the high thermal stresses, which cannot be avoided in the heat treatment of metal films on silicon substrates.

Max-Planck-Institut für Metallforschung und Institut für Metallkunde der Universität Stuttgart, 2000

Alle Rechte, auch das des auszugsweisen Nachdrucks, der auszugsweisen oder vollständigen Wiedergabe (Fotokopie, Mikroskopie), der Speicherung in Datenverarbeitungsanlagen und das der Übersetzung, vorbehalten.

Als Manuskript gedruckt. Printed in Germany.

Dirk Weiss

Verformungsmechanismen in reinen und legierten Kupferschichten

Kurzzusammenfassung

In dieser Arbeit wurden die Gefügeentwicklung und das thermomechanische Verhalten dünner Kupfer und Kupferlegierungsschichten untersucht. Die 0.3 bis 2.0 µm dicken Schichten wurden mittels Magnetronsputtern unter Ultrahochvakuumbedingungen auf Siliziumsubstrate abgeschieden, die mit einer amorphen Diffusionsbarriere beschichtet waren. Die mechanischen Eigenschaften wurden mit der Substratkrümmungsmethode gemessen.

Das Gefüge reiner, im Ultrahochvakuum ausgelagerter Kupferschichten war durch eine große Korngröße, eine scharfe (111)-Textur und eine geringe Dichte an Zwillingskörnern gekennzeichnet. Das einphasige System Kupfer-Aluminium zeigte das gleiche Kornwachstum wie reine Kupferschichten, während abnormales Kornwachstum und Unterdrückung des normalen Kornwachstums im zweiphasigen System Kupfer-Yttrium beobachtet wurde.

Die thermische Spannungsentwicklung in reinen Kupferschichten konnte in dieser Arbeit zum ersten Mal mit einem Kriechgesetz beschrieben werden, welches sowohl die Geometrie als auch die Haftung der dünnen Schicht auf dem Substrat berücksichtigt. Das Diffusionskriechen konnte gezielt durch das Legieren mit Aluminium unterdrückt werden. Dieses wurde mit der Hemmung der Oberflächendiffusion durch eine Segregationsschicht aus Aluminiumoxid erklärt. Die hohen thermischen Spannungen, die bei der Wärmebehandlung dünner Metallschichten auf Siliziumsubstraten entstehen, wurden für die Schädigung von Korngrenzen in Kupfer-Aluminium-Legierungsschichten durch Kriechporen verantwortlich gemacht. Kriechporen wurden dabei erstmalig in einem zweidimensionalen Gefüge beobachtet.

Danksagung

Die vorliegende Doktorarbeit wurde in der Zeit zwischen Januar 1997 und Mai 2000 am Max-Planck-Institut für Metallforschung in Stuttgart angefertigt. Herrn Prof. Dr. E. Arzt danke ich für die Aufnahme in seine Arbeitsgruppe und für die Stellung eines Promotionsthemas, das die Verbindung von Grundlagenforschung und anwendungsbezogenem Arbeiten ermöglicht hat. Ich danke ihm außerdem für die vielen Diskussionen, die ganz wesentlich zum Gelingen der Arbeit beigetragen haben.

Herrn Prof. Dr. F. Aldinger danke ich für die freundliche Übernahme des Mitberichts.

Herrn Prof. Dr. H. Gao von der Stanford University danke ich für die fruchtbare Zusammenarbeit, deren Ergebnisse einem wichtigen Teil dieser Arbeit zugrunde liegen.

Für die Hilfen, Anregungen und Diskussionen bin ich Frau Dr. Julie Nucci und den Herren Dr. Gerhard Dehm, Dr. Peter Gumbsch, Dr. Oliver Kraft und Dr. Peter Müllner dankbar.

Ich danke den Serviceeinrichtungen und Technikern des Instituts für Unterstützung bei der experimentellen Arbeit, von denen ich vor allem Herrn Gerhard Adam erwähnen möchte.

Schließlich bedanke ich mich bei allen Mitgliedern der Abteilung Arzt für die angenehme und kooperative Arbeitsatmosphäre.

Contents

1 INTRODUCTION **1**

2 LITERATURE REVIEW **4**

2.1 PROCESSING AND MICROSTRUCTURE OF THIN METAL FILMS **4**
2.1.1 SPUTTERING 4
2.1.2 MICROSTRUCTURE EVOLUTION IN PURE METAL FILMS 5
2.2 MECHANICAL PROPERTIES OF THIN METAL FILMS **7**
2.2.1 STRAIN AND STRESS IN THIN FILMS 7
2.2.2 THE YIELD STRESS OF THIN FILMS 9
2.2.3 MODELING OF FILM STRESS EVOLUTION DURING THERMAL CYCLING 11
2.3 MICROSTRUCTURE AND MECHANICAL PROPERTIES OF ALLOY FILMS **14**
2.3.1 MECHANICAL PROPERTIES OF DISPERSION STRENGTHENED BULK ALLOYS 14
2.3.2 GRAIN GROWTH IN THE PRESENCE OF PARTICLES 17
2.3.3 PROCESSING OF DISPERSION STRENGTHENED THICK FILMS 18
2.3.4 INTERNAL OXIDATION: THE CU-AL SYSTEM 20
2.4 SUMMARY OF THE LITERATURE AND AIMS OF THIS WORK **22**

3 EXPERIMENT **24**

3.1 FILM SYNTHESIS **24**
3.1.1 UHV SPUTTERING SYSTEM 24
3.1.2 UHV FILM SYNTHESIS: CU AND CU-AL 26
3.1.3 HV FILM SYNTHESIS: CU-Y 28
3.2 MICROSTRUCTURAL CHARACTERIZATION **28**
3.3 MECHANICAL AND ELECTRICAL CHARACTERIZATION **31**

4 RESULTS 34

4.1 PURE CU FILMS: MICROSTRUCTURE EVOLUTION 34
4.1.1 UHV-ANNEALED FILMS 34
4.1.2 HV-ANNEALED FILMS 44
4.2 PURE CU FILMS: MECHANICAL PROPERTIES 45
4.2.1 UHV-ANNEALED FILMS 45
4.2.2 HV-ANNEALED FILMS 49
4.3 CU-AL FILMS: MICROSTRUCTURE EVOLUTION 52
4.3.1 UHV-ANNEALED AND OXIDIZED FILMS 52
4.3.2 HV-ANNEALED FILMS AND REACTIVELY SPUTTERED FILMS 63
4.4 CU-AL FILMS: MECHANICAL PROPERTIES 65
4.4.1 UHV-ANNEALED AND OXIDIZED FILMS 65
4.4.2 HV-ANNEALED FILMS AND REACTIVELY SPUTTERED FILMS 70
4.5 CU-1AT.%Y FILMS: MICROSTRUCTURE EVOLUTION 74
4.6 SUMMARY OF THE RESULTS 77

5 DISCUSSION 79

5.1 MICROSTRUCTURE DEVELOPMENT IN CU, CU-AL AND CU-Y FILMS 79
5.1.1 PURE CU FILMS 79
5.1.2 CU-AL FILMS 82
5.1.3 CU-Y FILMS 85
5.2 THERMO-MECHANICAL BEHAVIOR OF CU AND CU-AL ALLOY FILMS 88
5.2.1 STRESS RELAXATION BY DISLOCATION GLIDE (AL-TYPE) 89
5.2.2 STRESS RELAXATION BY CONSTRAINED DIFFUSIONAL CREEP (UHV CU-TYPE) 93
5.2.3 THE VACUUM QUALITY EFFECT (HV CU-TYPE) 112
5.3 YIELD STRESS OF CU THIN FILMS 115
5.3.1 THE FILM THICKNESS EFFECT ON YIELD STRESS 115
5.3.2 ISOTHERMAL STRESS RELAXATION EXPERIMENTS 119
5.3.3 THE ROLE OF DISLOCATION SOURCES FOR THE YIELD STRESS OF THIN FILMS 124
5.4 GRAIN BOUNDARY VOIDS IN OXIDIZED CU-AL ALLOY FILMS 129

6 SUMMARY AND CONCLUSIONS 134

LITERATURE 139

APPENDIX **145**

A: Thermoelastic data for Cu on Si **145**

B: Modeling constrained diffusional creep **147**

C: List of Cu and Cu-Al films **152**

D: List of symbols **154**

1 Introduction

The miniaturization of electronic devices in the last decades would not have been achieved without thin film technology. As an essential component, thin metal lines, which interconnect tens of millions of transistors on a microchip, are “cut” out of thin metal films deposited onto the wafer. However, the different thermal expansions of the various materials in a microchip give rise to high mechanical stresses in these components. For example, an increase in temperature of only 30 K leads to a stress of 100 MPa in a copper thin film firmly attached to a silicon wafer – which is equivalent to a pressure of 1000 kg per cm^2. Much higher temperature changes occur during fabrication and operation of a microchip, which produces even larger thermal stresses. These stresses can provoke delamination and cracking of films and are therefore considered a serious reliability issue in modern semiconductor industry.

Understanding and controlling mechanical properties of films is not only a fundamental challenge for the rapidly growing semiconductor industry, but it is also a leading-edge topic in materials research. Academic interest is due to the observation that the mechanical properties of geometrically constrained materials, such as thin films, often differ significantly from the bulk properties. The mechanical behavior of a material depends on its microstructure. The microstructure describes the arrangement of defects on a microscopic length scale, far below the macroscopic dimensions of bulk samples. In thin films, however, the thickness is often below the length scale of the defects which constitute the microstructure. As a consequence, the surface of the film and the interface between the film and the substrate increasingly influence the processes which determine the mechanical behavior of the films. This dimensional effect is illustrated for three types of defects in the following.

In a bulk metal, grain boundaries are arranged in a cell-like structure comparable to soap in a soap froth, which is schematically shown in Figure 1-1 (a). A grain boundary is a plane separating two regions of different crystallographic orientation from one another. The order of the atoms in a grain boundary is disturbed compared to the crystal lattice.

Therefore, the motion of atomic vacancies is more easily achieved in the grain boundary than through the undisturbed lattice. For this reason, grain boundaries play an important role in the deformation of a material at high temperature, which is associated with a directional motion of these vacancies. In a thin film, grain boundaries usually extend from the surface, where they are “trapped” by little grooves, to the film/substrate interface (see Figure 1-1 b). Due to this specific geometry, new paths for vacancy motion along the interfaces – both the interface between film and substrate and the film surface – emerge. Thus, the properties of the interface and the surface will become important for particular characteristics of the high-temperature deformation of a thin film.

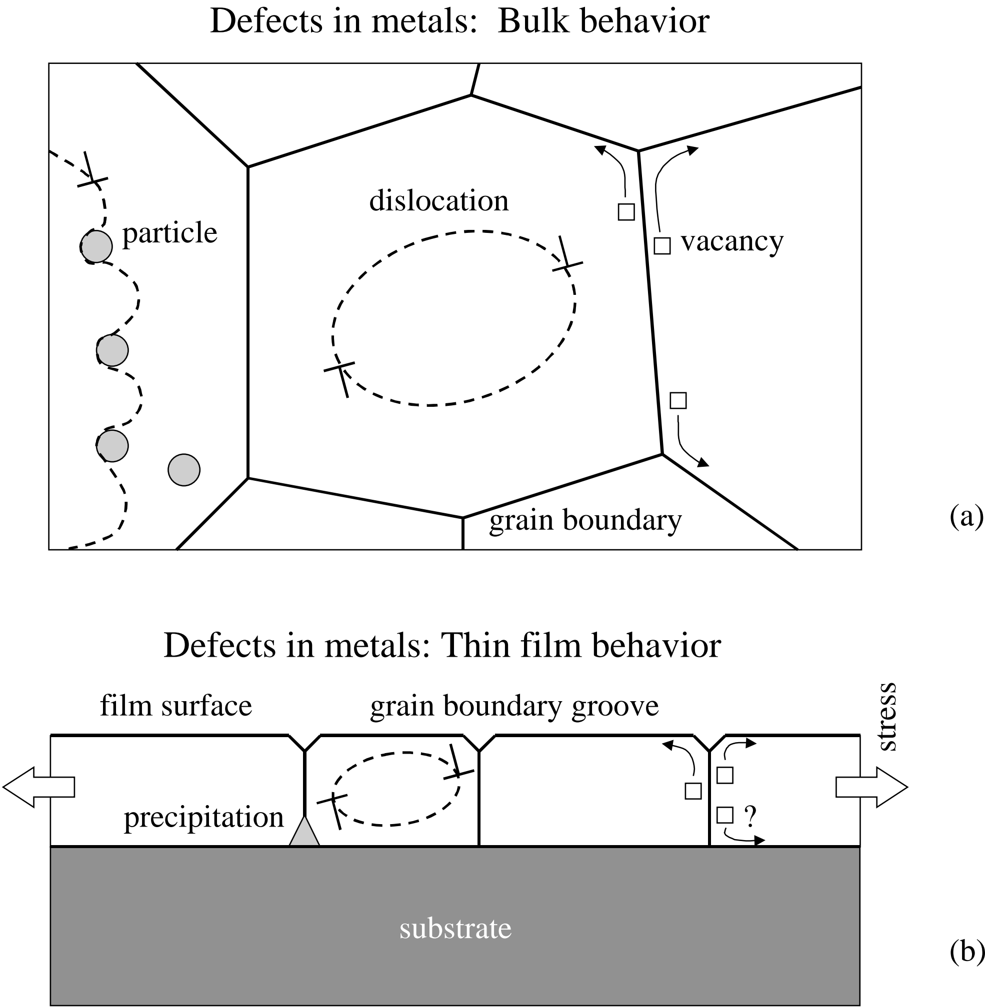

Figure 1-1 Defects in metals: Bulk behavior (a) versus thin film behavior (b). Surface and interface become important in the evolution of microstructure and in the mechanical behavior of thin films.

Another observation is that thin films are commonly stronger than bulk materials. This behavior is related to another class of defects, the dislocations. In a thin film, dislocation motion is confined by the limited extension of the film in the direction perpendicular to the film plane. The increased strength of a thin film is attributed to this dimensional effect; however, the particular role of surfaces and interfaces is still not understood.

A third aspect, which will be addressed in this work, are alloying effects in small di-mensions. For most engineering purposes, metals must be alloyed because pure metals are usually too soft. One common alloying route consists of the reinforcement of the metallic matrix by small second-phase particles. The working principle, which is shown in Figure 1-1 (a), consists of the obstruction of dislocation motion by the particles. However, alloy-ing strategies successfully applied in many bulk metals can fail in thin films. Second phases have been observed to precipitate at the film/substrate interface where they become inactive as obstacles for dislocation motion (Figure 1-1 b). Also in this case, interfaces are responsible for the distinct behavior of a thin film.

To date, the application of alloying methods to thin films is discussed only in a few publications. It is expected that "alloying in small dimensions" will gain importance in in-dustry and research as the trend for miniaturization extends to other areas, such as me-chanical engineering, chemical synthesis and analysis, and bio-medical applications, where new thin-film materials with improved performance are needed.

A thin film system with high technical relevancy is copper. Copper is characterized by a high thermal and electrical conductivity. Thanks to these advantageous material qualities, copper is replacing aluminum as interconnect material in electronic microchips since 1998. In this work, the effect of film geometry on the deformation mechanisms in pure and al-loyed copper films is investigated. Pure copper films are produced for the first time by magnetron sputtering under ultra high vacuum conditions. The microstructure evolution in copper and dilute copper-aluminum and copper-yttrium films is investigated. In chapter 2 the literature on microstructure and mechanical properties of pure and alloyed thin metal films is reviewed. In chapter 3 the experimental techniques applied in this work are pre-sented. Chapter 4 gives a detailed record of all experimental results. The results are dis-cussed in chapter 5, focusing on the mechanical behavior of pure Cu and Cu-Al alloy films. The main result of this work is discussed in section 5.2. Namely, the first clear iden-tification of diffusional creep in a thin film under the constraint of the substrate adhesion is discussed. A detailed summary is found in chapter 6.

2 Literature review

Many laws governing bulk material behavior cease to apply as one sample dimension becomes very small in a thin film. Thin film behavior has been intensely researched in the last decades and deviations from bulk behavior have been analyzed. In section 2.1 the literature on microstructure evolution in thin films is reviewed. In section 2.2 the literature on strengthening and stress relaxation mechanisms in thin films is critically discussed. It is focused on the properties of pure fcc metal films on Si substrates. Section 2.3 gives an overview of dispersion strengthening in bulk alloys and thick alloy films.

2.1 Processing and microstructure of thin metal films

2.1.1 Sputtering

Sputtering is an important means for the fabrication of thin solid films, both in basic research and in industry. A good overview of film deposition methods is given in Ohring (1992). In general, sputtering is carried out in a vacuum chamber. Atoms are sputtered from a target by the momentum transfer of ionized sputtering gas atoms, mostly noble gases, which are accelerated onto the target. The sputtered target atoms condense on a substrate located vis-à-vis the substrate. Unlike thermal evaporation, sputtering is a cold process. No crucible is required for the material to be deposited. Sputtering is exceptionally suitable for the deposition of alloys. It can be shown that the chemical composition of a sputtered film very closely resembles the composition of the target.

Sputtering became important for industrial application after 1975 (Haefer 1987) when magnetrons came into use, which are very efficient sputtering sources. In this technique, which was also applied in this work, a noble gas plasma is ignited in the chamber; a strong magnetic field perpendicular to the target surface confines electron movement and thus concentrates the plasma to the region in front of the target. It allows for sputtering with

high deposition rates at low working gas pressures. Finally, reactive sputtering is mentioned as an important means for the fabrication of compound films, e.g. TiC or TiN, used as hard coatings. In this technique, reactive gases, e.g. O_2, CH_2 or N_2, are added to the sputtering gas, which under certain conditions react on the substrate with the sputtered metal atoms, e.g. Ti.

2.1.2 Microstructure evolution in pure metal films

Microstructure evolution in thin films is different from microstructure evolution in bulk materials. This is explained by the particular film deposition methods, and by the large surface to volume ratio in thin films, which is responsible for the small grain size. In the early stages of film growth, islands nucleate and coalesce. Not only grain size but also the final texture of the as-deposited film is determined by these processes (Ohring 1992). Thornton (1977) developed a structure zone model for refractory metal films. In this model, which can be applied to many other materials as well, three zones on the scale of different substrate temperatures are distinguished. In zone I found at homologous temperatures $T/T_m < 0.3$, where T_m is the melting temperature of the film, a fine grained structure evolves; a high working gas pressure promotes the extension of zone I. Zone II is characterized by columnar grains; it appears at $0.3 < T/T_m < 0.5$. Finally, large grains with low defect density and grooved grain boundaries are characteristic of Zone III ($T/T_m > 0.5$). Shadowing effects (zone I), surface diffusion (zone II) and bulk diffusion (zone III) control the respective as-deposited microstructures. For example, a Cu film sputtered at room temperature is expected to have a zone I-microstructure (the melting point of Cu is 1357 K, thus $T/T_m \approx 0.2$).

Fine grained films can undergo grain coarsening upon post-deposition annealing. A good overview on grain growth is written by Haessner (1978). Grain growth is driven by the reduction of total grain boundary area. Normal grain growth is characterized by a monomodal grain size distribution which develops in a self-similar fashion. Grain boundaries move towards their particular center of curvature resulting in the coarsening of larger and the disappearance of smaller grains. The driving force for normal grain growth is expressed as a pressure on the grain boundary (Haessner 1978) as

$$p_n = \frac{2\gamma_{gb}}{R}, \tag{2-1}$$

where γ_{gb} is the specific grain boundary energy, and R is the local radius of curvature.

Another type of grain growth is abnormal grain growth. During abnormal grain growth, few grains grow into a matrix of small stagnant grains. At an intermediate stage, it leads to a bimodal grain size distribution, while a monomodal distribution of very large grains is often found at this end of the process. Abnormal grain growth occurs under two conditions, namely the suppression of normal grain growth, and the existence of an energy advantage for the abnormally growing grains.

Grain growth in thin films usually stagnates if the median grain size is of the order of two times the film thickness. Pinning at grain boundary grooves is commonly accepted as the physical origin for stagnation of grain growth. This was first described by Mullins (1958). In this model, a grain boundary intersecting the surface is trapped to its surface groove because it would gain length upon moving out of the groove. This, however, is only the case for large grains which have a small in-plane and thus a small out-of-plane curvature (which is equal in amount but opposite in sign at equilibrium). Small grains with boundaries intersecting the surface at a larger angle to the surface normal can escape from the groove. Grain size distributions in thin films are usually lognormal (see section 3.2). The same distributions resulted from computer simulations of two dimensional grain growth, into which a pinning force in the form of a critical grain boundary curvature was introduced (Thompson 1990).

As mentioned above, stagnation of normal grain growth can lead to abnormal growth. In thin films, surface and interfacial free energies as well as elastic strain energy can contribute to the energetics in grain growth. In fcc metals, the (111) oriented close packed surface is associated with the lowest free surface energy, which is why abnormal growth of (111) oriented grains can be observed. On the other hand, elastic strain energy due to thermal strain is minimized for (100) oriented grains, if the material is elastically anisotropic such as Cu (see Appendix A). Thompson (1984) set up so-called texture maps for the final texture of thin films as a function of deposition temperature and film thickness which agreed well with experimental data.

2.2 Mechanical properties of thin metal films

2.2.1 Strain and stress in thin films

Thin metal films on Si substrates are often strained. In general, theses strains result from volume changes in the film which cannot be accommodated by the substrate, if good film-substrate adhesion is provided and if the substrate is significantly thicker than the film. Film volume changes are caused by several effects which are reviewed in the following. Misfit strain in epitaxial thin films is not considered here; films deposited onto Si sub-strates coated with amorphous diffusion barriers do not have an epitaxial relationship with the substrate.

Thermal strain results from a mismatch in thermal expansion coefficients of film and substrate material. It is defined as

$$\varepsilon_{thermal}(T) = \int_{T_0}^{T} \left[\alpha_f(T') - \alpha_s(T')\right] dT', \qquad (2\text{-}2)$$

where α_f and α_s are the linear thermal expansion coefficients of film and substrate material, and T_0 is a temperature at which the film is free of thermal strain (e.g. the deposition tem-perature). Thermal expansion coefficients of most metals are one order of magnitude higher than the expansion coefficient of Si: heating a Cu film on Si from room temperature to 500 °C induces a thermal strain of 0.7% (see appendix A). Thermal strain is isotropic in the film plane if both film and substrate material exhibit isotropic thermal expansion coef-ficients. This is the case for materials with cubic crystal symmetry.

Another class of film strains are *intrinsic strains* (see Thompson and Carel (1996) for a comprehensive overview). Negative intrinsic strain, developing during stabilization of the film microstructure during annealing, results from the annihilation of excess vacancies and a reduction in total grain boundary area in the film. Positive intrinsic strain can be ex-plained by atomic "shotpeening" and sputtering gas incorporation.

For films with a stabilized microstructure, only thermal strain shall be considered in the following. Film-substrate adhesion does not allow the film to expand freely; it forces the film to maintain the dimensions of the substrate: As a consequence, thermal strain must be accommodated by elastic and plastic film strains, as

$$\varepsilon_{thermal} = -(\varepsilon_{elastic} + \varepsilon_{plastic}). \tag{2-3}$$

Thermal strain of a film attached to a thick substrate can thus be compared to the external strain imposed to a sample by the testing machine in tensile testing. Thermal strain has been used as the principal means of deforming thin films for mechanical testing throughout this work.

Film *stress*, σ, and elastic film strain are related by the biaxial film modulus, M_f, as

$$\sigma = M_f \, \varepsilon_{elastic} \tag{2-4}$$

(Hooke's law). A thin film is in a state of plane stress because the film is free to relax in the direction normal to the film plane. For materials with cubic symmetry, stress is is o-tropic in the film plane for (100) and (111) oriented single crystalline films and for pol y-crystalline films with a (100) or (111) fiber texture (equi-biaxial stress). The biaxial moduli for (100) and (111) textured films of materials with cubic symmetry can be expressed with the components C_{ij} of the stiffness matrix as

$$M_f(100) = C_{11} + C_{12} - \frac{2C_{12}^2}{C_{11}}, \tag{2-5}$$

and

$$M_f(111) = \frac{6C_{44}(C_{11} + 2C_{12})}{C_{11} + 2C_{12} + 4C_{44}}, \tag{2-6}$$

respectively (Nix 1989).

Film stress can be relaxed by dislocation glide: Glide is driven by the resolved shear stress, τ, which is related to film stress by the respective Schmid factor, s, as

$$\tau = s\sigma . \tag{2-7}$$

The Schmid factor for equi-biaxial stress obeys the relation $s = \cos\lambda \cos\varphi$, where λ is the angle between the Burgers vector and the film normal, and φ is the angle between the glide plane normal and the film normal. This Schmid factor is similar to the Schmid factor for the case of uniaxial loading along the film normal. This is explained by the fact that super-position of both stress states would result in a hydrostatic pressure under which the re-solved shear stress on any glide system is zero. For a (111) oriented film, $s = 0$ for the (111) glide plane parallel to the film surface, and $s = 0.27$ for the 3 inclined {111}-type glide planes, for which the two angles are $\lambda = 35.3°$ and $\varphi = 70.5°$.

2.2.2 The yield stress of thin films

Thin metallic films support higher mechanical stresses than corresponding bulk materials (Nix 1989, Venkatraman and Bravman 1992, Keller et al. 1998). It has been claimed that dislocation movement in a thin film is dimensionally constrained by the high density of interfaces such as the film/substrate interface and grain boundaries (Arzt 1999). Models based on energy-balance arguments, however, underestimate the yield stress of thin films (Nix 1989, Thompson 1993, Nix 1998). The common idea of these models, which are pre-sented in the following, is that the energy cost of geometrically necessary interfacial dislo-cation segments must be balanced by the work done by an external stress upon glide.

In the model by Nix (Nix 1989), plastic yielding is accomplished by threading disloca-tions; it is impeded because of the deposition of dislocation segments at the film/substrate interface and at a possible film/passivation interface. These interfacial dislocation seg-ments resemble misfit dislocations in hetero-epitaxial films. The yield stress is described by the equation

$$\Delta\sigma_{Nix} = \frac{1}{s}\frac{\mu_{eff}\, b}{4\pi(1-\nu)}\frac{\sin\varphi}{t_f}, \qquad \text{(2-8a)}$$

where s is the Schmid factor defined in equation (2-7), b is the length of the Burgers vector of the film, ν is Poisson's ratio of the film, φ is the angle between the glide plane normal and the film normal, t_f is the film thickness, and μ_{eff} is an effective shear modulus which takes into account the effect of the stiffness of substrate and passivation on the line energy of the dislocation segments. It is defined as

$$\mu_{eff} = \frac{2\mu_f \mu_s}{(\mu_f + \mu_s)} \ln\left(\frac{\beta_s t_f}{b}\right) + \frac{2\mu_f \mu_o}{(\mu_f + \mu_o)} \ln\left(\frac{\beta_o t_o}{b}\right), \tag{2-8b}$$

where μ_f, μ_s, and μ_o are the shear moduli of film, substrate, and oxide, respectively, t_o is the thickness of the oxide, and β_s and β_o are constants of the order of unity defining the cutoff radii for the strain fields of the interface dislocations. It is noted that μ_{eff} is enhanced by a factor of approximately two in the presence of a passivation layer. The $1/t_f$-dependency predicted by equation (2-8) was found in many experiments (Venkatraman and Bravman 1992, Keller et al. 1998). However, it was reported by Keller et al. 1998 that the experimental yield stresses of Cu thin films were significantly higher than described by the Nix model. The authors reported a room temperature yield stress of 280 MPa for a 1 µm thick unpassivated Cu film; the yield stress for the same film calculated with equation (2-8), however, is only 45 MPa, which was calculated with the numbers $s = 0.27$ and $\varphi = 70.5°$ for (111)-texture, $\mu_{Cu} = 42.1$ GPa, $\mu_{Si} = 63.7$ GPa, $b = 2.56\times10^{-10}$ m (Frost and Ashby 1982), and $\nu = 0.34$; the constants β were set to unity.

Nix (1998) incorporated strain hardening into this model. The author calculated the elastic interaction of moving threading dislocations with the interface dislocations. Strain hardening was accounted for by the narrowing of the channels through which dislocations in a thin film can move such that the effective value for t_f in equation (2-8) is decreased.

Thompson (1993) extended the Nix model for the case of the deposition of dislocation segments at the grain boundaries. The expression for the yield stress is

$$\Delta\sigma_{gb} = \frac{1}{s} \frac{\mu_f b}{4\pi(1-\nu)} \ln\left(\frac{d}{b}\right) \frac{2}{d}, \tag{2-9}$$

where d is grain size and the other parameters are defined above. A $1/d$-dependency was found by Venkatraman and Bravman (1992) for the yield stress of Al thin films, in which grain size and film thickness had been independently varied by applying a back-etch technique. It is noted that grain size strengthening in bulk materials shows a different grain size dependency which is described by the Hall-Petch relation,

$$\Delta\sigma_{gb} = \frac{k_y}{\sqrt{d}}, \qquad (2\text{-}10)$$

where k_y is a material specific constant (see Courtney 1990, p. 169). This relationship was derived for dislocation pile ups at the grain boundaries, which in thin films have so far not been observed.

It is concluded that the energy-balance based models for the yield stress of thin films correctly describe the experimentally found dependency of yield stress on parameters such as film thickness and grain size. However, it was reported that the actual yield stresses of thin metal films are still higher than described by these models.

2.2.3 Modeling of film stress evolution during thermal cycling

The models for the yield stress of thin films described above are athermal. They depend only weakly on temperature through the elastic constants. However, experimental yield stress sometimes shows high variations with temperature. The yield stress of thin metal films on Si substrates is commonly measured by thermal cycling experiments, in which a film is plastically deformed under thermal mismatch strain, equation (2-2). Figure 2-1 shows two representative stress-temperature curves for Cu and Al thin films from the literature. They are characterized by a tensile stress at room temperature which decreases linearly upon heating. This segment is called the thermoelastic line, during which thermal strain is accommodated predominantly by elastic strain (see equation (2-3)). Deviation from this line in the compressive stress region indicates plastic flow. The dependency of yield stress on temperature, i.e. the *shape* of the stress-temperature curve, is different for the Cu and for the Al film: The Al film supports higher stresses at high temperatures than the Cu film. Interestingly, it is observed that noble metal films, which commonly show Cu-type curve shapes, change their thermo-mechanical behavior from Cu-type to Al-type behavior if they are protected by a passivation layer.

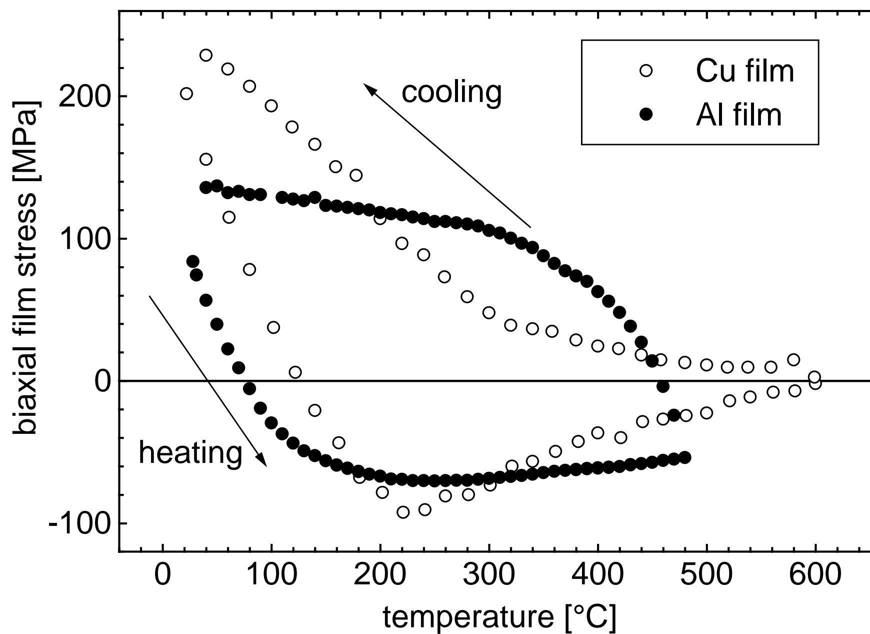

Figure 2-1 Experimental stress-temperature curves for a 1 μm thick Cu film (Keller et al. 1998) and for a 0.7 μm thick Al film (Joo et al. 1997). The stresses were measured with the wafer curvature method.

Cu-type curves were observed for unpassivated Cu films (i.e. films without a protective capping layer) by Flinn (1991), Thouless et al. (1993), Vinci et al. (1995), Thouless et al. (1996), and by Keller et al. (1998). They were also observed for other noble metal films, such as for Ag films by Thouless et al. (1996) and for Au films by Leung and Nix (1999). Al-type curves were observed both for Al films and for passivated noble metal films. They were observed for Al films by Venkatraman and Bravman (1992), Thouless et al. (1996), and Joo et al. (1997). They were observed for passivated Cu films by Vinci et al. (1995), Thouless et al. (1996), and by Keller et al. (1998). They were furthermore observed for passivated Ag films by Thouless et al. (1996) and for passivated Au films by Leung and Nix (1999).

Flinn et al. (1987) first proposed to model stress-temperature curves of Al films with thermally activated dislocation glide as the dominant deformation mechanism. The same mechanism was accordingly proposed for passivated noble metal films by Thouless et al. (1996). The simulated curve on the right hand side of Figure 2-2 shows a good qualitative agreement with experimental Al-type curves. Thermally activated dislocation glide at high

stresses in the presence of rectangular obstacles, on which this simulation was based, was described by Frost and Ashby (1982, p. 8) as

$$\dot{\varepsilon}_{plastic} = \dot{\varepsilon}_0 \exp\left[-\frac{\Delta F}{k_B T}\left(1-\frac{s\sigma}{\hat{\tau}}\right)\right], \tag{2-11}$$

where $\dot{\varepsilon}_0$ is a characteristic constant taking into account dislocation density, ΔF is the activation energy, k_B is Boltzmann's constant, $\hat{\tau}$ is a critical stress, and s is the Schmid factor defined in equation (2-7). ΔF represents the *strength* of a single obstacle, while the *distribution* of the obstacles is described by $\hat{\tau}$, which in many cases can be approximated by the Orowan stress (see section 2.3.1). $\hat{\tau}$ can be interpreted as an "athermal flow stress" as it represents the shear stress which would be necessary to overcome an obstacle at 0 K. It is noted that this equation is not a specific thin-film law.

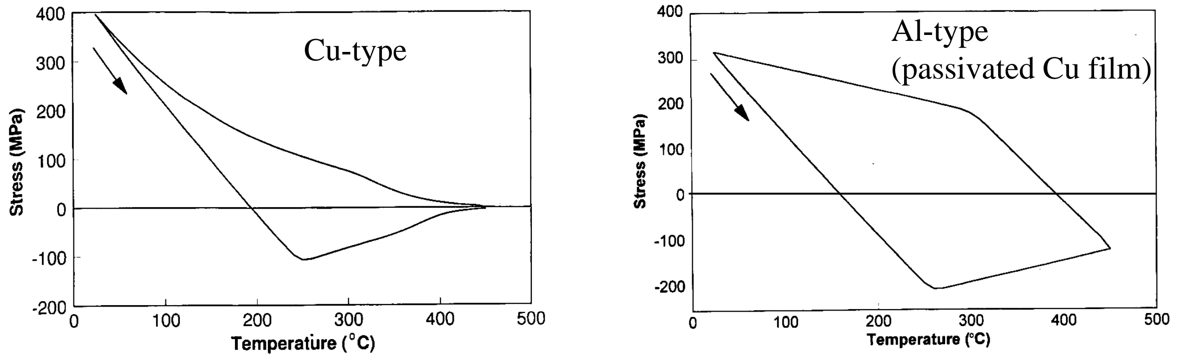

Figure 2-2 Simulated stress-temperature curves for an unpassivated Cu film (left) and for a passivated Cu film (right) from Thouless et al. (1996). The simulation of the Cu-type curve is based on the bulk constitutive equations for power-law breakdown creep and diffusional flow. The Al-type curve is based on thermally activated dislocation glide.

The Cu-type curve shape cannot be described by dislocation glide alone. The loss of film strength at high temperatures suggests creep mechanisms to be dominating stress evolution. Several authors have applied bulk constitutive equations for creep deformation from the deformation mechanism maps from Frost and Ashby (1982) to model the stress evolution of Cu-type films (Thouless et al. 1993, Vinci et al. 1995, Thouless et al. 1996, and Keller et al. 1999). The creep mechanisms used for modeling were power law creep, power-law breakdown, and diffusional creep, which are all mechanisms involving atomic

diffusion. Figure 2-2 (left) shows such a simulated stress-temperature curve for an unpas-sivated Cu film.

Despite the good agreement between the simulated curves and experimental data, the procedure described remains unsatisfactory because of the use of bulk constitutive equa-tions which do not account for the specific geometry of a thin film. The use of bulk equa-tions can therefore not lead to an accurate picture of the actual deformation mechanisms involved in thin films. In particular, the combination of several bulk models produces a large number of free fitting parameters, which makes it possible to produce good agree-ment between experimental and theoretical data without the accompanying understanding of the processes involved.

2.3 Microstructure and mechanical properties of alloy films

In this section, the oxide dispersion strengthening concept is discussed. It is based on the introduction of a fine dispersion of thermally stable ceramic particles into the metallic ma-trix to increase mechanical strength up to high temperatures. To date no systematic work is reported to apply this alloying strategy to thin films in the 1 micrometer thickness range. The original idea behind the oxidation experiments with Cu-Al alloy films in this work was to create aluminum-oxide particles by internal oxidation. However, as a result of the short diffusion paths in thin films, the particles did not form. This section is not essential for the understanding of this work; however, several relationships presented in this section are utilized in the discussion in chapter 5.

2.3.1 Mechanical properties of dispersion strengthened bulk alloys

The Orowan mechanism

The introduction of a fine dispersion of ceramic particles into a metallic matrix can im-prove the strength of materials at room temperature and at high temperatures. High thermal stability of a ceramic prevents the particles from ripening and dissolving, which thus retain their ability to impede dislocation motion at temperatures even close to the melting point of the metallic matrix.

Second phase particles situated on the glide plane impede dislocation glide, resulting in an increase in flow stresses (see e.g. Courtney 1990, p. 184). Upon yielding, dislocations

either cut the particles, or they circumvent the particles by the bowing mechanism described by Orowan. While cutting dominates if the particle are small, the bowing mechanism is observed for large particles (non-deformable particles). The Orowan mechanism can be observed in TEM: a dislocation which encounters a pair of particles on its glide plane bows around the particles; yield occurs when the dislocation can bypass the particles leaving one dislocation loop around each particle. The yield stress in shear due to this mechanism, $\Delta\tau_{Or}$, is approximately

$$\Delta\tau_{Or} = \frac{\mu b}{L_p}, \tag{2-12}$$

(the Orowan stress) with the matrix shear modulus μ, the Burgers vector b and the mean particle distance L_p.

The mean particle distance is a quantity rather difficult to measure. It can be expressed as a function of the total volume fraction of the second phase, f, and the mean particle radius, r_p, which can be obtained from microscopic studies; a simple geometric model for spherical particles of uniform size yields

$$L_p = \left(\sqrt{\frac{2\pi}{3f}} - \frac{\pi}{2}\right) r_p \,. \tag{2-13}$$

Inserting equation (2-13) into equation (2-12) gives the relation

$$\Delta\tau_{Or} \propto \frac{1}{r_p}, \tag{2-14}$$

from which it follows that a fine dispersion of small particles is important to obtain a maximum strengthening effect. For example, the yield stress in shear of a Cu crystal increases by 100 MPa if the particle distance is 100 nm, which is estimated from equation (2-12) using the values $\mu = 42.1$ GPa and $b = 2.56$ Å for Cu. If the total volume fraction of second phase particles is 1%, the particle radius must be as small as 10 nm, as obtained from equation (2-13).

Creep deformation

At temperatures above $T/T_m \geq 0.6$, where T_m is the melting temperature of the matrix material, the Orowan description fails as dislocations pass the particles at $\tau < \tau_{Or}$ by climb. However, it was found that finely dispersed ceramic particles can enhance the high-temperature strength of many alloys, if the particles remain stable during creep testing. In a rather empirical approach, the creep behavior of dispersion strengthened alloys had been described with a power law with a threshold stress below which practically no creep deformation is found. This approach was replaced by an analytical law set up by Rösler and Arzt (1990). From TEM studies it was deduced that not overclimbing of the particle, but rather the detachment of the dislocation segment attached to the particle rear side is the rate-limiting step in creep deformation. It was shown that the creep strength of particle strengthened alloys was determined by the attractive interaction between particle and dislocation, which was explained by the partial relaxation of line energy at the particle/dislocation interface. The new creep model resulting from this analysis has been successfully applied to explain the creep behavior of many dispersion strengthened alloys.

Creep voiding

Creep deformation can lead to specimen fracturing. Creep rupture is almost always related to grain boundary failure. One mechanism often observed is voiding at the grain boundaries which leads to failure upon coalescence of the voids. Second-phase particles located on grain boundaries are preferred nucleation sites for the growth of a void. As a complete monograph on high temperature fracture, the book by Riedel (1987) is recommended.

Creep voiding is accounted for by atomic diffusion from a void located at a grain boundary into the grain boundary itself, if a tensile normal stress component, σ_n, acts upon it. Void growth is driven by a gradient in chemical potential (see e.g. Hull and Rimmer 1959). The chemical potential at a grain boundary under normal stress can be written as

$$f = f_0 - \sigma_n \Omega , \qquad (2\text{-}15)$$

where f_0 is the chemical potential inside the grain, and Ω is the atomic volume. The chemical potential at the void surface is

$$f = f_0 - 2\gamma_s \Omega / R , \qquad (2\text{-}16)$$

where γ_s is the free surface energy and R is the radius of curvature of the surface. Thus, if $R > 2\gamma_s/\sigma_n$ the void will grow, while it would sinter out in the opposite case.

Cocks and Ashby (1982) analyzed the growth of voids in the regime of different mechanisms including grain boundary and surface diffusion. Spherical voids are formed if grain boundary diffusion is rate limiting while the voids are crack-like if surface diffusion is rate limiting. In the former case, the growth rate of a single void is given as

$$\frac{dV}{dt} = \frac{2\pi\delta D_{gb}\sigma_n\Omega}{k_B T}\frac{\left(1 - l_v^{\,2}/r_v^{\,2}\right)}{\ln\left(l_v/r_v\right)}, \tag{2-17}$$

where V is the total volume transported from the surface of one void into the grain boundaries, δD_{gb} is the grain boundary thickness times the grain boundary diffusivity, r_v is the void radius, and $2l_v$ is the distance between two voids.

2.3.2 Grain growth in the presence of particles

In section 2.1 it was carried out that the suppression of normal grain growth can lead to abnormal grain growth. Normal grain growth can be suppressed effectively by second phase particles which act as grain boundary pinning sites. Pinning is explained by the reduction in grain boundary area at the pinned site. The pinning force can be written as (Zener 1949)

$$p_Z = \frac{3f\gamma_{gb}}{2r_p}, \tag{2-18}$$

where f is the total volume fraction of second phase particles. Equating (2-1) and (2-18), and making the approximation $R \approx d$ yields the maximum final grain size,

$$d_{\max} = \frac{4r_p}{3f}. \tag{2-19}$$

This shows that particle pinning is the most effective if the particles are small and if the volume fraction of the second phase is large.

Little work has been published on the influence of alloying on abnormal grain growth in thin films. Longworth et al. (1991) reported on abnormal grain growth in dilute Al-Cu-Cr alloy films. Both $CuAl_2$ and ternary intermetallic precipitates were found in TEM which were supposed to act as pinning sites suppressing normal grain growth. Harper et al. (1994) observed abnormal grain growth in evaporated dilute Cu-Co alloy films. In this case, a b-normal grain growth was accounted for by discontinuous precipitation of Co at the moving grain boundary of an abnormally growing grain. A moving grain boundary offers a fast diffusion path for precipitation from the supersaturated matrix of the small matrix grains. A n-other example is electroplated Cu, which is currently used as a material for conductor lines in semiconductor industry. These films exhibit abnormal grain growth even at room te m-perature (Harper et al. 1999). The very small as-deposited grain size was explained by grain boundary pinning at impurities used as bath additives in the deposition process. The triggering mechanism for the abnormal grain growth, however, is not understood in these films.

Theoretical work was presented by Riege et al. (1998), who introduced particle drag into computer simulations of two dimensional grain growth. The authors found a relation for the stagnant grain size of

$$d_{\max} \propto \frac{r_p}{\sqrt{f}}, \qquad (2\text{-}20)$$

unlike the $d_{\max} \propto r_p / f$ relation from equation (2-19). It was shown that this difference is based on the non-random particle/boundary intersections, which resulted from the co m-puter simulation: for the derivation of equation (2-19), *random* particle/boundary intersec-tions were assumed, which leads to a much smaller fraction of particles located at a grain boundary.

2.3.3 Processing of dispersion strengthened thick films

Film deposition methods, namely sputtering, evaporation and electroplating, have been a p-plied in the past to produce oxide dispersion strengthened (ODS) films. The purpose of the work reported on in the literature, however, was to produce thick films with bulk prope r-ties. The term bulk property thereby refers to a grain size to film thickness ratio much smaller than unity. To the author’s knowledge, the results were of purely academic interest

and no technical application resulted from the work. A short review of the literature is given in the following.

Häussler et al. (1979) found enhanced yield strengths in dilute Cu-Ti-Fe films sputtered from an alloy target. The films were 30 - 100 µm thick and had a grain size of 1 µm. The target material is an age hardenable alloy which owes its strength to Fe_2Ti precipitates. Unlike the bulk material, which lost strength after annealing above the stability region of Fe_2Ti, the films retained their high yield strength after prolonged annealing at 650 °C. The authors argued that this behavior was due to thermally stable TiO_2 and Fe_3O_4 dispersoids that formed during sputtering by reaction with residual oxygen present in the sputtering process. Nagorka et al. (1995) reported on the sputtering and internal oxidation of thick films of a Cu-1at.%Y alloy. Small yttrium-oxide particles were found in TEM. Grain size was in the range of 1 µm after annealing.

Majumder (1977) reported on the synthesis of Cu-Al_2O_3 alloys by dual source electron beam evaporation. These films were 2000 µm thick. A very fine dispersion of alumina particles with radii of about 40 Å were obtained to which the hardness enhancement was credited by the author. This hardness was retained even after annealing at $T/T_m = 0.94$. Movchan et al. (1977) applied a similar technique to fabricate Ni films strengthened by ZrO_2 particles. These films were also thick (1000 - 2000 µm), with very small grain sizes of approximately 1 µm.

A different processing route was proposed by Sautter (1963) who had first described dispersion strengthening of electro-deposited alloys. In this case, Ni films were deposited from an electrolyte while the second phase particles, namely Al_2O_3, were suspended into the plating bath to be subsequently buried in the growing film. Suzuki et al. (1986), who applied this technique to alumina strengthened silver films, found improved room temperature yield strengths in tensile testing of the free standing films. The yield strengths declined upon annealing which was accounted for by grain growth. The role of grain boundary strengthening could not be fully resolved in these films, but the function of the particles to stabilize small grains, which also leads to strengthening, was pointed out by the authors.

The only work on ODS films in the one micrometer thickness range was reported by Bader et al. (1994). Thin Al films were laser reflowed to obtain large grains. The particles were produced by oxygen ion implantation. Very small particles were identified by a typical strain field contrast in transmission electron microscopy. The strength of the films increased upon ion implantation.

2.3.4 Internal oxidation: The Cu-Al system

Dispersion strengthened materials can be produced by internal oxidation. The original idea behind the oxidation experiments with Cu-Al alloy films in this work was to create aluminum-oxide particles by internal oxidation. Internal oxidation refers to the preferential oxidation of an element B within a matrix of a more noble metal A. The review by Meijering (1971) is recommended for a detailed discussion of this method. Two requirements must be fulfilled for internal oxidation to be achieved: first, the oxygen affinity, ΔG^0, of the element B has to be higher than the oxygen affinity of the element A. Second, the so-called permeability $c_O D_O$ of oxygen in the alloy must be greater than the permeability $c_B D_B$ of the element B in the alloy, where c_O and c_B denote the concentration (or solubility) and D_O and D_B the diffusivities of oxygen and the element B in the alloy, respectively. The latter is often fulfilled because gases are generally interstitially dissolved in a metal resulting in a low activation energy for diffusion, while metal-in-metal diffusion shows much higher activation energies. In a first order model, the in-diffusing oxygen is considered to consume all B atoms at the so-called internal oxidation front with position ξ, defined as coordinate with respect to the sample surface. ξ follows a parabolic time law given by Meijering (1971) as

$$\xi^2 = \frac{2c_O D_O}{n c_B} t \, , \tag{2-21}$$

where n is half the valency of the metal cations formed (e.g. $n = 1.5$ for Al_2O_3) and t is time.

Two competitive processes to internal oxidation exist. The first is external oxidation of the element B which occurs if the permeability of B is above a critical value. The second competitive process is the external oxidation of the matrix A. This occurs if the oxygen partial pressure during oxidation is greater than the dissociation pressure of the matrix oxide. In the method by Rhines, the oxygen activity during internal oxidation of Cu-based alloys is controlled by sealing the specimen together with a mixture of Cu_2O and Cu powder. The oxygen partial pressure thus never exceeds the oxygen equilibrium pressure of the reaction $Cu_2O \Leftrightarrow 2Cu + 1/2 O_2$ ("Rhines-pack"). Other methods to control the oxygen activity apply buffered gas mixtures, e.g. CO_2/CO or H_2O/H_2.

The radii of the oxide-particles obtained by internal oxidation can vary in a large range. For large differences in oxygen affinities, ΔG^0, of the elements A and B, small par-

ticles are found, and vice versa. For example, for internally oxidized Ag-1%Mg alloys a very fine, quasi “molecular” dispersion of oxide was found (“oxide in supersaturated solution”). In Cu-Zn alloys, on the other hand, macroscopic ZnO needles were found after internal oxidation (Meijering 1971). Two different explanations exist for this phenomenon: The first argument is that particles are nucleated more easily when more free energy is gained by the oxidation. The second explanation is that nucleated particles ripen faster if ΔG^0 is low, associated with a high solubility product of the oxide in the matrix. During so-called Ostwald ripening (Wagner 1961), the mean particle radius, r_p, obeys a cubic time law according to

$$r_p^{\,3} - r_0^3 = \frac{8}{9}\frac{D_B c_B \gamma_i V_m}{RT} t, \qquad (2\text{-}22)$$

where r_0 is the mean particle radius at time $t = 0$, γ_i is the particle/matrix interfacial energy, V_m is the molar volume of the particle, R is the universal gas constant and T is the absolute temperature.

A commercial Cu alloy strengthened with Al_2O_3-particles named Glidcop is produced by internal oxidation of Cu-Al powder with subsequent compaction by hot extrusion. The alloy is applied as a high-conductivity and high-strength material. The structure of the particles in this alloy was investigated by Ernst et al. (1991). The authors found a bimodal size distribution of the second phase particles, with α-alumina particles approximately 1 μm in diameter located at the grain boundaries and small triangular platelets of cubic Al_2O_3 within the matrix.

Dilute Cu-Al single crystals were investigated by Kupcis et al. (1973), who studied particle distribution and the strength of the crystals after internal oxidation. Depending on oxidation conditions either very small coherent particles with diameters of approximately 10 nm or larger incoherent particles with diameters larger than 40 nm were found. The strengthening effect for the small particles was one order of magnitude smaller than expected from theory, which was accounted for by particle fracturing. Further references on literature of internal oxidation of Cu-Al are found in the publications of Ernst et al. (1991) and Kupcis et al. (1973).

The internal oxidation of bulk Cu alloys is usually carried out at temperatures close to the melting point of Cu, 1084 °C, for two reasons. The first reason is to prevent oxidation of the Cu: The dissociation pressure of Cu_2O is high at high temperatures. The second reason is to achieve a high permeability of oxygen in the matrix. In the present work annealing temperatures were limited to 600 °C, above which diffusion of Cu into the diffusion barrier SiN_x was expected. However, the small film thickness in the range of 1 μm allowed complete internal oxidation at reasonable times, as shown in Figure 2-3.

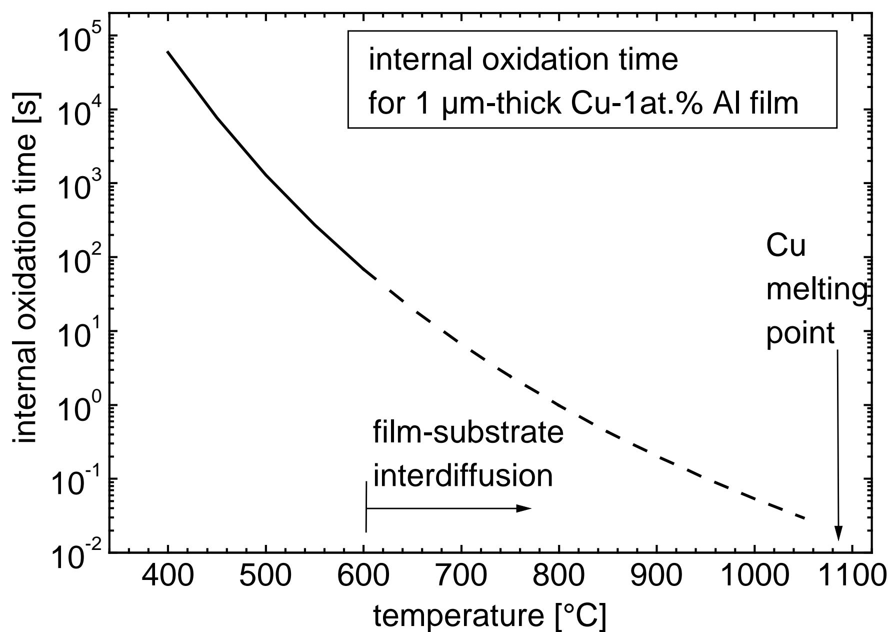

Figure 2-3 The time for complete internal oxidation of a 1 μm thick Cu-1at.%Al film versus oxidation temperature. Equation (2-21) was applied, setting $\xi = 1$ μm and using the thermo-dynamical data from Fromm and Gebhardt (1976), p. 660. Above 600 °C, film-substrate interdiffusion would lead to the degradation of the films, which is why this temperature was chosen as the maximum annealing and oxidation temperature.

2.4 Summary of the literature and aims of this work

Thin films behave differently than bulk materials. The yield stress of thin metal films is higher than that of corresponding bulk metals. Current models which describe the yield stress of thin films in terms of interface/dislocation interaction underestimate the experimental yield stresses. The evolution of thin film yield stress as a function of temperature is

not completely understood, either. Simulations of the stress evolution during thermal cycling based on bulk creep equations have not delivered insight into the specific stress relaxation mechanisms in thin films. Despite the growing industrial importance of thin metal films, only few publications can be found about the application of bulk alloying methods for the strengthening of thin films so far.

The aim of this work is to investigate the predominant deformation mechanisms in pure Cu and in dilute Cu alloy films. As central aspect, the influence of very clean fabrication conditions on microstructure evolution and mechanical behavior of pure Cu films will be studied. The idea behind the alloying is to selectively oxidize the alloying element in order to create a thermally stable second phase. Microstructure evolution in the presence of the alloying element will be researched as well as the influence of alloying on the thermomechanical behavior of the films.

3 Experiment

The experimental techniques applied in this research project were the synthesis of thin films in the 1 μm thickness range by magnetron sputtering, microstructural characterization of the films predominantly by focused ion beam microscopy (FIB), and characterization of the thermo-mechanical film properties by wafer curvature measurements. These techniques are described in this chapter.

3.1 Film synthesis

3.1.1 UHV sputtering system

Vacuum system

Pure Cu and Cu-Al films were produced by magnetron sputtering in a UHV multi chamber system (DCA Instruments, Turku, Finland). The system had been modified in order to maximize the purity of the films: Sputtering sources with a short sputtering distance were used, the Ar sputtering gas was further purified by a gettering system, and a Kaufman-type ion source for in-situ substrate cleaning has been added.

The complete procedure of film synthesis - substrate cleaning, sputtering, annealing, and oxidation - was carried out in the sputtering chamber without exposing the sample to air between one of these steps. Up to seven sample holders could be introduced into the system through a load lock. A buffer line between load lock and sputtering chamber allowed for the maintenance of the low base pressure in the sputtering chamber of 1×10^{-8} Pa. All three chambers were separated by vacuum valves. Each chamber could thus be vented separately. The base pressure of the buffer line was also 1×10^{-8} Pa. Both chambers had to be baked out for 48 h at 120 °C. In the load lock, pressure was of 1×10^{-6} Pa after baking out for 2 h with quartz lamps fixed inside the chamber. The sputtering chamber was evacu-

ated with a 1000 l/s turbo pump. A Ti sublimation pump was used to further improve the pressure. The buffer line was evacuated with an ion pump; the load lock was evacuated with a small turbo pump. Pressure was measured with ion gauges for UHV and with a capacitance manometer for the sputtering gas. The sputtering chamber was also equipped with a quadrupole mass spectrometer which was used for leak detection with helium and for monitoring the vacuum quality before and after film synthesis.

Deposition chamber

The deposition chamber was equipped with two magnetrons of the type Mighty MAK for 3" targets (US, Inc., Milpitas, CA). Both targets could be closed with a shutter. The relative sputtering distances could be changed using Quick Coupler Mounts with a Viton seal. The magnetron for the base element Cu had a sputtering distance to the substrate of 15 cm while the magnetron for the alloying element Al had a distance of 30 cm to the substrate. With this geometry, atomic concentrations of below 0.5 at.% Al could be obtained. The concentration of the alloying element was controlled via the relative sputtering powers. The targets were delivered by TMI, Inc. (Columbus, Ohio). They were 3" in diameter and 0.25" in thickness. The Cu target was of 99.997 purity and the Al target was of 99.999 purity. The targets were held by ferromagnetic backing plates.

For in-situ substrate cleaning by Ar-ion bombardment, a Kaufman-type ion source with an ion beam of 3 cm diameter (IBS-250, Commonwealth Scientific Corp., Alexandria, VA) was used. Both magnetrons and the ion source pointed to the sample holder and were aligned 35° off the vertical axis (sample normal).

The sample holder could be rotated at up to 150 rev/min. It was electrically isolated to allow for bias sputtering. The samples could be heated up to 700 °C with a boron nitride heating plate. The temperature was measured with a thermocouple placed between heating plate and substrate holder. The substrate temperature was controlled through the heating power. However, the real substrate temperature had to be calibrated, which was carried out with a massive Cu dummy sample to which a second thermo-couple was fixed.

Argon gas with 6N purity was used for both sputtering and ion bombardment. The gas was further purified by a chemisorptive gettering system (Waferpure Micro In-Line Gas Purifier, Millipore Corp., Bedford, MA). The content of water vapor and oxygen was below 1 ppb after gettering, as guaranteed by the supplier of the gas purifier. An electronic mass flow controller was used for regulating the gas flow. The oxygen gas had 4.8N purity.

A standard leak valve was used to control the oxygen pressure for oxidation experiments. Both gases were delivered by Messer Griesheim GmbH (Krefeld, Germany).

Film thickness calibration

The film thickness was adjusted by the sputtering power and the duration of sputtering. For the determination of the deposition rates and the thickness homogeneity, pure Cu and pure Al films were sputtered onto a glass substrate (microscope slide). The substrate was marked with a permanent marker, from which a part of the film was lifted off in an ultrasonic bath with acetone. The step height was measured using a profilometer (Dektak 3, Veeco Instruments Inc., U.K.). The deposition rate for Cu was 75 nm/min at 200 W. Cu-Al films were deposited by co-sputtering with 200 W sputtering power for the Cu target and 0 to 160 W sputtering power for the Al target. The resulting Al content was between 0 and 5 at.%. Film thickness dropped by 10% towards the edge of a 2” wafer. The values for film thickness in this work refer to the average film thickness.

Substrates

All films were deposited onto (100)-oriented Si substrates. The substrates were coated on both sides with amorphous thermal SiO_x and CVD SiN_x diffusion barriers. Both layers were 50 nm thick. For the wafer-curvature experiments 2” wafers with a thickness of 260-300 µm were used. They were delivered by CrysTec GmbH (Berlin, Germany). For other experiments square substrates of 15 mm×15 mm size were used. They were obtained by cleaving 4” wafers that had been previously scratched with a diamond scribe. The 4” wafers were 500 µm thick and were delivered by Aurel GmbH (Landsberg, Germany). The substrates were clamped on substrate holders of molybdenum. The holders had a diameter of 3” and were 2 mm thick. The clamps consisted of tantalum springs and were fixed by stainless steel screws.

3.1.2 UHV film synthesis: Cu and Cu-Al

In the following, a detailed description of film synthesis is given. It consisted of the 4 steps, substrate cleaning, sputtering, annealing, and oxidation. All steps were carried out in the deposition chamber without interruption of UHV conditions between the steps.

Substrate cleaning

The substrates were first cleaned by a strong stream of CO_2 or N_2 and transferred into the load lock. For in-situ surface cleaning by Ar ion bombardment, the substrate holder was transferred to the sample holder in the deposition chamber, which was grounded and connected to an ammeter and which rotated at 100 rev/min. Sputter cleaning was carried out for 3 min with 200 eV ion energy and an Ar gas flow of 4 sccm (standard cubic centimeter per minute).

Film deposition

In order to optimize film purity, two steps preceded film deposition which were analysis of the sputtering gas and target cleaning. Hydrogen was sometimes detected in the Ar gas. It probably originated from the steel pipes. The sputtering gas was analyzed by purging with a gas flow of 80 sccm for 1 min and recording the mass spectrum after 30 s. The contamination was removed by 1 to 3 pump and purge procedures. The targets were sputter cleaned before every film deposition. Each target was sputtered for 5 min with a sputtering power of 100 W and a gas flow of 80 sccm. During target cleaning the target shutters remained closed. For pure Cu films the Cu target was cleaned for at least 10 min to remove Al contamination. It is noted that analysis of the sputtering gas and target cleaning was carried out before the introduction of the substrate into the sputtering chamber.

During film deposition, the sample holder was rotated at 100 rev/min. The sample was grounded and the current was measured during sputtering. The Ar gas flow was 30 sccm resulting in an Ar pressure was 1×10^{-1} Pa. The turbo pump was not throttled back during sputtering because this would have led to an increase in the residual gas pressure of approximately one order of magnitude. During sputtering of 1000 nm Cu (which corresponded to a sputtering time of approximately 13 min) the substrate temperature increased to approximately 130 °C.

Post-deposition annealing and oxidation

Usually, the sputtered films were annealed in the deposition chamber directly after film deposition. A sample took 10 min to reach a temperature of (600 ±10) °C. After annealing, the sample cooled down to 100 °C within approximately one hour. During annealing, the chamber pressure increased to the 10^{-6} Pa range. For oxidation experiments, the tempera-

ture was adjusted and oxygen gas pressure was adjusted with the leak valve. For pressures up to 1×10^{-3} Pa , the oxygen pressure was controlled with the ion gauge.

3.1.3 HV film synthesis: Cu-Y

Cu-1at.%Y films were produced by sputtering of an alloy target in a high vacuum (HV) chamber. A magnetron for 2” targets (US-Gun II, US, Inc., Milpitas, CA) was used. The vacuum chamber was pumped by a turbo pump. The base pressure was 3×10^{-5} Pa after 24 h pumping. Ar gas with 5N purity was used for sputtering. The target was vacuum induction melted in an alumina crucible and cast into a degassed graphite mould. Y and Cu were pre-alloyed by arc melting. The same substrates as for the Cu and Cu-Al films were used. No substrate cleaning could be carried out. The films were sputtered with a sputtering power of 100 W and a working gas pressure of 2×10^{-1} Pa. The sputtering distance was 8 cm. The deposition rate was in the range of 100 nm/min. The total thickness variation of a film deposited onto a 2” wafer was 10%.

Annealing experiments were carried out in a quartz tube furnace under high vacuum. The pressure in the furnace was in the 10^{-4} Pa range during annealing. The sample took 12 min to reach a temperature of 600 °C. The temperature was calibrated using a thermocouple. The absolute error for the temperature was 10 °C. The annealing times given in this work include the heating time. Upon cooling down from 600 °C, the sample temperature reached 100 °C within 20 min. For the oxidation process, the oxygen partial pressure could not be controlled. Instead, oxygen from the residual gas and from the native oxide on the sputtered film were used for internal oxidation.

3.2 Microstructural characterization

Focused ion beam microscopy

A focused ion beam microscope (FIB) was used for the characterization of film topography (grooves, voids, hillocks), grain size, and texture. The working principle of a FIB is similar to that of a scanning electron microscope: The sample is also scanned, but in this case with a beam of focused high-energy gallium ions. A grey scale image is constructed from a detector current of secondary electrons emitted from the sample. The spatial resolution is limited by the probe size. Due to the high momentum of the Ga ions, a strong channeling

contrast is obtained. This was used for grain size analysis and a rough texture analysis. Grains with a more open crystallographic orientation with respect to the primary ion beam appear darker in the FIB image: because of the higher channeling depth for the ions, the total number of secondary electrons emitted from these grains is smaller. Furthermore, the high momentum of the primary Ga ions was use to modify the film surface. Oxide films were sputtered off during imaging. For preparing cross sectional views, a square hole was etched into the film with the ion beam. After tilting the sample by 45°, the profile could be imaged. It is noted that no sample preparation was required for the FIB. In this work, an FEI 200 workstation with a 30 keV Ga beam and 45° sample tilting range was used. The spatial resolution was 30 nm.

Transmission electron microscopy

A JEOL 200CX transmission electron microscope working with 200 kV beam energy was used for this work. Plan-view samples were prepared by ion milling to electron transparency after grinding and etching a window from the back side of the sample; the sample preparation is described in detail elsewhere (Keller 1996).

Quantitative microstructure analysis

The size distributions of grains, twins and grain boundary voids were evaluated with a computer program for quantitative microstructure analysis (Quantimet 500, Zeiss, Oberkochen, Germany) using digitized FIB images. For grain size analysis, a series of three FIB images with the respective tilt angles of 15°, 20° and 25° were taken of one surface area. All grain boundaries seen in the 15° image were drawn on a transparency foil. The images with 20° and 25° tilt angle served as references to add in boundaries not visible in the 15° image. Straight boundaries clearly identified as coherent twin boundaries were disregarded. A digitized image of the transparency foil was analyzed by the computer program. Throughout this work, grain size is defined as the equivalent circular diameter,

$$d = \sqrt{\frac{4A}{\pi}}\,, \qquad (3\text{-}1)$$

where A is the grain area. Grain size distributions are fitted to the lognormal distribution,

$$f(d) = \frac{1}{\sigma\sqrt{2\pi}d} \exp\left\{-\left[\ln(d/d_{50})/\sqrt{2}\sigma\right]^2\right\}, \qquad (3\text{-}2)$$

where f(d) is the fraction of grains with diameters in the interval between d and $d+\Delta d$, d_{50} is the median grain diameter, and σ is the lognormal standard deviation. The cumulative distributions were plotted on log-probability axes, in which a lognormal distribution appears as a straight line.

For twin analysis, all grains which were clearly identified as twin lamellae were outlined on FIB images taken with 15° sample tilt. They were scanned into the same program. Both the total twin area and the total twin boundary length were evaluated. Some grains had twin boundaries parallel to the film surface; these boundaries, which could be detected only in cross-sectional views with the FIB, were disregarded for the statistics.

The size distribution of grain boundary voids was obtained from FIB images of untilted samples. The definition of the equivalent circular void diameter, d, followed equation (3-1), in which A was replaced by the projected area of a void. The total void volume of a specific sample area was evaluated by the equation

$$V_{voids} = \sum_{i} \frac{2\pi}{3}\left(\frac{d_i}{2}\right)^3. \qquad (3\text{-}3)$$

Texture analysis

Texture analysis was carried out with standard X-ray methods. A Siemens D5000 machine equipped with an Eulerian cradle was used; the monochromator was set to Cu K α_1 radiation. Locally resolved texture information was obtained from electron backscattering diffraction experiments carried out with a scanning electron microscope (LEO 438VP) using the Orientation Imaging Microscopy (OIM) software (TSL, Utah, USA).

Auger electron spectroscopy

Depth profiles of the elemental distribution at the surface regions of the films was carried out by Auger electron spectroscopy using the Scanning Auger Multiprobe PHI 600 by Physical Electronics.

3.3 Mechanical and electrical characterization

Wafer curvature technique

The mechanical film properties were measured as function of temperature in wafer curvature experiments. A useful discussion of this method is found in Nix (1989). In a wafer curvature experiment, the film/substrate specimen is thermally cycled between a minimum and a maximum temperature. The film is deformed both elastically and plastically due to the thermal mismatch stress generated upon temperature variation (see section 2.2.1). The film stress deforms the substrate, which usually is much thicker than the film, only elastically; the stress in the film can be calculated from the radius, R, of substrate curvature using the relation derived by Stoney (1909),

$$\sigma = \frac{M_s t_s^2}{6 t_f} \frac{1}{R}, \tag{3-4}$$

where M_s is the biaxial modulus of the substrate, and t_f and t_s are film and substrate thickness, respectively. Note that this equation depends only on the elastic properties of the substrate, but not on those of the film.

Substrate curvature was measured with a laser scanning method. The beam of a He-Ne laser is thereby scanned across the wafer with a rotating mirror placed in the focal plane of a lens (1 m focal length). Parallel beams reflected by a curved surface are no longer parallel. Thus, the curvature of the wafer is determined from the position of the reflected laser spot on a position-sensitive photo cell. A maximum radius of curvature of 10^4 m can be resolved with this technique. The furnace, into which the wafer was placed, could be heated at a controlled rate from room temperature to 600 °C. All experiments were run at a heating rate of 6 K/min. The cooling rate was controlled by the flow of cold nitrogen and could be kept at 6 K/min up to 100 °C. Below 100 °C, the cooling rate dropped to below 4 K/min. During the experiment, the furnace was purged with nitrogen. At high temperatures, the combustion products of a cellulose cloth produced a reducing atmosphere in the furnace. The system used in this work is described in further detail in Flinn et al. (1987) and Keller et al. (1998).

The system was designed for the use of 4” wafers which were positioned on a tripod consisting of three NiCr-Ni thermocouples. An adapter for 2” wafers was built for this work. A hole with a diameter of 5.2 cm was drilled into a 4” Si wafer with a rotating brass

tube using boron nitride polishing paste. Three notches of Si were fixed to the inside of this ring using a high-temperature cement such that a 2” wafer could rest upon them.

Uncoated wafers are not perfectly plane. Additional curvature is added due to the influence of gravitation. Therefore, the curvature of each bare wafer was measured with the wafer curvature apparatus before film deposition. This local curvature profile was automatically subtracted from the measured curvature during the thermal cycling experiment, following the procedure described by Flinn et al. (1987). The error of the film stress had two major contributions. The first was an absolute error of ± 5 MPa/t_f, where t_f is the film thickness in µm. This error was due to the re-positioning accuracy for a wafer on the tripod and due to thermal drift. The second error in film stress was a relative error of $\pm$ 5%, which was estimated as result from the film thickness inhomogeneity.

Nanoindentation

A nanoindenter was used to measure the film hardness at room temperature. In this technique, a film is indented with a diamond tip. Both tip displacement (indentation depth) and the force applied to the tip are detected, from which the film hardness is evaluated. A good overview of different indentation methods for thin films is found in Brotzen (1994).

In this work, a commercial instrument, the Nano Indenter II (MTS Systems Corp., Eden Prairie, MN), was used. The Berkovich type diamond tip was loaded by a coil and permanent magnet assembly. The force was controlled through the current in the coil. The force resolution was 1 µN. Displacement was measured with a 3-plate capacitance gauge. The accuracy of the displacement measurement was better than 1 nm. In this work, the continuous stiffness method (Oliver and Pharr 1992) was applied. Both hardness and elastic modulus of the film could be measured continuously upon loading. A sinusoidal oscillation with a small amplitude and a frequency of 45 Hz is superimposed to the load ramp. From the response of the displacement signal, which is gained by a lock-in technique, the actual contact stiffness and contact depth were be calculated. Experiments were carried out with constant strain rate. The error of the measurement was governed by the accuracy of the tip shape calibration, which is necessary to calculate the contact area. A second source of error was the pile-up of film material which leads to an apparent increase in hardness.

Electrical sheet resistance

The electrical resistance of a film, the sheet resistance, R_S, was measured with a 4-point probe. The sheet resistance is defined as

$$R_S = \frac{\rho}{t_f}, \quad (3\text{-}5)$$

where ρ is the specific resistivity of the film material. A 4-point probe consists of 4 equidistant metal pins which are placed on the film. A current, I, flowing through the two outer pins produces a voltage drop, V, between the two inner pins. If the film diameter is large compared to the dimension of the 4-point probe, the sheet resistance is obtained as (Ohring 1992)

$$R_S = \frac{\pi}{\ln 2}\frac{V}{I} \cong 4.53\frac{V}{I}. \quad (3\text{-}6)$$

In this work, a commercial Alessi C4S Probe Head (Cascade Microtech Inc., Beaverton, Oregon) and a standard assembly of power supply, microammeter and nanovoltmeter were used. The applied currents were 50 mA, 100 mA and 200 mA. The sample was either a 2" wafer or a (13 mm)^2 square film. The latter was too small compared with the pin distance of 1.67 mm to apply equation (3-6) (if the current is confined to a relative small area, the voltage drop between the two inner pins becomes larger). Measuring a reference film (1 μm annealed Cu) deposited under the same conditions on both a wafer and a small substrate, a correction factor of 0.91 ± 2% was found for R_S. The error of this factor determined the error for R_S.

4 Results

In this work, pure Cu and dilute Cu-Al and Cu-Y films were produced by magnetron sputtering on diffusion-barrier coated Si substrates. The Cu and Cu-Al alloy films were fabricated under ultra high vacuum (UHV) conditions. The microstructure and the mechanical film properties were studied primarily with the focused ion beam microscope and with the wafer curvature method. In the following, a detailed record of the experimental results is presented. In section 4.1 and section 4.2 the results on microstructure and mechanical behavior of pure Cu films are presented. In section 4.3 and section 4.4 the microstructure and mechanical properties of Cu-Al films are presented. The development of the microstructure of high-vacuum (HV) sputtered Cu-1at.%Y films is presented in section 4.5. Section 4.6 gives a summary of the experimental results.

4.1 Pure Cu films: Microstructure evolution

4.1.1 UHV-annealed films

Focused ion beam microscopy

The as-sputtered Cu films had small non-columnar grains (Figure 4-1). In the FIB micrograph, single grains are identified by different grey scales. The typical grain structure of an annealed Cu film (10 min at 600 °C in UHV) is shown in Figure 4-2. Large columnar grains with few twins are typical for these films as observed in the FIB. Grooves were visible at some grain boundaries. Annealing hillocks were not observed.

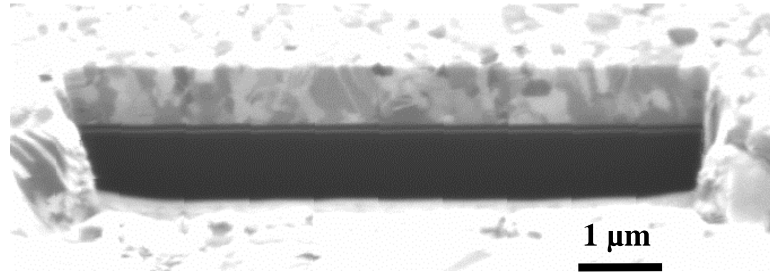

Figure 4-1 FIB micrograph of a 1 µm thick as-deposited Cu film [044][1]. The tilt angle of the sample is 45°. Small non-columnar grains are visible on the side wall of the sputter etched trench in the middle of the picture. The Si substrate appears black. The SiN_x and SiO_x diffusion barriers can be identified between film and substrate.

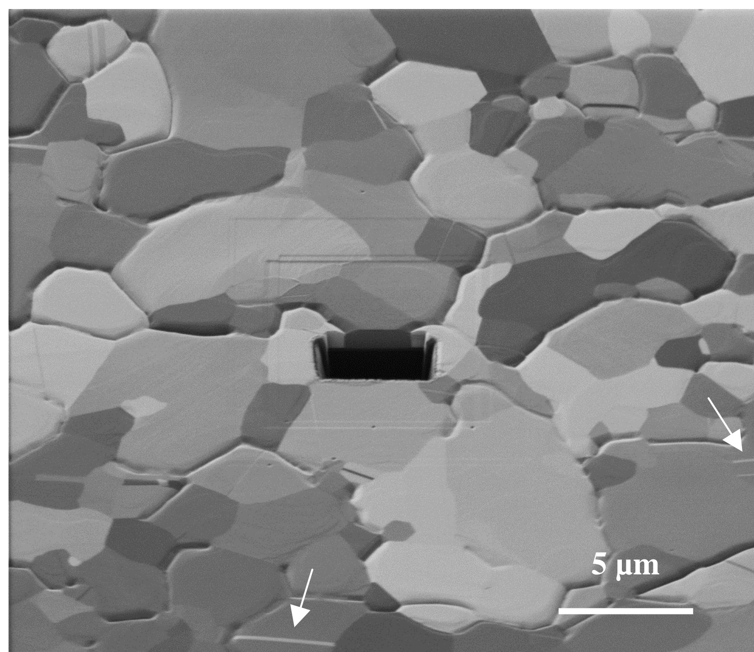

Figure 4-2 FIB micrograph of a 1 µm thick Cu film which was UHV-annealed for 10 min at 600 °C directly after deposition [091]. The tilt angle is 45°. Grains appear in different grey scales due to the different crystallographic orientations towards the primary ion beam of the FIB. Some grain boundaries are grooved. The film shows very few twin lamellae (arrows).

[1] The number in square brackets is the film number. In Appendix C, all Cu and Cu-Al films are listed together with a detailed description of the fabrication conditions.

Grain size and twins

Two striking features of the UHV-sputtered and annealed Cu films were their large grain size to film thickness ratio and the low density in twin grains. This was so far not observed with other Cu films from the literature, which were sputtered under HV conditions (Gupta et al. 1992, Keller 1996). In Figure 4-3 (a), grain size distributions for 3 different films are shown. The grain size distributions are lognormal, as indicated by the linear course of the points. The median grain sized increased with increasing film thickness. The features of the grain size distributions are summarized in Table 4-1.

The analysis of the distribution of twin grains in these films is presented in Table 4-2. For the films sputtered with substrate cleaning, the twin boundary length per area is constant (within the error bar). The twin grains become fewer and larger with growing film thickness.

The effect of in-situ substrate cleaning by ion bombardment on the microstructure of a 1 µm thick Cu film was studied. After deposition, the film was annealed for 10 min at 600 °C in UHV. It was found that the grain size distribution was, within the error bar, identical to the distribution of the film sputtered with substrate cleaning (Figure 4-3 (b) and Table 4-1). The density of twin grains, on the other hand, was enhanced by a factor of two as shown in Table 4-2. Also the texture of this film was changed if compared to a film sputtered after substrate cleaning. This is shown in the following.

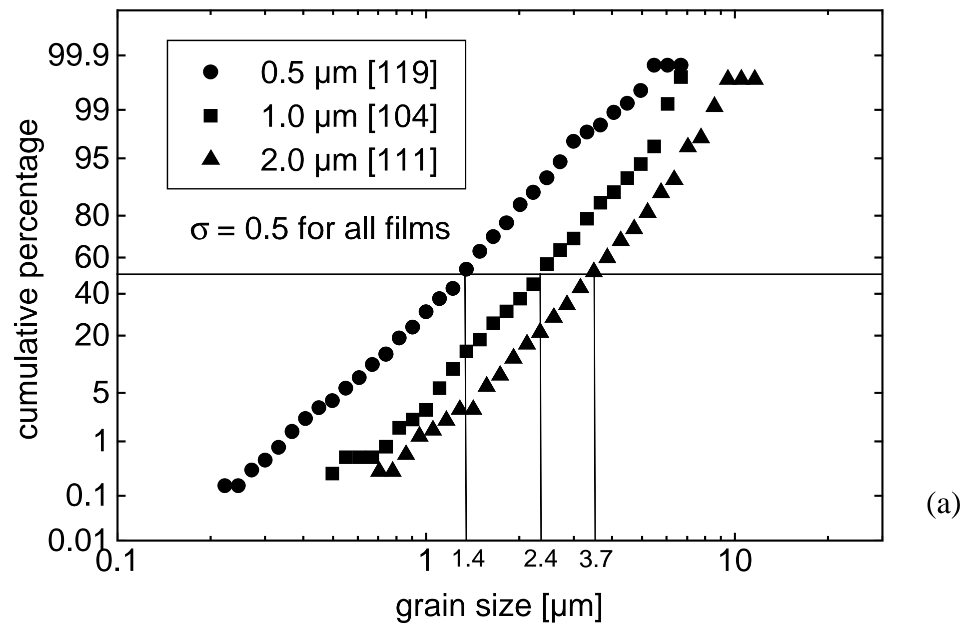

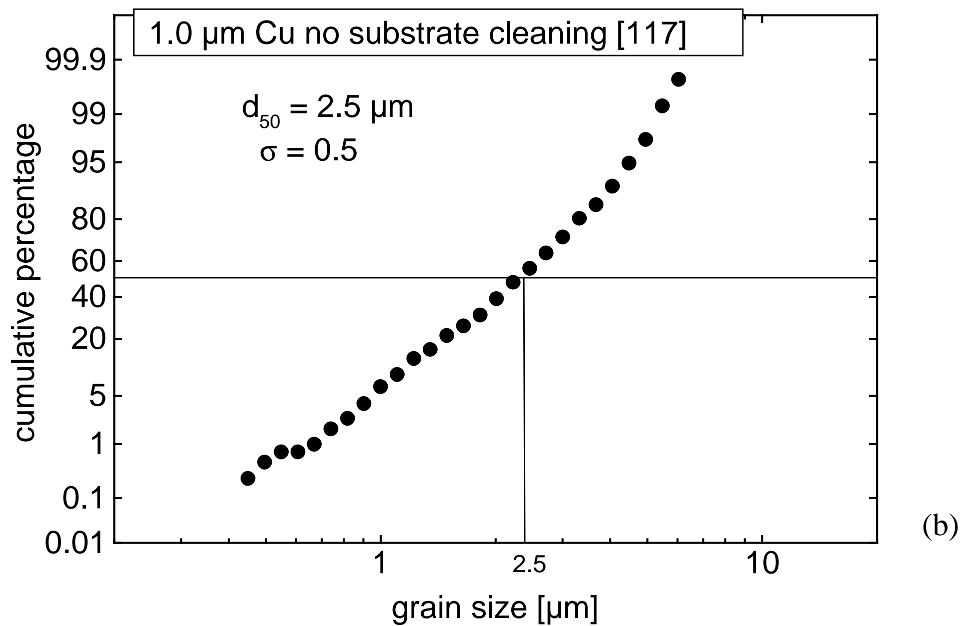

Figure 4-3 Grain size distributions for UHV-annealed (10 min at 600 °C) 0.5, 1.0 and 2.0 µm thick Cu films prepared with substrate cleaning (a) and for a 1.0 µm thick film prepared without substrate cleaning (b). The linear course of the data points indicate lognormal grain size distributions. The median grain size, d_{50}, increases with growing film thickness, while the lognormal standard deviation, σ, is equal for all films as indicated by the equal slope of each line. Substrate cleaning has no significant influence on the grain size distribution, as shown for 1 µm thick films.

Grain size in Cu films

film thickness (µm)	median grain size (µm)	average grain size (µm)	lognormal standard dev.	number of counted grains
0.5 [119]	1.4	1.5	0.50	632
1.0 [104]	2.4	2.6	0.50	375
1.0 [117] [a]	2.5	2.6	0.50	406
2.0 [111]	3.7	3.9	0.50	335

Table 4-1 Grain size data for the Cu films from Figure 4-3. The 1.0 µm film [a] was sputtered without substrate cleaning. The error of the median and average grain sizes is ± 0.1 µm, and the error of the lognormal standard deviation is ± 0.05.

Twins in Cu films

film thickness (µm)	twin boundary length/area (μm^{-1})	twin area/area	number of twins/area (μm^{-2})	number of counted twins
0.5 [119]	0.22	0.02	0.08	200
1.0 [104]	0.27	0.04	0.06	415
1.0 [117] [a]	0.43	0.07	0.10	665
2.0 [111]	0.29	0.10	0.03	437

Table 4-2 Results of an analysis of twin grains. The 1.0 µm film [a] was sputtered without substrate cleaning. The error of the values in the second column is ± 0.05 μm^{-1}, ± 0.01 for the third column, and ± 0.02 μm^{-2} for the fourth column.

Texture

A striking property observed with the UHV-sputtered and annealed Cu films was the strong and sharp (111)-texture. The influence of substrate cleaning by ion bombardment was studied. Θ–2Θ X-ray scans for 1 µm thick films sputtered with and without substrate cleaning are shown in Figure 4-4. Both films have a strong (111) texture. The spectrum in (b) has a small (100) component which is not visible in (a). A far more drastic difference, however, exists for the peak *widths* (Figure 4-5). The (111) texture of the film sputtered with substrate cleaning (a) was more than 5 times sharper than the (111) texture of the film sputtered without substrate cleaning (b). The texture of Cu films with different film thickness was similar to that of the 1 µm thick film. Texture was analyzed with the FIB. In a (111)-textured film, all grains appeared with the same grey scale in the FIB image, if the

sample tilt was 0°. The few (100) grains appeared black at a sample tilt of 0° due to the higher channeling depth for the Ga ions.

Combined FIB and OIM measurements

Not all grain boundaries in the annealed Cu films were visibly grooved. This is seen in the FIB micrograph in Figure 4-6 (a) (see also Figure 4-2). A local texture measurement of the same film area with the OIM technique (Figure 4-6 b) revealed that only high angle boundaries with tilt angles greater than 15° were visibly grooved. Both low angle bound a-ries with tilt angles less than 15° and twin boundaries did not form a visible groove. The statistics of grain boundary segments obtained from data evaluation with the OIM software is presented in Table 4-3.

OIM boundary statistics

Rotation angle	Counts
2.0° - 15.0°	492
15.0° - 180.0°	1897
Class	
Σ3	316

Table 4-3 Grain boundary statistics from the OIM measurement in Figure 4-6 (b). Each count belongs to one raster unit identifying a grain boundary segment. The counts of the Σ3-twin boundary segments are included in the statistics of the high angle boundaries (15.0° to 180.0°).

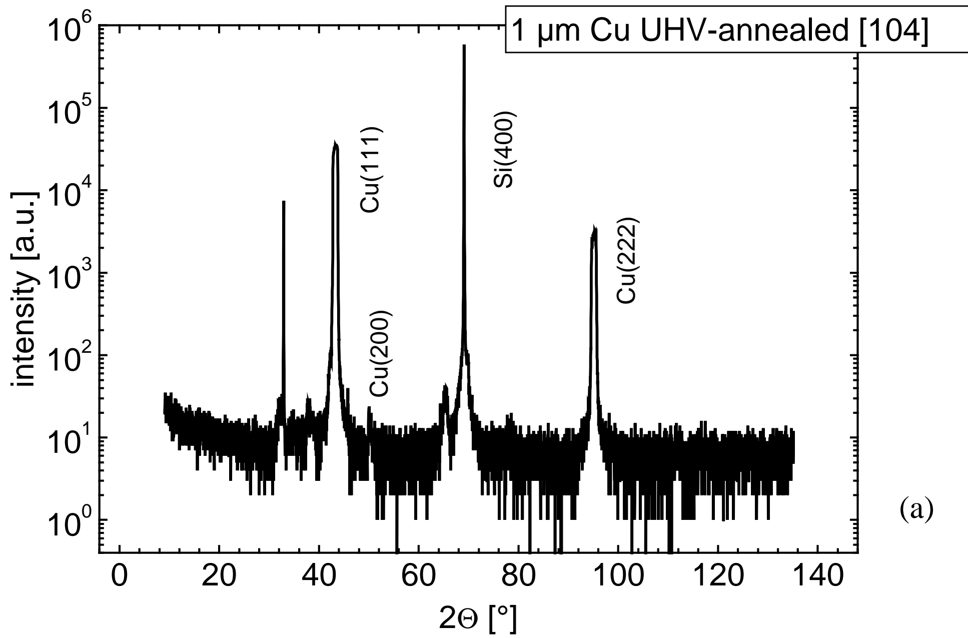

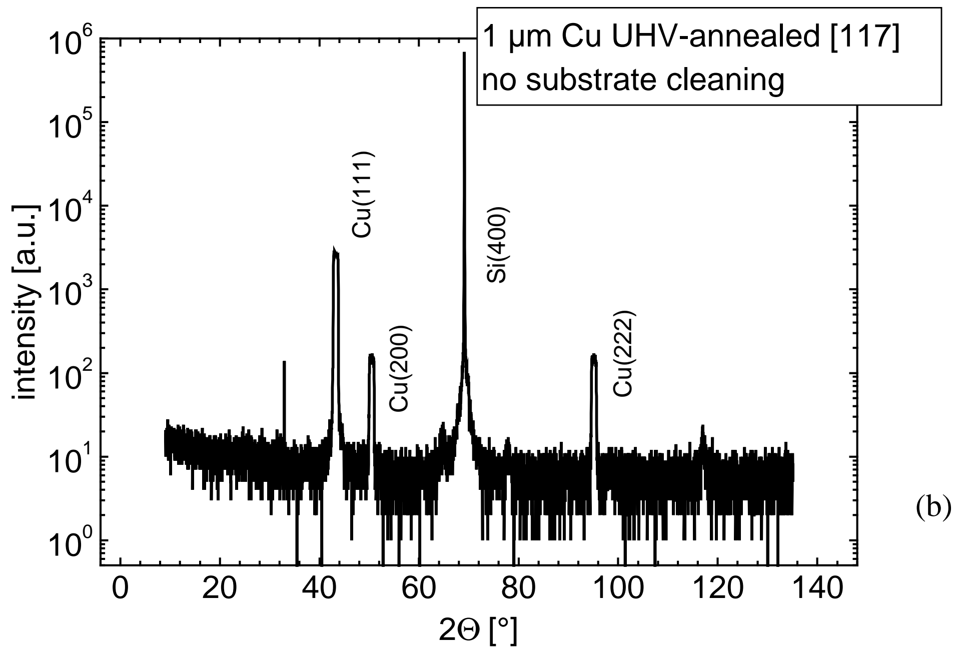

Figure 4-4 X-ray texture measurements (Θ–2Θ scan) of 1 µm thick Cu films, both UHV-annealed for 10 min at 600 °C. The film in (a) was sputtered with, the film in (b) was sputtered without pre-deposition substrate cleaning. The films are strongly (111) textured. The underlying Si substrate is visible in the spectrum, too. The film sputtered without substrate cleaning has a stronger (100) peak.

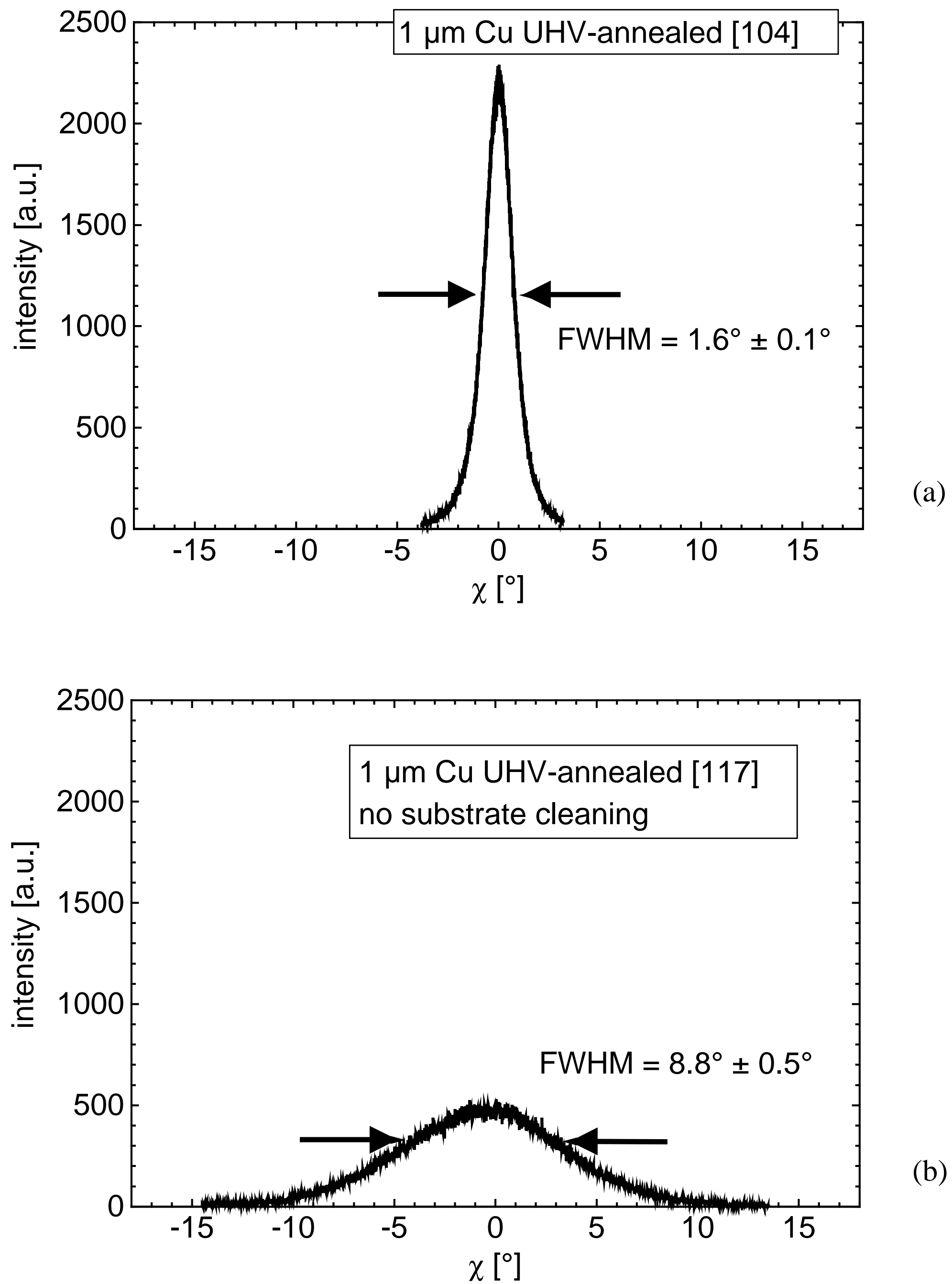

Figure 4-5 (a) Rocking curve for the (111) peak of the annealed Cu film sputtered with substrate cleaning. The texture is very sharp; the full peak width at half maximum intensity (FWHM) is 1.6°. The rocking curve for the (111) peak of the annealed Cu film sputtered without substrate cleaning in (b) exhibits a less sharp texture than the film sputtered with substrate cleaning (a).

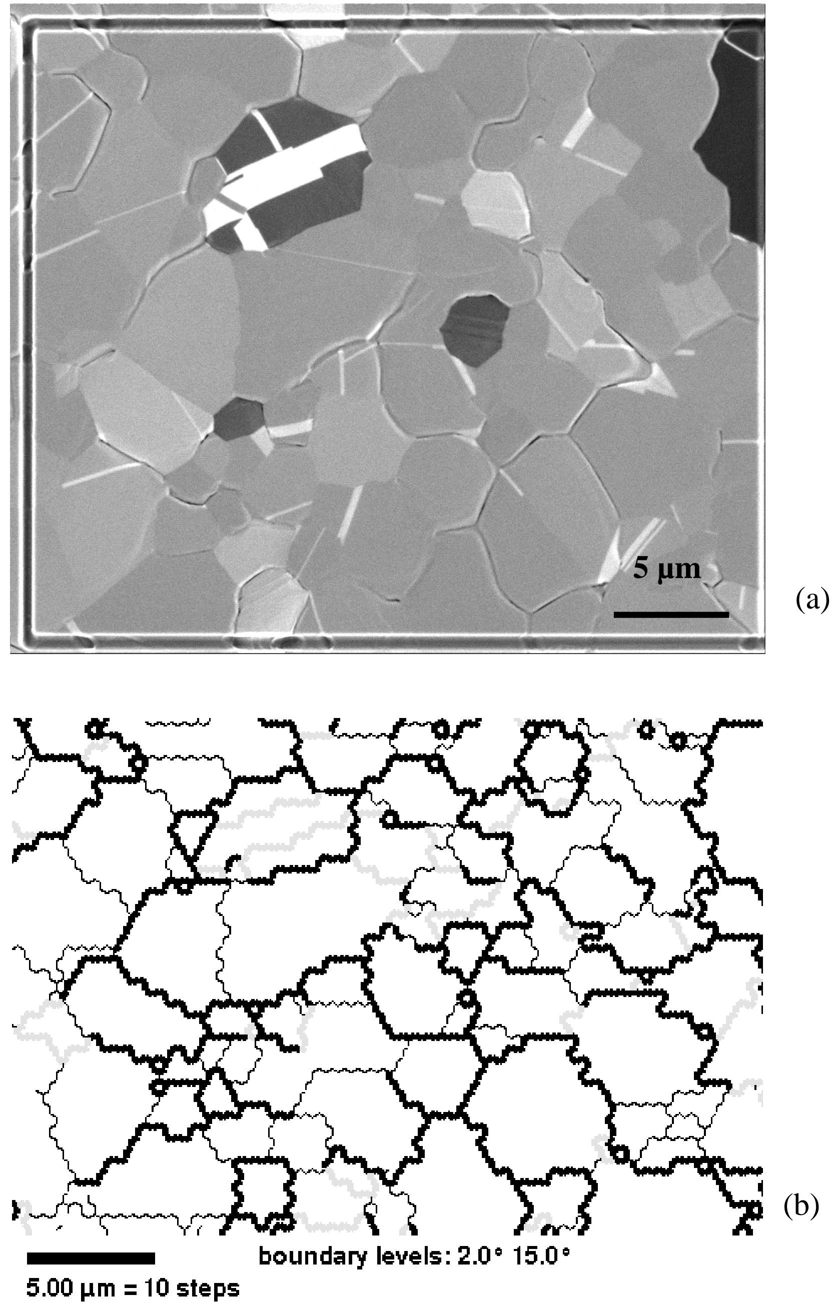

Figure 4-6 FIB micrograph (a) and grain boundary map (b), obtained from a local texture measurement with electron back-scattering diffraction (OIM software), of a 1 µm-thick annealed Cu film [104]. The region of interest was marked in the FIB. Only high angle boundaries with tilt angles >15° (represented by thick black lines in (b)) are decorated by grooves visible in (a). Both low angle tilt boundaries with tilt angles <15° (thin lines) and Σ3-twin boundaries (grey lines) are not visibly grooved. The sample in (a) is untilted. (100) grains appear black.

Oxidation experiment

In Figure 4-7, the FIB micrograph of a Cu film is shown which was oxidized at 600 °C after annealing. Ruggedly shaped patches centered on each grain can be seen. These structures are regarded as Cu_2O islands. Yang et al. (1998) reported on in-situ oxidation of Cu in TEM. The range of pressure and temperature was in the same range as applied for the film in Figure 4-7. In these experiments, the authors observed the formation of epitaxial Cu_2O islands. Coalescence of the oxide islands was reported as the oxygen dose increased. The position of the islands at the center of grains observed in this work is not understood. This experiment served as a reference experiment for comparison with the 1 µm thick Cu-1at.%Al film shown in Figure 4-19. In the alloy film, which was sputtered, annealed and oxidized under the same conditions as the pure Cu film in Figure 4-7, voids were found at grain boundaries and grain boundary triple junctions.

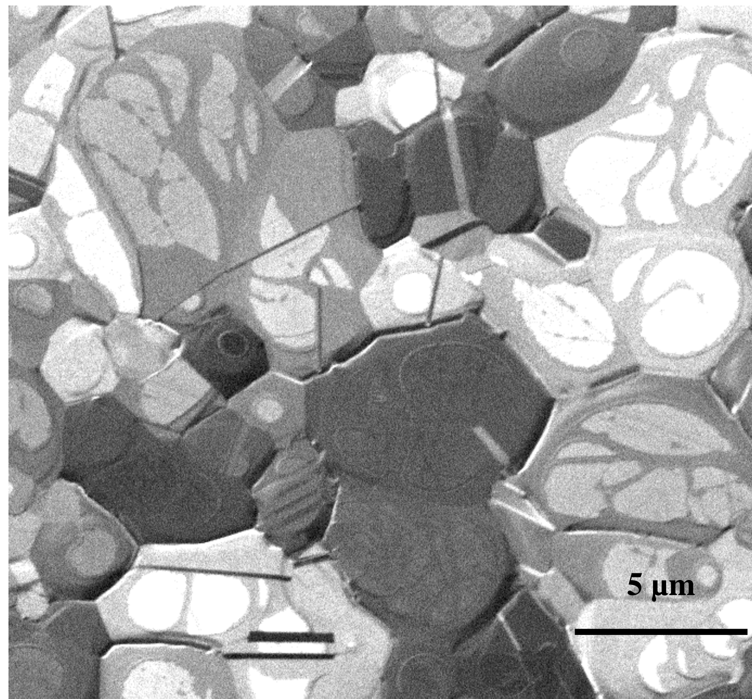

Figure 4-7 FIB micrograph of an oxidized 1 µm thick Cu film [097]. The sample tilt is 18°. After annealing at 600 °C, the film had been oxidized for 2 min at an oxygen pressure of 1×10^{-3} Pa. This corresponds to a dose of approximately 1000 L (Langmuir, 1 L = 1 s × 10^{-6} torr ≈ 10^{-4} Pa s; a rule of thumb states that exposure with 1 L corresponds to offering one monolayer of gas molecules to a surface). Structures of a lighter grey scale are centered on the grains. These structures, which are interpreted as Cu_2O islands, were easily sputtered off during FIB imaging.

4.1.2 HV-annealed films

Focused ion beam microscopy

In this work, several pure Cu films were annealed under HV conditions or under an inert gas atmosphere in the wafer curvature apparatus. The microstructure of these films, which had been sputtered under the same UHV-conditions, was not studied extensively. The formation of an oxide scale and of annealing hillocks was observed (Figure 4-8). Both features were not found in UHV-annealed films (Figure 4-2).

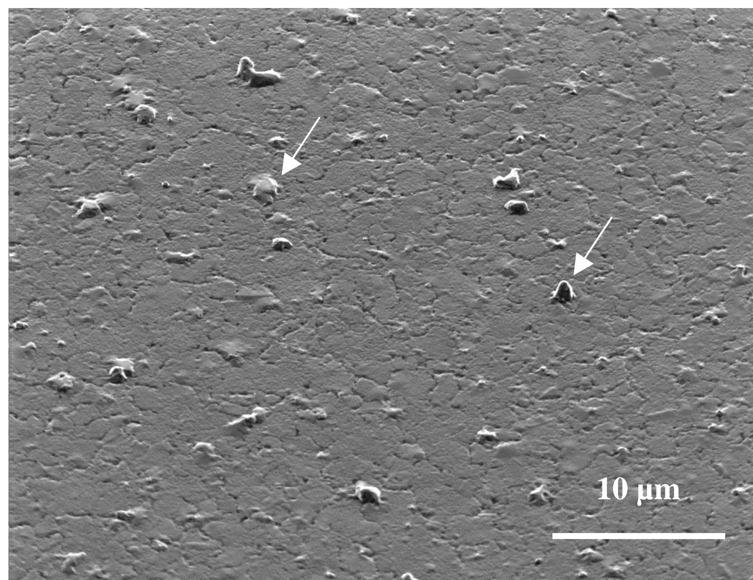

Figure 4-8 FIB micrograph of a 1 µm thick pure Cu film [052], annealed during five thermal cycles to 500 °C in the wafer curvature apparatus under an inert gas atmosphere. The sample tilt is 45°. No grain contrast is visible because of a thin amorphous or nanocrystalline surface layer which presumably was CuO_x. The surface layer was sputtered off during FIB imaging, after which grain contrast appeared. Annealing hillocks (arrows) can be seen, as well as grain boundary grooves.

4.2 Pure Cu films: Mechanical properties

4.2.1 UHV-annealed films

Wafer curvature measurements: The effect of film thickness

The wafer curvature method was applied to measure the thermo-mechanical properties of Cu films. All films had been UHV-annealed at 600 °C for 10 min in order to stabilize grain structure before thermal cycling. In Figure 4-9 to Figure 4-12, stress-temperature curves of 4 different films are shown. At the beginning of the experiment, all curves exhibit a tensile residual stress. The stress decreases linearly upon heating. In this segment, thermal strain is accommodated predominantly elastically. The departure of the curve from this so-called thermoelastic line indicates plastic yielding. A thermoelastic segment is found also at the onset of cooling. During cooling, plastic yielding occurs in the tensile stress region.

In Figure 4-9 to Figure 4-12, a strong film thickness effect is observed on the strength of the films as well as on the shape of the stress-temperature curves. The stress upon yielding increases for decreasing film thickness. This effect is less pronounced at 500 °C than at room temperature. This film thickness effect on yield stress has been observed by many authors for several film materials (see e.g. Venkatraman and Bravman 1992 for Al and Keller et al. 1998 for Cu).

Not only the film strength but also the *shape* of the curves changes with film thickness. The curve of the thinnest 0.3 µm thick film in Figure 4-9 exhibits two characteristic features: during heating, a stress drop is observed at (A) at about 250 °C, during cooling, a kink is observed at (B) at approximately 200 °C. These characteristic features become less pronounced with increasing film thickness.

The 0.5 µm thick film (Figure 4-10) was cycled four times. The first wafer curvature cycle was carried out approximately one day after UHV-annealing which was the case for all the other films presented in this section, too. The second cycle was carried out one day after the first cycle. This cycle begins at higher stress, it does not build up as high compressive stresses as during the first cycle. The third cycle, which was measured half a year later, looks similar to the first cycle. However, the characteristic stress drop at 250 °C extended over a larger region than in the first cycle. Before the fourth cycle, the film had been cooled for 5 min to 77 K in a liquid nitrogen bath. The small tensile stress at the beginning of the fourth cycle is due to plastic deformation during cooling to 77 K.

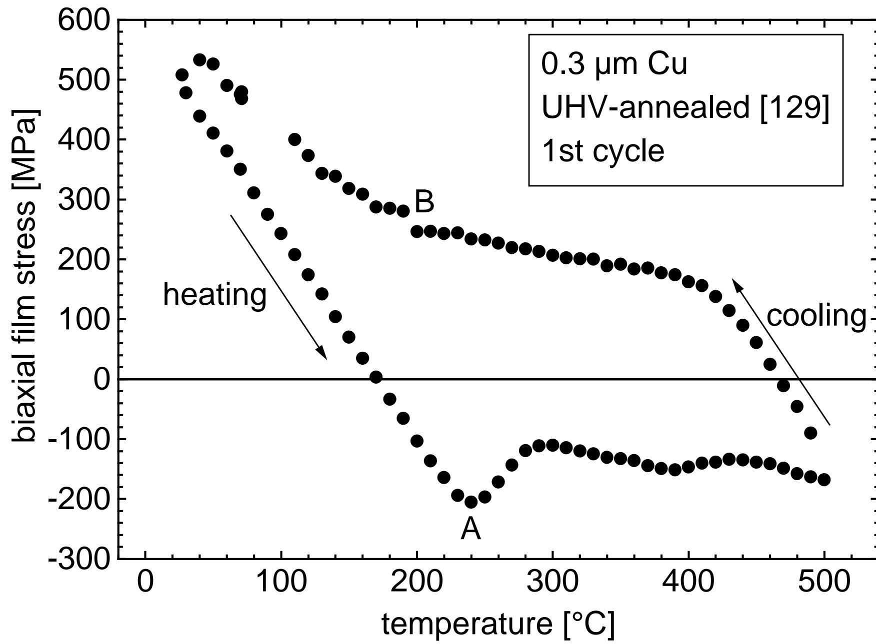

Figure 4-9 Stress-temperature curve for the first wafer curvature cycle of a 0.3 µm thick Cu film. After deposition, the film had been UHV-annealed at 600 °C in order to stabilize the grain structure before the wafer curvature experiment. The experiment was carried out under an inert gas atmosphere.

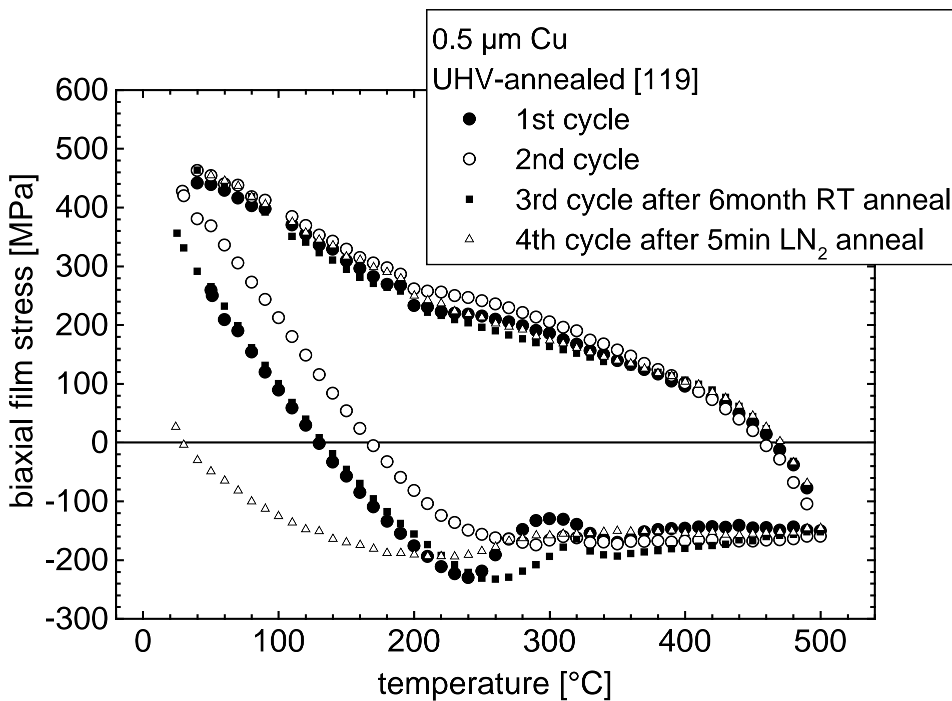

Figure 4-10 Stress-temperature curves for four different thermal cycles of a 0.5 µm thick UHV-annealed Cu film. Note that the maximum compressive stress between 200 and 250 °C is significantly lower for the second and for the fourth cycle.

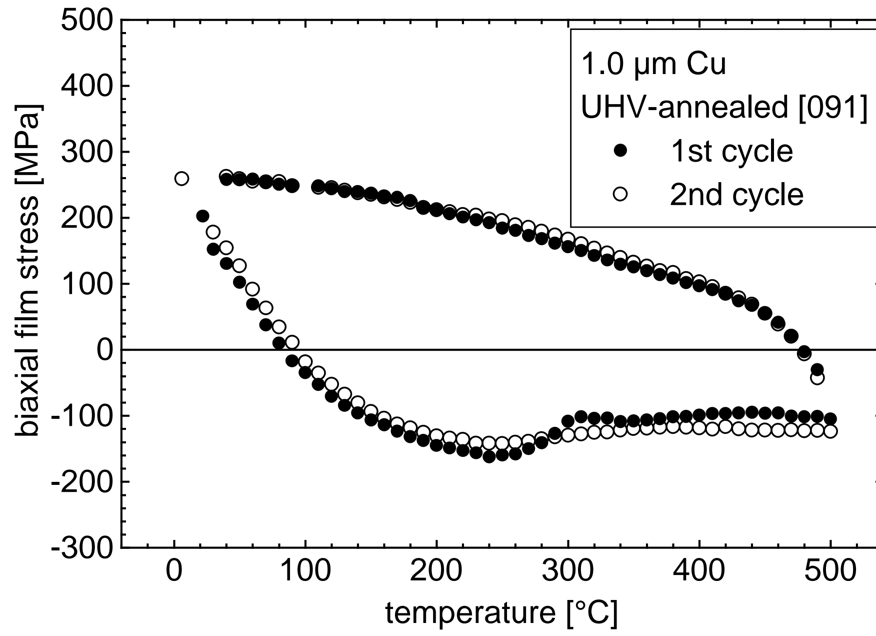

Figure 4-11 The first two wafer curvature cycles of a UHV-annealed 1.0 µm thick Cu film.

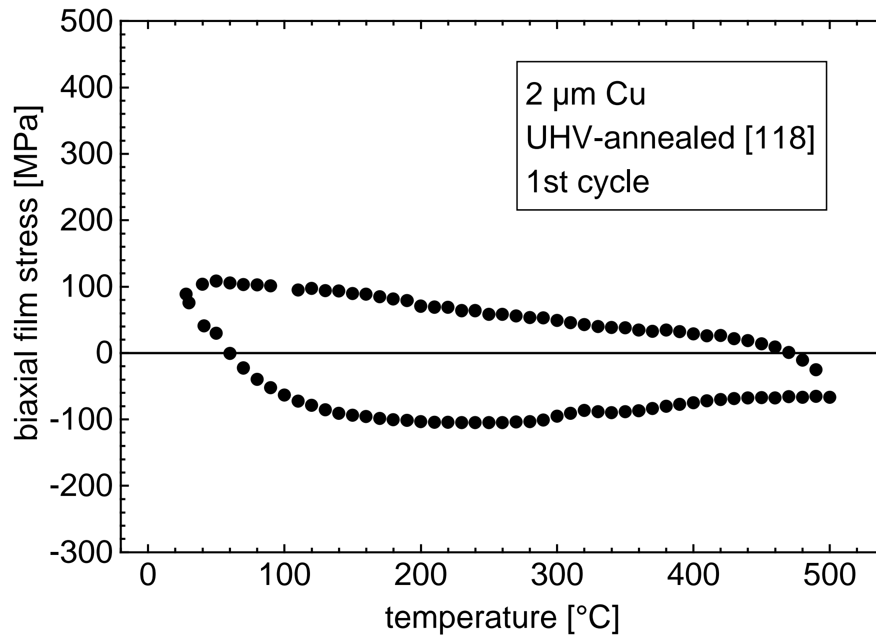

Figure 4-12 First wafer curvature cycle of a UHV-annealed 2.0 µm thick Cu film.

Wafer curvature measurements: The effect of substrate cleaning

The in-situ cleaning of the wafer surface before film deposition had a large influence on the film texture and on the density of twin grains (section 4.1.1). In this experiment, the influence onto substrate cleaning on the stress-temperature curve of the same film was determined. The stress-temperature curve is shown in Figure 4-13 together with the curve of the film sputtered on a cleaned substrate. The heating curves up to 350 °C look similar in both films. However, at higher temperatures stresses are lower in the film sputtered without substrate cleaning.

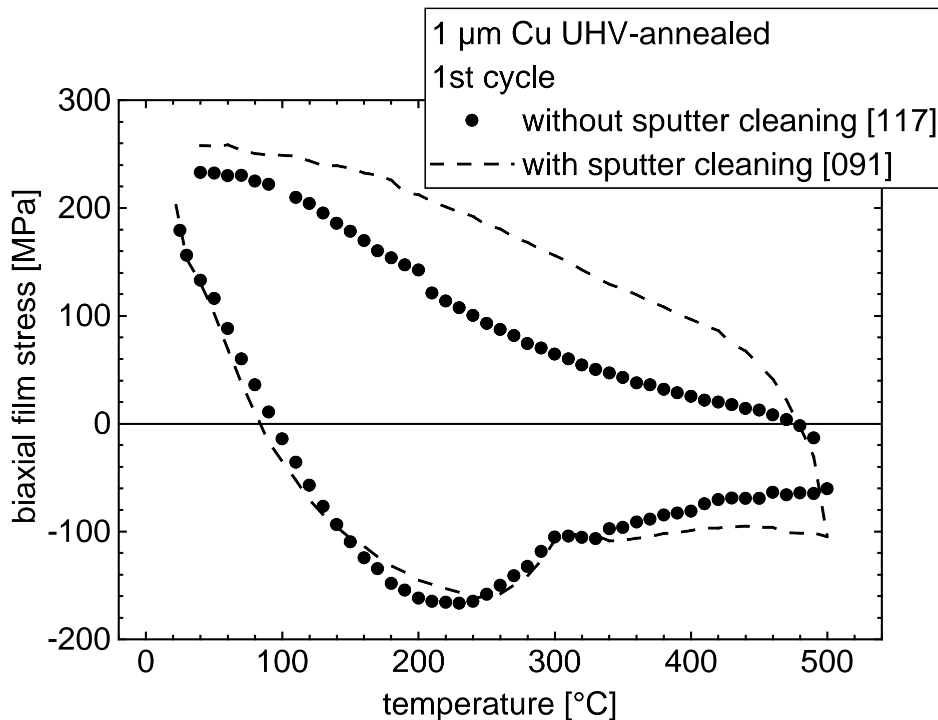

Figure 4-13 First wafer curvature cycle of a 1 µm thick UHV-annealed Cu film fabricated without in-situ sputter cleaning of the wafer surface. The first cycle of the corresponding film fabricated with sputter cleaning from Figure 4-11 is shown as a reference.

Nanoindenter measurements

The hardness of two UHV-annealed Cu films, 1 µm and 2 µm thick, was measured with the nanoindenter as a function of indentation depth (Figure 4-14). The 1 µm thick film is harder than the 2 µm thick film. Both curves indicate increasing hardness with increasing indentation depth. In section 4.2.2, more nanohardness measurements are shown for HV-annealed Cu films having a larger variety in film thickness.

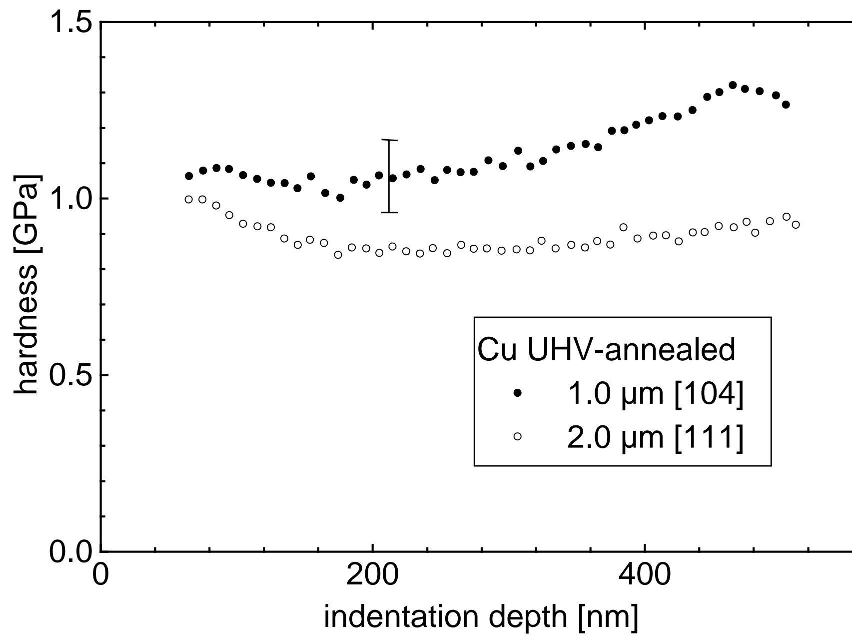

Figure 4-14 Nanohardness values versus indentation depth for 1 µm and 2 µm thick UHV-annealed Cu films. The measurements were carried out with a nanoindenter operated in the continuous stiffness mode. A Berkovich-type diamond tip was used. Each curve represents the average of 10 indentations at different sites. The error bar represents the standard deviation of the 10 indentations.

4.2.2 HV-annealed films

Wafer curvature measurements

In Figure 4-15, the first two wafer curvature cycles of a 1 µm thick as-sputtered Cu film are shown. Above 200 °C during the first heating cycle a large stress drop is observed. This stress drop is explained by thermally induced densification processes like grain growth and the annihilation of excess vacancies from the deposition process. The second wafer curvature cycle resembles the curve of the UHV-annealed 1 µm thick film, which is shown for comparison. The curve was reproducible during the third, fourth and fifth wafer curvature cycle.

In the third to fifth thermal cycles, isothermal stress relaxation experiments were carried out for this film (Figure 4-16). In these experiments, the temperature ramp was halted at a definite temperature, and the temperature was kept constant for 16 hours. Such experiments are suitable for the determination of the predominating stress relaxation mechanisms at a definite temperature. Isothermal stress relaxation experiments are similar to conventional creep experiments carried out under strain control.

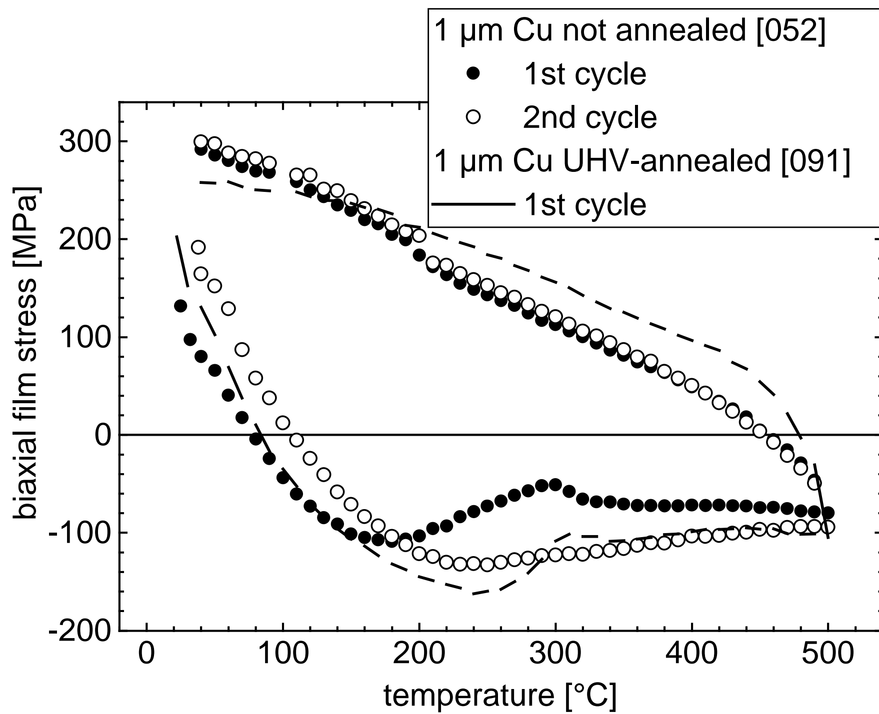

Figure 4-15 First and second thermal cycle for an as-deposited 1 µm thick Cu film. A stress drop during the first cycle is explained by densification processes. The stress-temperature curve of a corresponding UHV-annealed film is inserted as a reference.

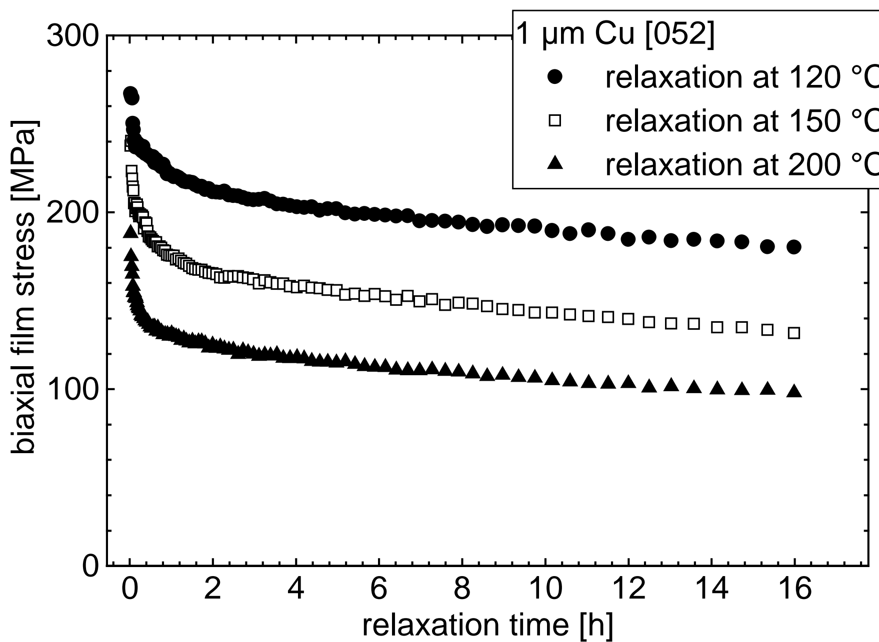

Figure 4-16 Isothermal stress relaxation curves for the film from Figure 4-15 measured during the third (200 °C), fourth (150 °C), and the fifth (120 °C) cooling cycle.

Nanoindenter measurements

Nanohardness was measured for 0.5 to 2.0 μm thick Cu films which had been annealed in high vacuum at 400 °C. Each curve shown in Figure 4-17 represents the averaged data for 10 indentations at different sites. It is observed that both the absolute hardness values and the hardening, i.e. the slope of the curves, increase with decreasing film thickness. The same trend was observed for the yield stress of pure Cu films in wafer curvature experiments in section 4.2.1.

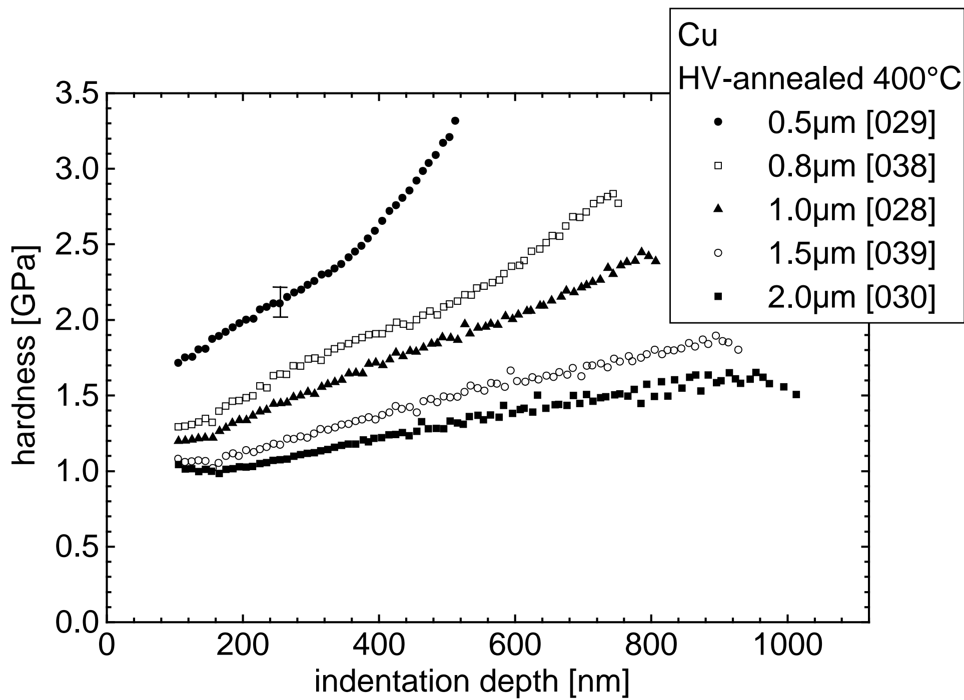

Figure 4-17 Hardness vs. indentation depth for Cu films of different thickness. The hardness was measured at room temperature with the nanoindenter working in the continuous stiffness mode. The films were HV-annealed for 1 h at 400 °C. The error bar represents the standard deviation of the 10 indentations.

4.3 Cu-Al films: Microstructure evolution

Dilute Cu-Al alloy films were produced by magnetron co-sputtering of Cu and Al targets in the same UHV sputtering chamber as used for the pure Cu films. Most films were subsequently annealed in UHV without breaking the vacuum in between. The aim was not to form a second phase by oxidation *before* grain growth was completed. Several films were oxidized after annealing.

4.3.1 UHV-annealed and oxidized films

Focused ion beam microscopy

First, the topography of the films was studied with the FIB. The FIB image in Figure 4-18 shows the microstructure of an unoxidized Cu-1at.%Al film which had been annealed in the UHV directly after film deposition. The microstructure looks identical to the microstructure of corresponding pure Cu films shown in Figure 4-2 and Figure 4-6 (a).

In Figure 4-19 to Figure 4-23, FIB images of oxidized 1 µm thick Cu-1at.%Al films are shown. With exception of the film in Figure 4-23, all films were first annealed in the UHV chamber, then oxidized at a specific temperature, and finally allowed to cool down in UHV. The most striking feature observed are voids at many grain boundaries and grain boundary triple junctions. This is the first time that such grain boundary voids were observed in thin films. Similar voids have been found on grain boundaries of polycrystalline bulk creep specimens ("creep voids"). No oxide islands, which were seen in the pure Cu film in Figure 4-7, have formed. Void growth is correlated with the oxidation temperature, which is seen in Figure 4-19 to Figure 4-21. Many grain boundaries and triple junctions were voided in the film oxidized at the maximum temperature of 600 °C (Figure 4-19). In the film oxidized at 500 °C (Figure 4-20), only grain boundary triple junctions were voided. Finally, the film annealed at the lowest temperature of 400 °C (Figure 4-21) was not voided.

The respective oxidation times and oxygen partial pressures, found in the figure captions, were selected on the basis of the calculation of the velocity of the internal oxidation front, plotted in Figure 2-3. The oxygen partial pressure was chosen such that the total dose of oxygen molecules impinging on the film surface during annealing was sufficient to oxi-

dize all Al atoms within a film; kinetic gas theory was applied for this calculation assuming a low sticking coefficient of 0.1 to allow for abundant oxygen delivery.

The film shown in Figure 4-22 was annealed for a long period at 550 °C after oxidation at 600 °C. The purpose of this experiment was to find out which effect prolonged annealing after film oxidation had on void growth. The FIB micrograph shows a bimodal void size distribution of large voids with diameters of up to 5 µm, and voids at grain boundaries and triple junctions which looked similar to the voids in the film shown in Figure 4-19. No explanation for the growth mode of the large voids was found. The film shown in Figure 4-23 was oxidized under an inert gas atmosphere in the wafer curvature machine. Void shape is different in this film if compared to the voids in the films oxidized and annealed in the UHV-chamber.

It can be concluded that grain boundary voids were found in Cu-Al alloy films which were oxidized at temperatures above 500 °C. Neither oxidized pure Cu films nor Cu-Al films, which were only annealed but not oxidized, were damaged by voids.

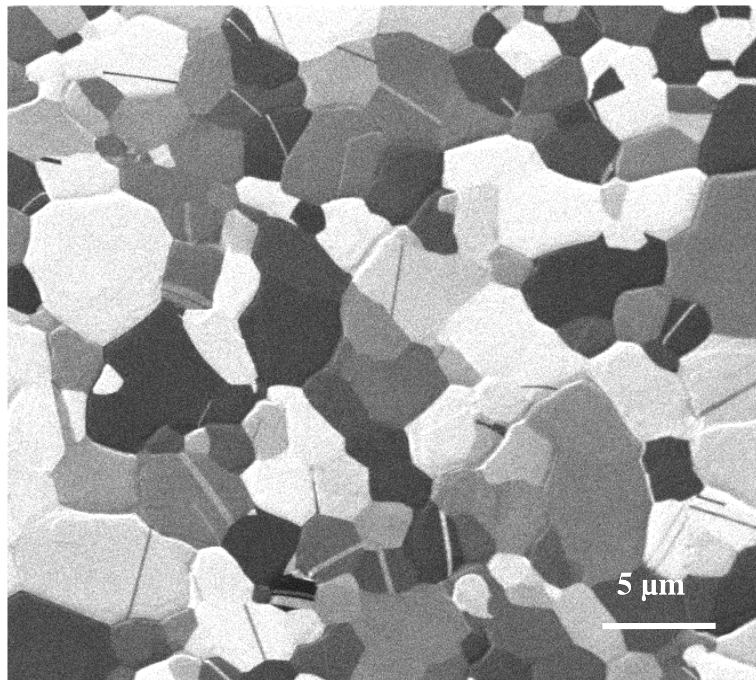

Figure 4-18 FIB micrograph of a 1 µm thick Cu-1at.%Al film which was annealed in the UHV-chamber for 10 min at 600 °C directly after sputtering [095]. The sample tilt is 17°.

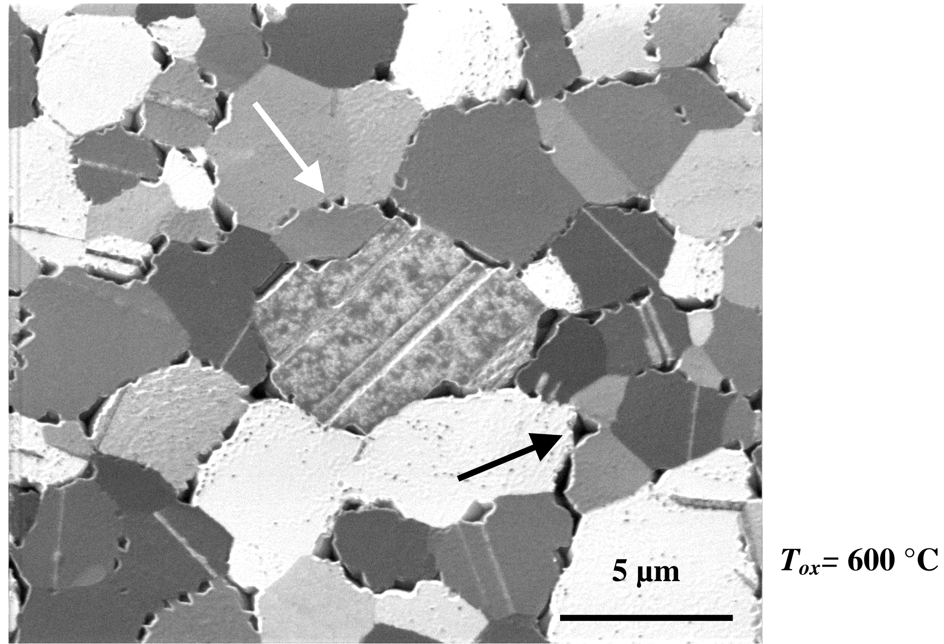

Figure 4-19 FIB micrograph of a 1 µm thick Cu-1at.%Al film, oxidized for 2 min at 600 °C at an oxygen pressure of 1×10^{-3} Pa [096]. The film had been annealed at 600 °C for 10 min before oxidation. Two different types of voids are distinguished: small circular voids at grain boundaries (white arrow) and large voids at triple junctions (black arrow). The sample tilt is 17°. The very different topography of a 1µm thick *pure* Cu film, oxidized under similar conditions, is shown in Figure 4-7.

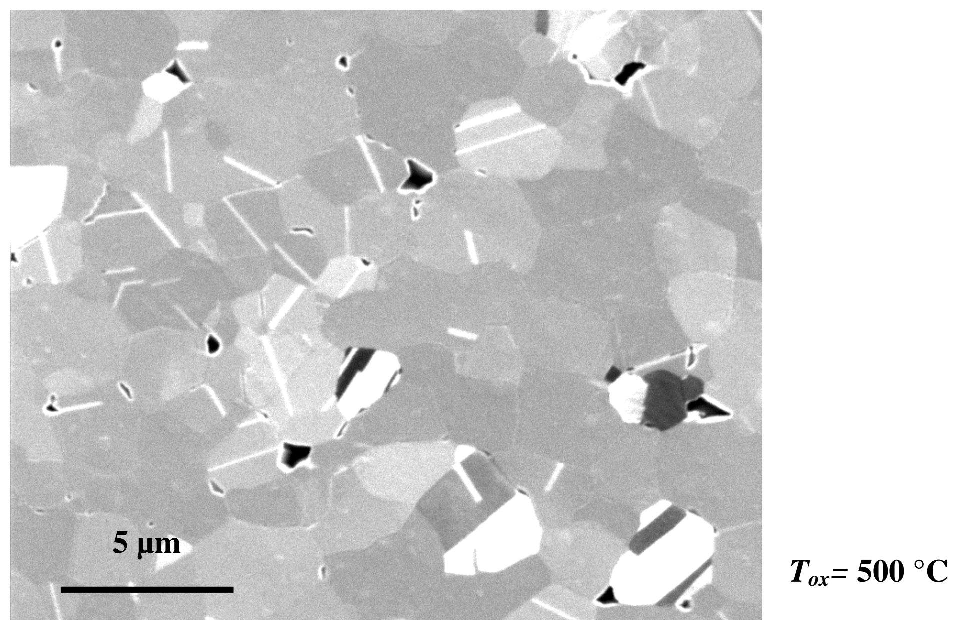

Figure 4-20 FIB micrograph of a 1 µm thick Cu-1at.%Al film, annealed and oxidized at 500 °C for 30 min at an oxygen pressure of 1×10^{-5} Pa [102]. Fewer voids have formed than in the film in Figure 4-19; the voids appear as black structures with white rims. The sample tilt was 0°, which is why the orientation contrast between (111)-grains is low.

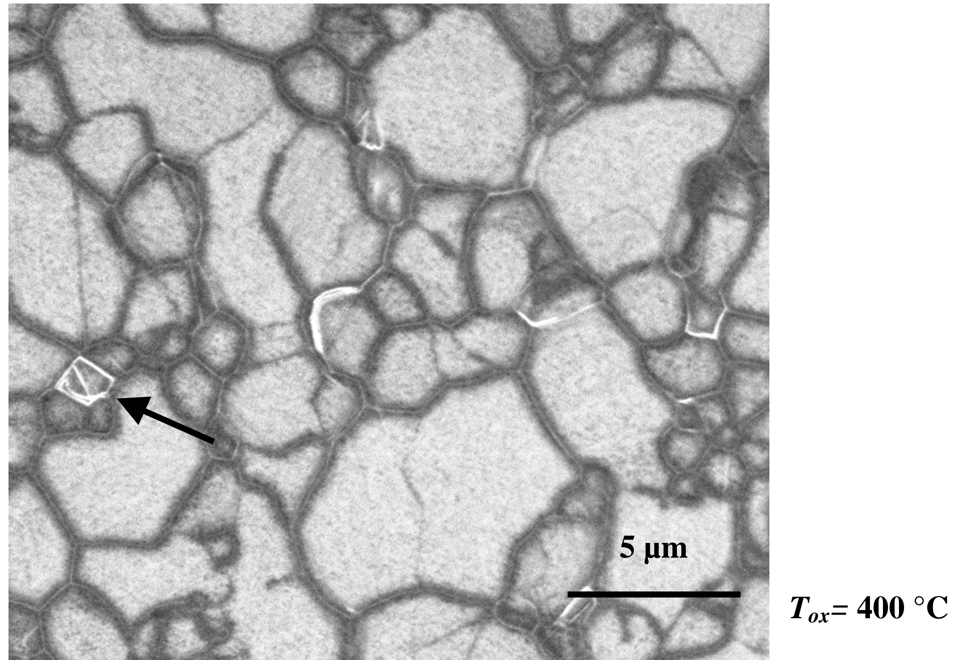

Figure 4-21 FIB micrograph of a 1 µm thick Cu-1at.%Al film, annealed at 600 °C and oxidized at 400 °C for 6 h at an oxygen pressure of 1×10^{-5} [105]. No grain boundary voids can be seen. A dense oxide scale which appears dark at grain boundaries and few facetted protrusions (arrow) can be seen. The sample tilt is 0°.

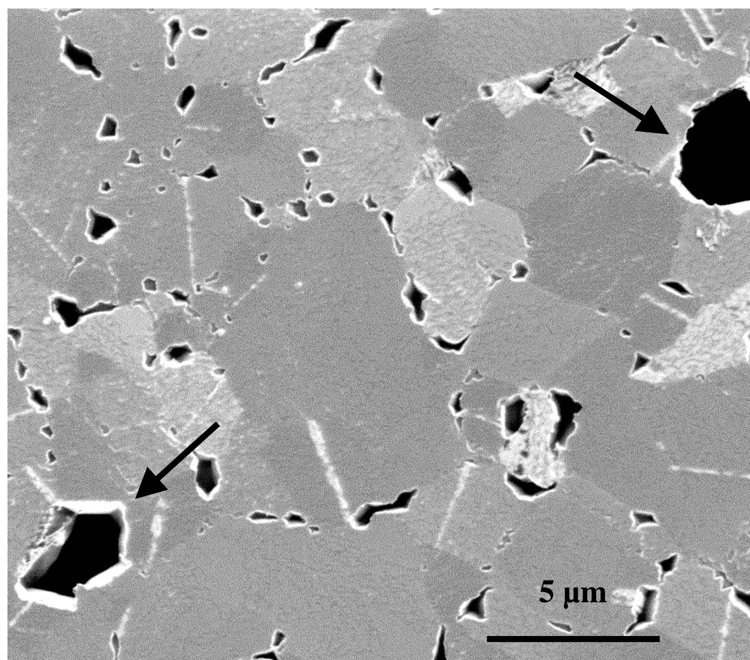

Figure 4-22 FIB micrograph of a 1 µm thick Cu-1at.%Al film, annealed and oxidized (2 min, 1×10^{-3} Pa) at 600 °C, and subsequently annealed for 6 h at 550 °C [106]. Few very large holes reaching down to the substrate (arrows) can be seen. The sample tilt is 0°.

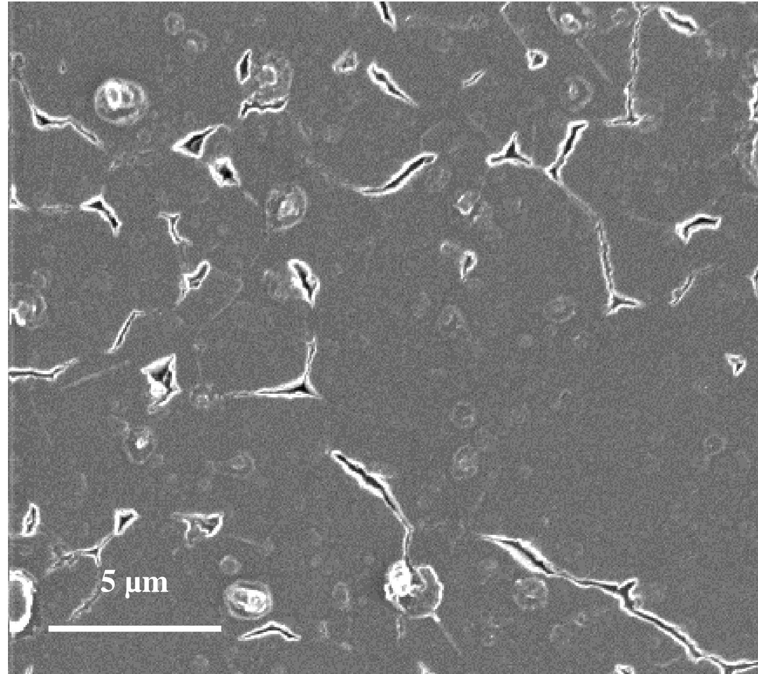

Figure 4-23 FIB micrograph of a 1 µm thick Cu-1at.%Al film, UHV-annealed for 10 min at 600 °C and oxidized ex-situ in the wafer curvature apparatus for 5 min at 600 °C under an inert gas atmosphere [116]. The voids in this film are crack-like. The dark tone of the image and the missing grain contrast is due to an oxide scale.

Transmission electron microscopy

TEM analysis of the oxidized Cu-1at.%Al film from Figure 4-19 revealed that the formation of aluminum-oxide particles by internal oxidation was not achieved. A very fine dispersion of small objects producing a coherency strain contrast are seen in the TEM bright field micrograph in Figure 4-24 (arrows); however, the same contrast was observed in TEM specimens of annealed *pure* Cu films, which is why the objects marked with arrows in Figure 4-24 are not interpreted as aluminum-oxide particles. This contrast probably resulted from defects in the matrix resulting from TEM sample preparation by ion milling. Instead of being internally oxidized, Al segregated to the film surface and oxidized there, as shown below.

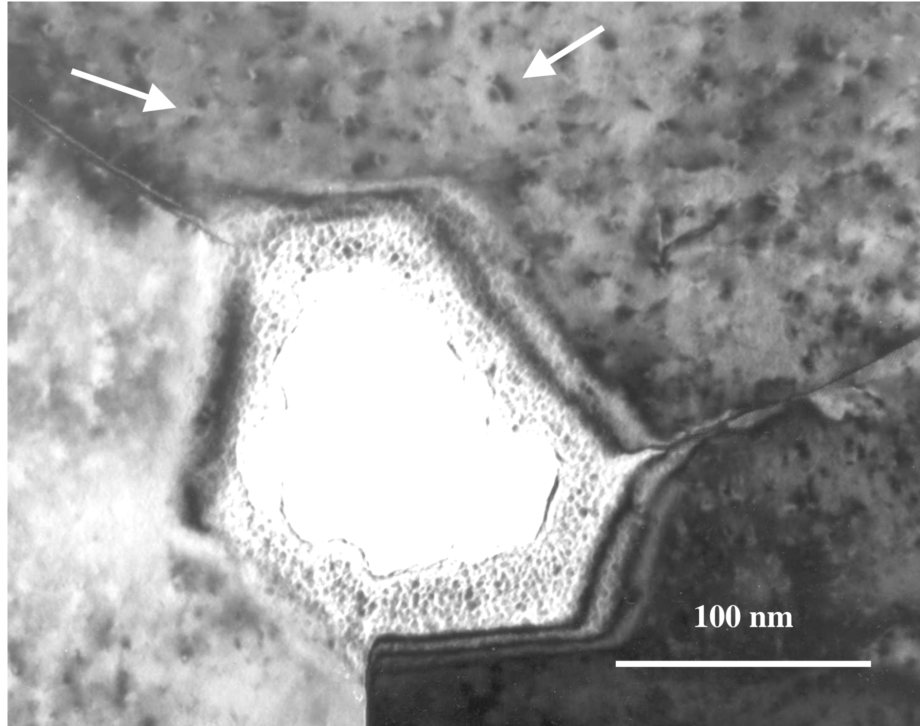

Figure 4-24 TEM bright field micrograph of the oxidized Cu-1at.%Al film from Figure 4-19 [096]. A void with facetted side walls is seen at a grain boundary triple junction. Small objects with a characteristic strain field contrast within the grains (arrows) are interpreted as radiation damage from TEM sample thinning. The same contrast was also observed in pure Cu films.

Grain size and twins

The grain size distribution and the distribution of twin grains was analyzed for the UHV-annealed Cu-1at.%Al film shown in Figure 4-18. It was confirmed that neither grain size nor the density of twin grains boundaries was influenced by the alloying. The grain size distribution shown in Figure 4-25 is characterized by both the same median grain size (2.4 µm) and lognormal standard deviation (0.5) as the appropriate pure Cu film (Table 4-1). Twinning was shown to be not affected by alloying of 1 at.% Al either (Table 4-4).

Texture

The third property not influenced by Al alloying was texture. The alloy film had a strong (111) texture as shown in Figure 4-26. The rocking curve of the (111) peak in Figure 4-27 had the same width as the curve of the corresponding pure Cu film in Figure 4-5 (a). It can be concluded that both quantitative microstructure analysis and texture analysis showed that the microstructure of a 1 µm thick Cu film is not altered by the alloying of 1 at.% Al.

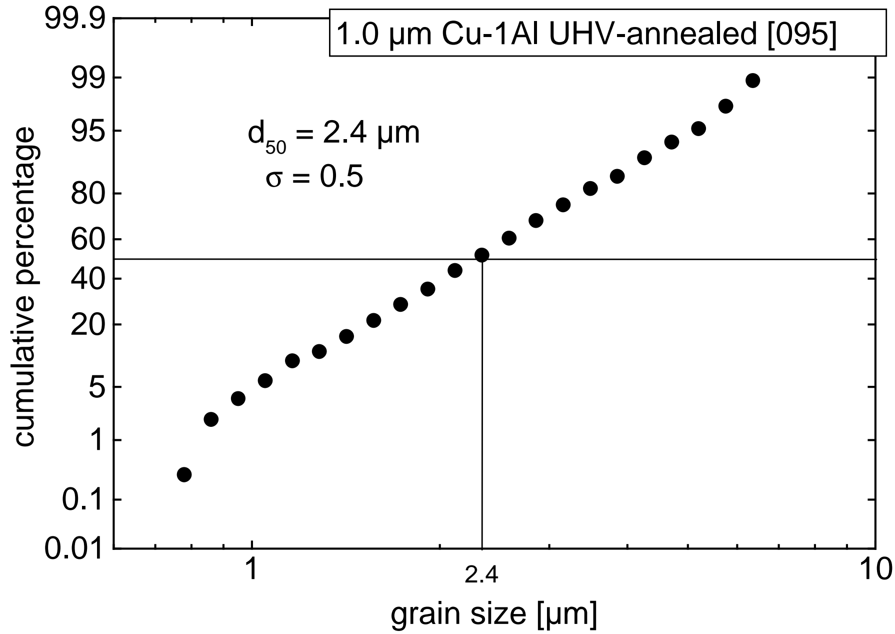

Figure 4-25 Grain size distribution in a 1 µm thick Cu-1at.%Al film, UHV-annealed for 10 min at 600 °C. The lognormal distribution is characterized by a median grain size of 2.4 µm and a lognormal standard deviation of 0.5. The distribution is equal to that of the 1 µm thick pure Cu film, Figure 4-3.

Twins in Cu-Al and Cu films

	twin boundary length/area (μm^{-1})	twin area/area	number of twins/area (μm^{-2})	number of counted twins
1at.%Al [095]	0.22	0.03	0.05	369
pure Cu [104]	0.27	0.04	0.06	415

Table 4-4 Analysis of twin grains in an UHV-annealed Cu-1at.%Al film. The corresponding data for the pure Cu film are inserted for comparison. Film thickness is 1 µm for both films. Twin densities are, within the error bar, equal for Cu-Al and pure Cu. The respective errors of the values are ± 0.05 μm^{-1} for the second column, ± 0.01 for the third column and ± 0.02 μm^{-2} for the fourth column.

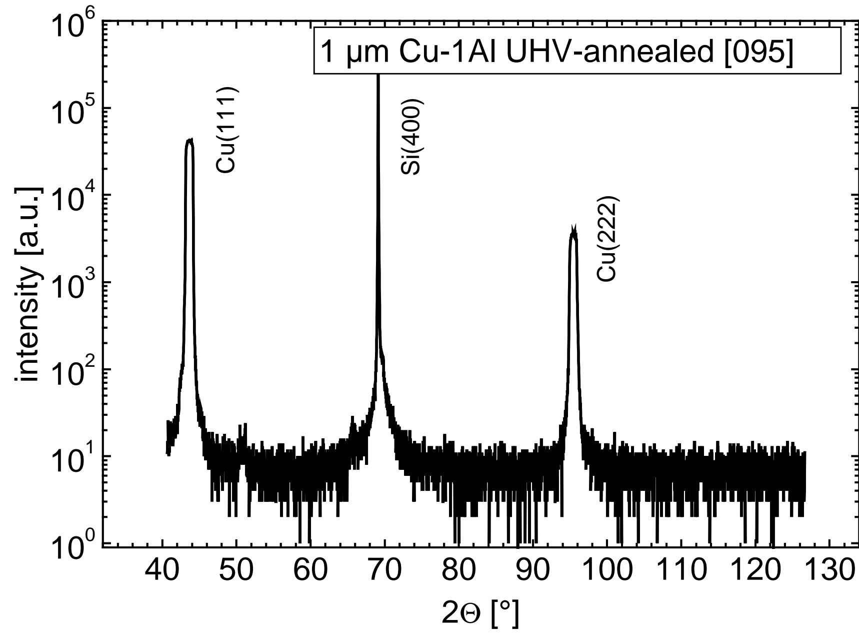

Figure 4-26 The Θ–2Θ scan of a 1 µm thick Cu-1at.%Al film shows a strong (111) texture.

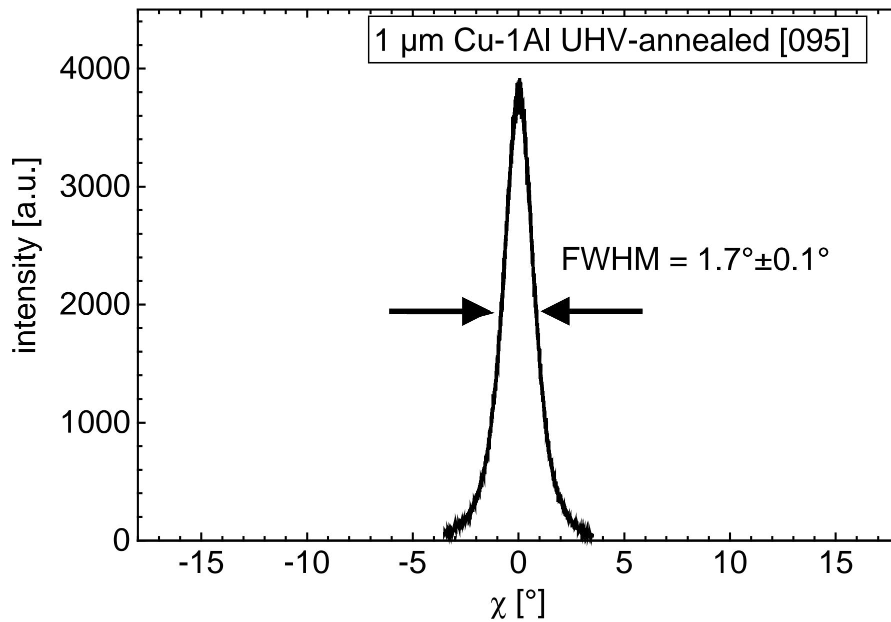

Figure 4-27 The texture of the film shown in Figure 4-26 is very sharp (rocking curve of the (111) peak).

Combined FIB and OIM measurements

Not all grain boundaries in the oxidized Cu-Al films were voided. A relationship between voiding and the local texture could be established by texture mapping of a specific area with OIM which had been imaged and marked in the FIB. Comparison of the FIB micro-graph in Figure 4-28 (a) and the corresponding grain boundary map (b) shows that high angle boundaries with tilt angles larger than 15° were almost entirely decorated by voids, whereas low angle boundaries with tilt angles less than 15° and twin boundaries were not voided. A similar texture dependency was found for grain boundary grooves in annealed pure Cu films (see Figure 4-6).

OIM boundary statistics

Rotation angle	Counts
2.0° - 15.0°	718
15.0° - 180.0°	1444
Class	
Σ3	332

Table 4-5 Grain boundary statistics from the OIM measurement in Figure 4-28 (b). Each count belongs to one raster unit identifying a grain boundary segment. The counts of the Σ3-twin boundary segments are included in the statistics of the high angle boundaries (15.0° to 180.0°).

Auger depth profiling

During oxidation of a Cu-Al alloy film, a part of the Al segregated and oxidized at the film surface. This can be seen in the Auger depth profile in Figure 4-29 (a). Al surface segregation continued during thermal cycling in the wafer curvature apparatus. Surface layers found in FIB images (Figure 4-21 and Figure 4-23) are interpreted as aluminum-oxide segregation layers. The self-passivation of the Cu-Al alloy films is held to be responsible for the non-achievement of internal oxidation in these films.

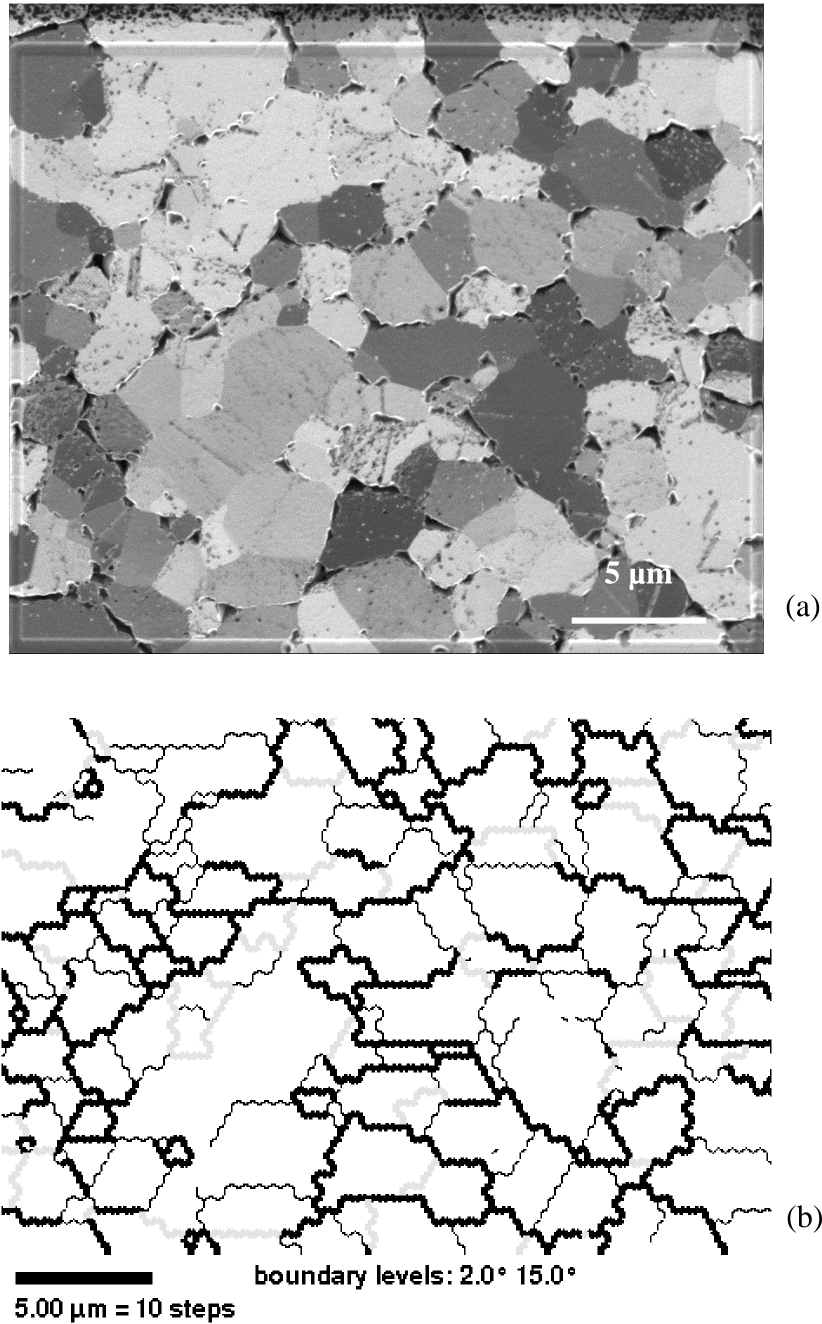

Figure 4-28 FIB micrograph (a) and grain boundary map (b), obtained from a local texture measurement with electron back-scattering diffraction (OIM software), of a 1 µm-thick UHV-annealed and oxidized Cu-1at.%Al film [096]. The region of interest was marked in the FIB. Only high angle boundaries with tilt angles >15° (represented by thick black lines in (b)) are voided (a). Both low angle tilt boundaries with tilt angles <15° (thin lines) and Σ3-twin boundaries (grey lines) are not voided. The sample tilt in (a) is 16°.

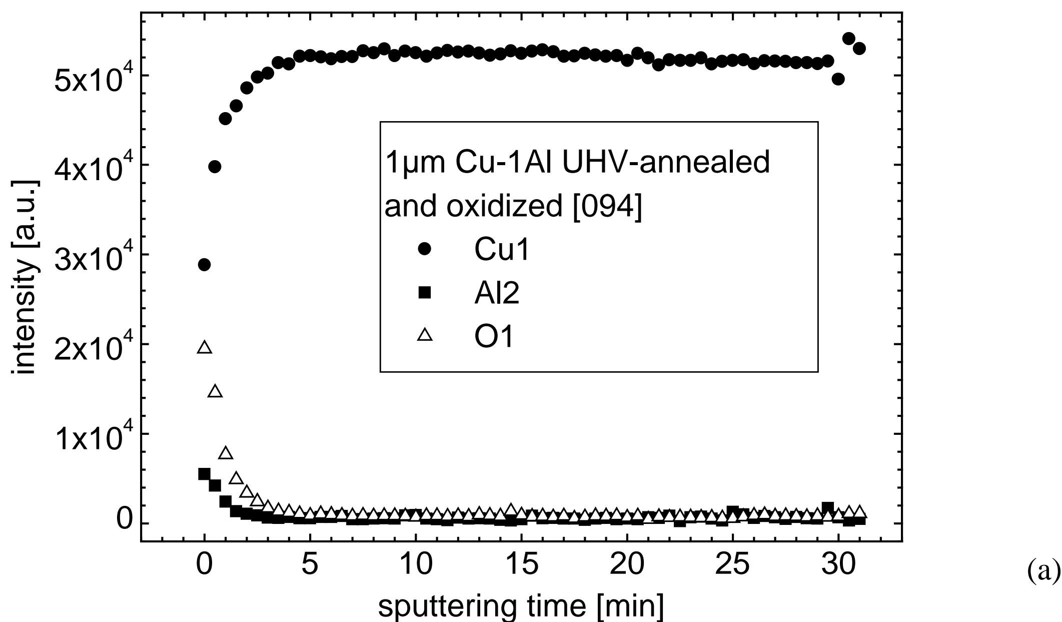

(a)

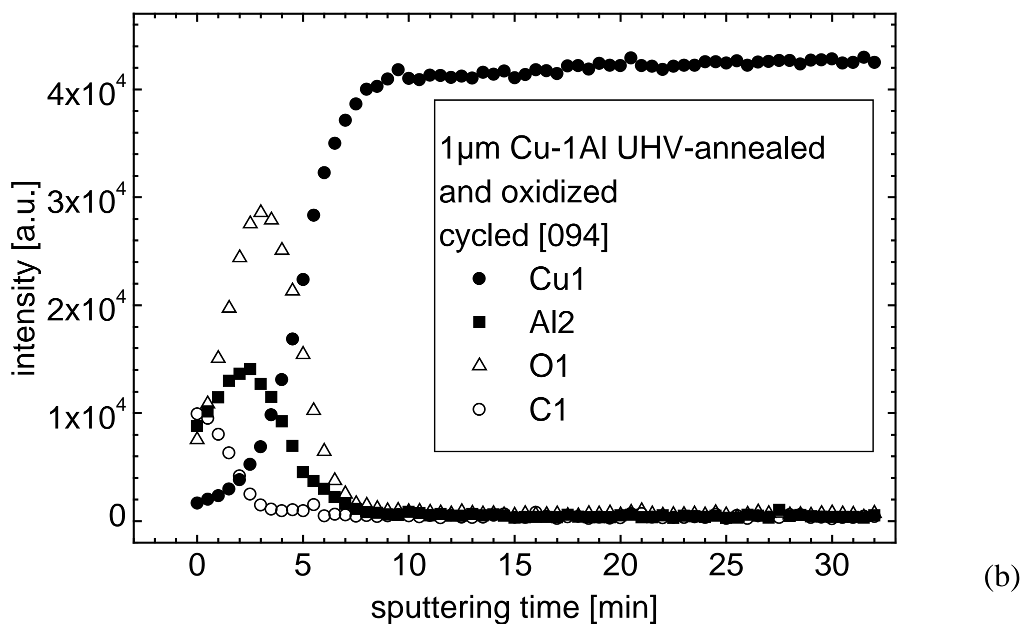

(b)

Figure 4-29 (a) Auger depth profile of an annealed and oxidized (10 s at 1×10^{-3} Pa at 600 °C) 1 µm thick Cu-1at.%Al film. The film was voided at grain boundaries. (b) Auger depth profile of the same film after thermal cycling under an inert gas atmosphere in the wafer curvature apparatus. The sputtering rate of 1.1 nm/min was calibrated for TaO_2. A surface layer about 1 nm thick with an increased Al- and O-concentration is found in the as-fabricated film (a) which became thicker (about 5 nm) after thermal cycling (b).

4.3.2 HV-annealed films and reactively sputtered films

Auger depth profiling

Several 1 μm thick Cu-Al films with different Al-concentration were thermally cycled in the as-deposited state. An Auger depth profile of a film alloyed with 5 at.% Al is shown in Figure 4-30. During thermal cycling under inert gas atmosphere, Al segregated and ox i-dized at the film surface. The aluminum-oxide surface layer is approximately twice as thick than in the case of the 1at.%Al film in Figure 4-29 (b).

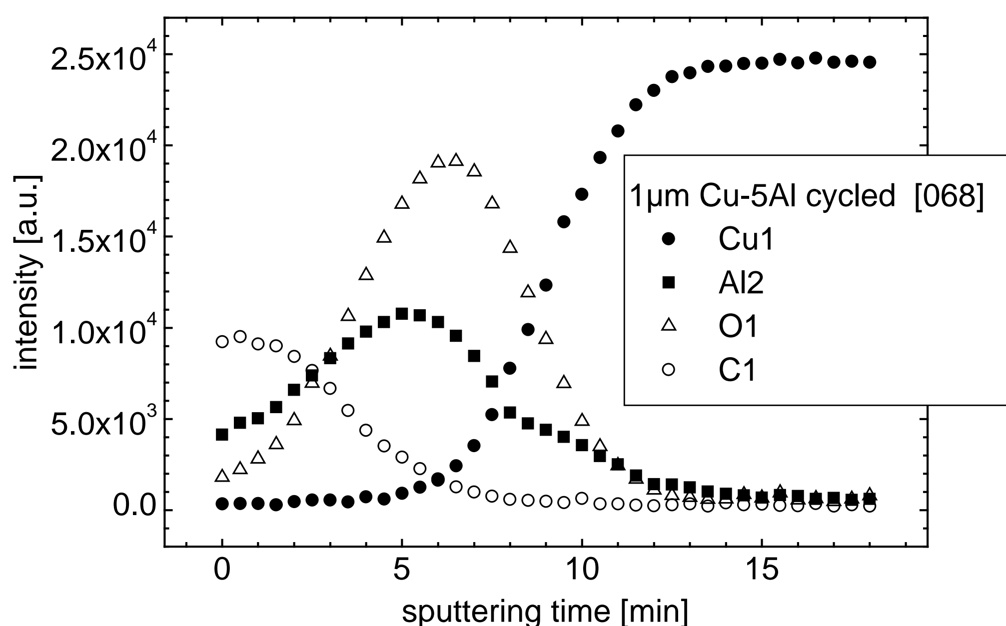

Figure 4-30 Auger depth profile of a 1 μm thick Cu-5at.%Al film which was thermally cycled to 500 °C under an inert gas atmosphere. The film was cycled in the as-deposited state. The sputtering rate of 1.1 nm/min was calibrated for TaO_2. A surface layer containing Al, O and C approximately 10 nm thick was found.

Films reactively sputtered with oxygen

Three Cu-Al films were reactively sputtered at different oxygen partial pressures in order to oxidize the Al during film growth. The presence of oxide (either Al or Cu oxide) in the film *before* annealing was expected to have a strong influence on grain growth. The films were sputtered at oxygen partial pressures of 1×10^{-5} Pa, 1×10^{-3} Pa, and 1×10^{-2} Pa, respectively. The oxygen pressure could not be measured during sputtering. However, it was found that it had decreased by about one order in magnitude directly after sputtering, and the pressure increased to the original value within minutes after sputtering. The decrease of

the oxygen partial pressure during sputtering is explained by oxygen gettering of the sputtered atoms.

The microstructure of the film [081] sputtered at the lowest oxygen partial pressure of 1×10^{-5} Pa was not further investigated. The thermo-mechanical behavior of this film was similar to that of a film sputtered without oxygen (section 4.4.2). It is assumed that the oxygen content was too small to alter the film properties. A second film was sputtered at a higher oxygen pressure of 1×10^{-3} Pa. The microstructure of this film was examined with FIB after thermal cycling to 500 °C in the wafer curvature apparatus (Figure 4-31). The film was small grained. The grains were non-columnar. Many hillocks were found on the film surface. This film supported very high stresses in the wafer curvature measurement (section 4.4.2). The third film [085] was sputtered at the highest oxygen partial pressure of 1×10^{-2} Pa. FIB examination revealed a bimodal grain size distribution of very small grains and large abnormally grown grains with diameters of several microns. This film supported only low stresses in wafer curvature measurements (section 4.4.2). These experiments showed that oxygen present in the as-sputtered film has a large influence on grain growth. Further experiments of this type were not performed.

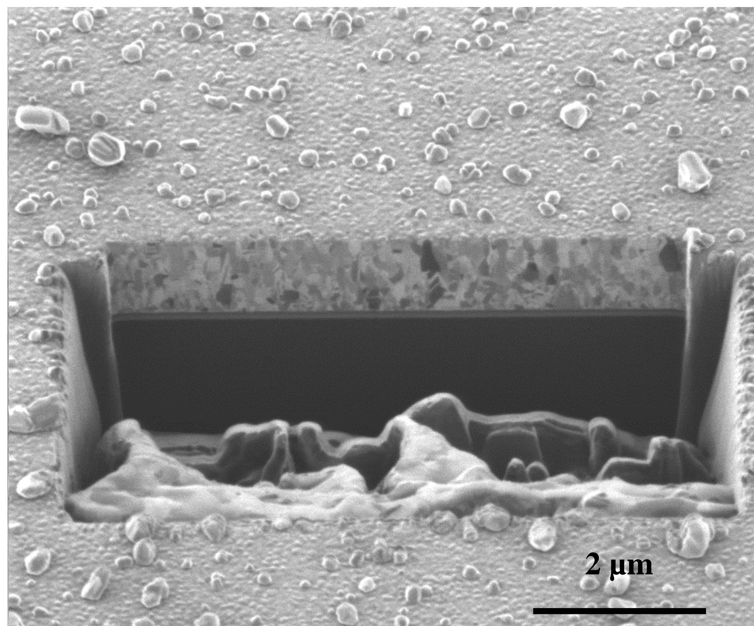

Figure 4-31 FIB micrograph of a 1 µm thick Cu-1at.%Al film [086] which was reactively sputtered at an oxygen partial pressure of 1×10^{-3} Pa. The film was thermally cycled twice to 500 °C under inert gas atmosphere in the wafer curvature apparatus. Small non-columnar grains with diameters up to 200 nm can be seen on the side wall of the sputter-etched trench. Annealing hillocks can be seen on the surface. The sample tilt is 45°.

4.4 Cu-Al films: Mechanical properties

4.4.1 UHV-annealed and oxidized films

Wafer curvature measurements

The microstructure analysis of Cu-Al alloy films in section 4.3 revealed that Al segregated to the film surface and became externally oxidized. In this section, the effect of the alumi-num-oxide surface layer on the mechanical film properties is studied.

In Figure 4-32, stress-temperature curves of an oxidized Cu-Al film are shown, which exhibited grain boundary voids. The stress-temperature curve of an annealed pure Cu film of the same thickness is shown for comparison. The alloy film supports higher stresses at high temperatures. The stress at room temperature at the end of the cooling cycle is equal for both films. Larger stresses are found in the cooling curve of the void-free film oxidized at 400 °C shown in Figure 4-33. It is noted that film stress is expected to be locally relaxed at the grain boundary voids. However, the substrate curvature is proportional to an average stress, such that the stress within grains of the voided film might be higher than indicated by the experiment.

In Figure 4-34, the stress-temperature curve of a UHV-annealed Cu-Al film is shown which was oxidized during a 5 min temperature hold at 600 °C in the wafer curvature ap-paratus. The purpose of this experiment was to study the stress evolution in a film during and after oxidation, because film stresses are expected to play an important role in void growth. In the furnace of the wafer curvature apparatus, the oxygen partial pressure could not be controlled. During the holding segment at 600 °C, stress relaxed as indicated by the arrow. Voids grown during this experiment are shown in Figure 4-23.

In Figure 4-35, the thermo-mechanical behavior of a 0.5 µm thick Cu-1at.%Al film is shown. The film had been UHV-annealed but not oxidized, such that grain boundaries were not voided. Stresses were higher in the alloy film than in the 0.5 µm thick pure Cu film which is inserted for comparison. Interestingly, the characteristic stress drop in com-pression and the kink in the cooling curve observed in the pure film have disappeared in the alloy film.

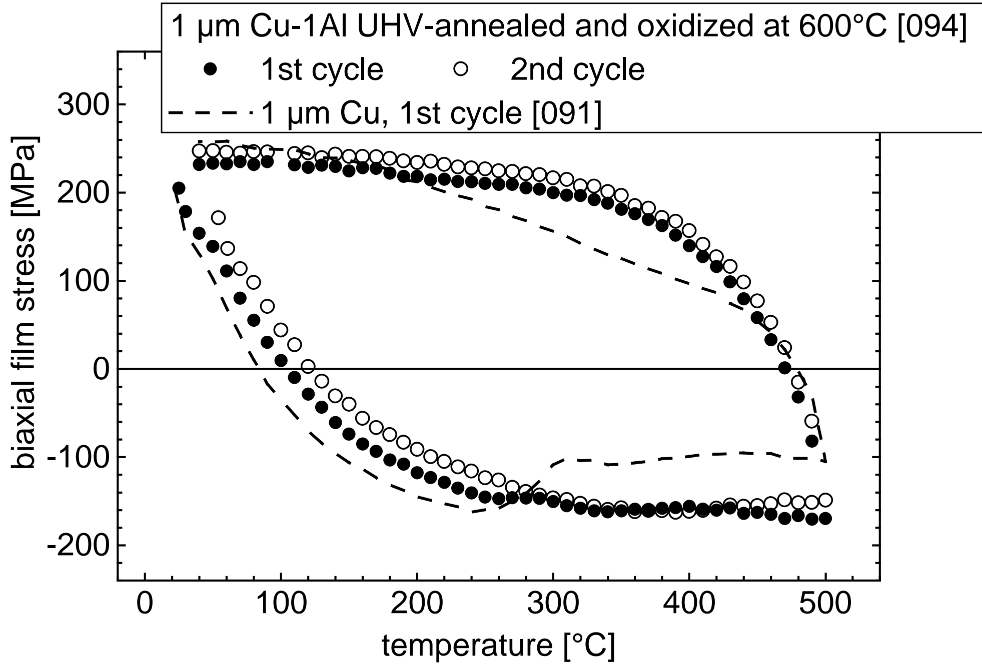

Figure 4-32 The first two wafer curvature cycles of a 1 µm thick Cu-1at.%Al film, UHV-annealed and oxidized at 600 °C (10 s, 1×10^{-3} Pa). This film was voided at the grain boundaries. The stress-temperature curve of a 1 µm thick pure Cu film is inserted.

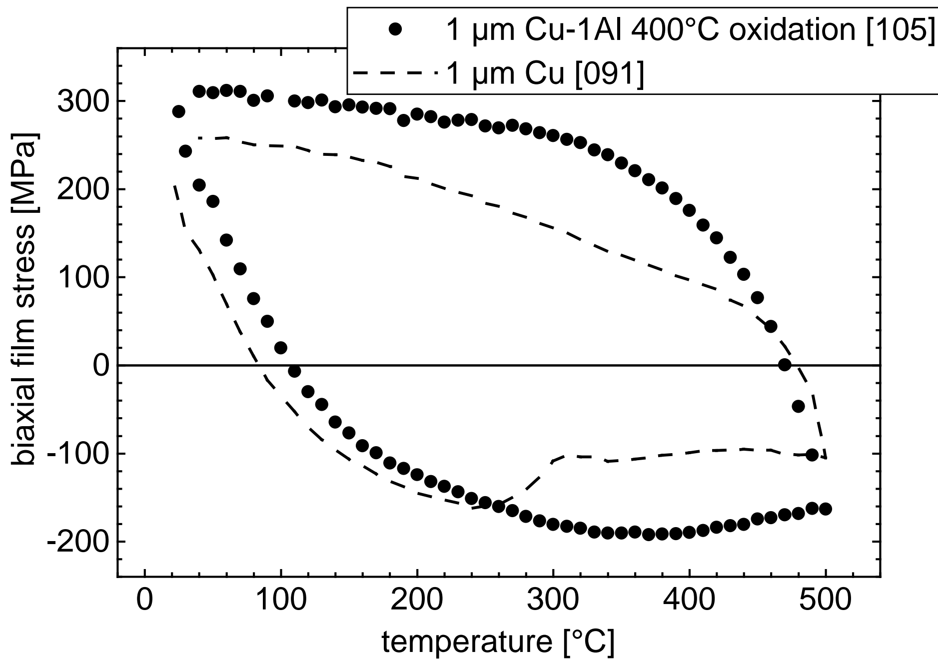

Figure 4-33 The first wafer curvature cycle of a void-free 1.0 µm thick Cu-1at.%Al film, UHV-annealed at 600 °C and oxidized at 400 °C. A FIB micrograph of the film surface is shown in Figure 4-21. The first cycle of a 1 µm thick pure Cu film is shown for comparison.

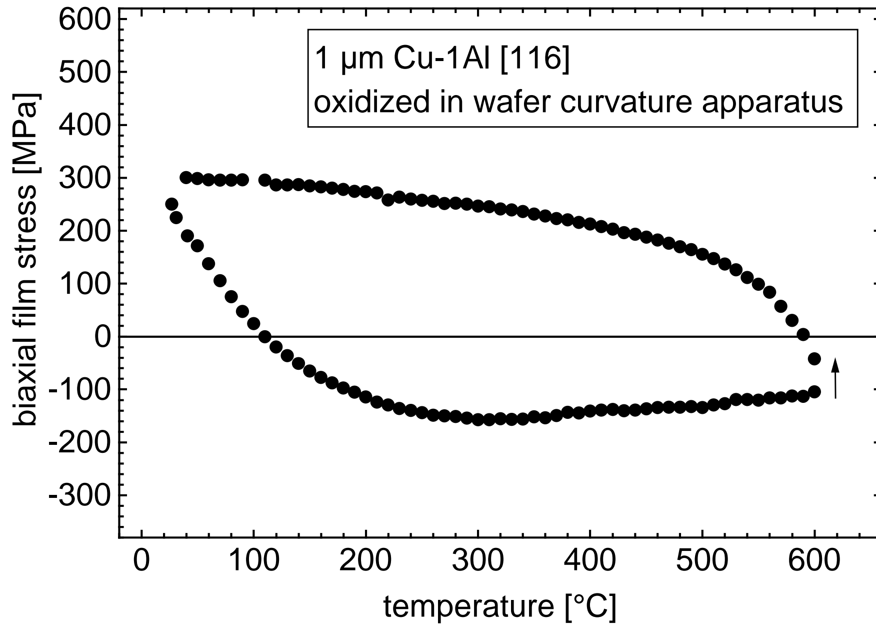

Figure 4-34 Stress-temperature curve of a UHV-annealed (10 min at 600 °C) Cu-1at.%Al film which was oxidized in the wafer curvature apparatus for 5 min at 600 °C at the end of the heating segment. The stress drop during the oxidation is indicated by the arrow. A FIB micrograph of the film surface is shown in Figure 4-23.

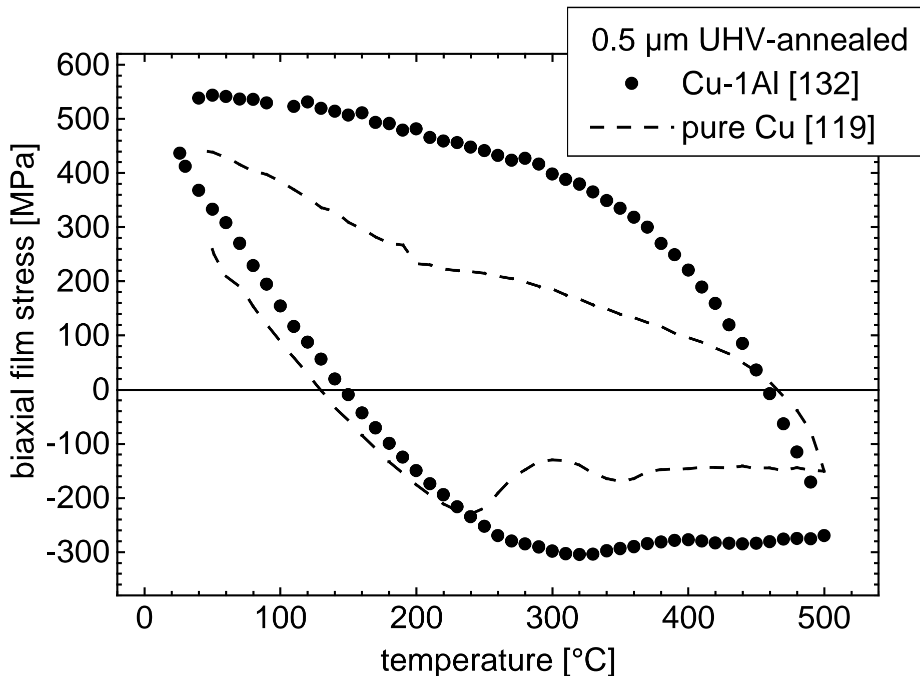

Figure 4-35 Stress-temperature curve of a 0.5 µm thick Cu-1at.%Al film. The film had been UHV-annealed for 10 min at 600 °C, but not oxidized. The corresponding curve of a 0.5 µm thick pure Cu film is shown for comparison. The stress drop in compression and the kink during cooling are only found in the pure Cu film.

Nanoindenter measurements

In Figure 4-36, the nanohardness measurements of a 1 μm thick oxidized Cu-1at.%Al film and of an annealed pure Cu film are shown. Both films have, within the error bar, the same hardness. Hardness increases with increasing indentation depth. The measurements were carried out at room temperature. The room temperature yield stress of two comparable films is equal as well (Figure 4-32). The fact that the alloy film was not hardened after oxidation is another indication for the failure of internal oxidation; a dispersion of oxide particles would have hardened the film.

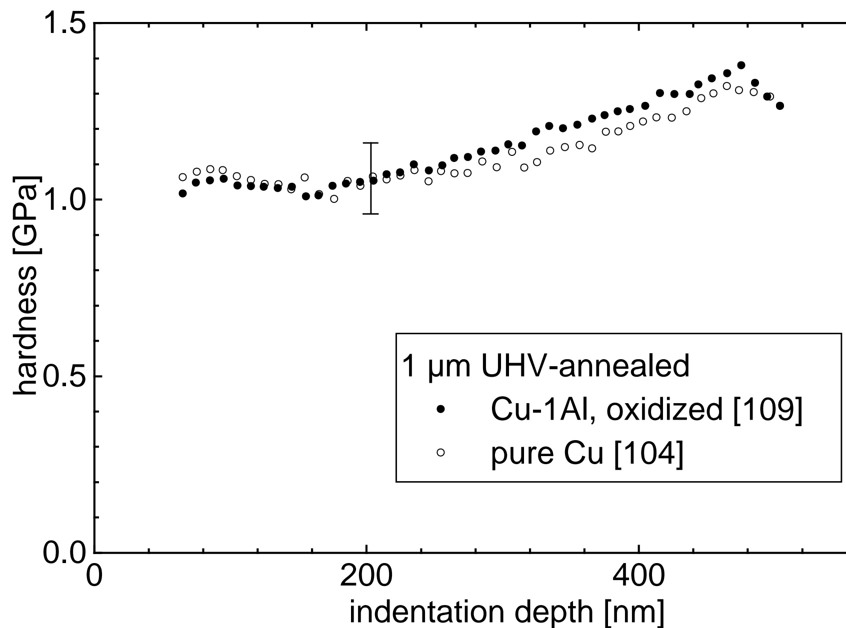

Figure 4-36 Nanohardness vs. indentation depth for 1 μm thick Cu-1at.%Al and Cu films. Both films were UHV-annealed. The alloy films was oxidized for 7 min at an oxygen pressure of 1×10^{-4} Pa at 600 °C. Grain boundaries in the alloy film were voided.

Electrical sheet resistance

The electrical sheet resistance was measured at room temperature for several Cu and Cu-Al films using a 4-point probe (Figure 4-37). The UHV-annealed pure Cu film had a specific resistivity of 1.9 μΩ cm which is only 10% higher than the resistivity of pure Cu at room temperature (1.73 μΩ cm). The sheet resistance increased linearly with increasing Al content. Resistivity decreased after annealing and further decreased after oxidation as is shown for 1% Al in the plot. Note that the oxidized alloy films were voided. The microstructure of these films were shown in Figure 4-19, Figure 4-20 and Figure 4-23.

The increased sheet resistance of the as-deposited films is explained by electron scattering at the grain boundaries. The electron mean free path in Cu single crystals is 39 nm at room temperature (see Harper et al. 1999), which is only one order of magnitude below the as-deposited grain size (Figure 4-1). During grain growth upon annealing, the grain boundary density decreases. The decrease of electrical resistance of the alloy films upon oxidation is accounted for by the segregation of Al, leading to a decreased amount of dissolved Al atoms in the Cu matrix.

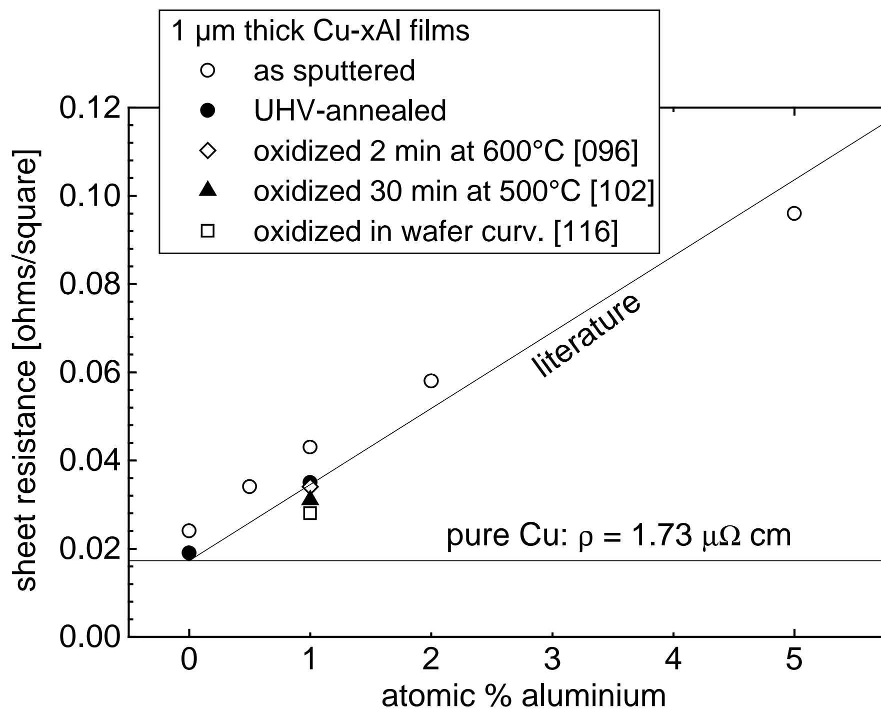

Figure 4-37 Electrical sheet resistance of 1 µm thick pure Cu and Cu-Al films measured with a 4-point probe. The film resistivity increased by a factor of 2 upon addition of 1at.% Al. Resistivity decreased upon annealing and further decreased upon oxidation. The relative error of the sheet resistance is 2%. The "literature" line refers to measurements of Ding et al. (1994).

4.4.2 HV-annealed films and reactively sputtered films

Wafer curvature measurements

Several wafer curvature measurements were carried out with as-deposited Cu-Al films. In Figure 4-38, the first two thermal cycles of a Cu-1at.%Al film are shown. The stress drop during the first heating cycle is explained by densification processes during the first an- nealing of the film. A similar observation was made for the pure Cu film in Figure 4-15, for which, however, the stress drop was smaller. In Figure 4-39 the second thermal cycles of 1 μm thick pure Cu, Cu-1at.%Al and Cu-5at.%Al films are shown. The two curves of the alloy films are similar. Stresses are higher than in the pure Cu film.

For the Cu-5at.%Al film, an isothermal stress relaxation experiment was carried out at 200 °C during cooling in the third wafer curvature cycle (Figure 4-40). The corresponding curve for the pure Cu is shown for comparison. The amount of relaxed stress is larger in the pure Cu film than in the alloy film.

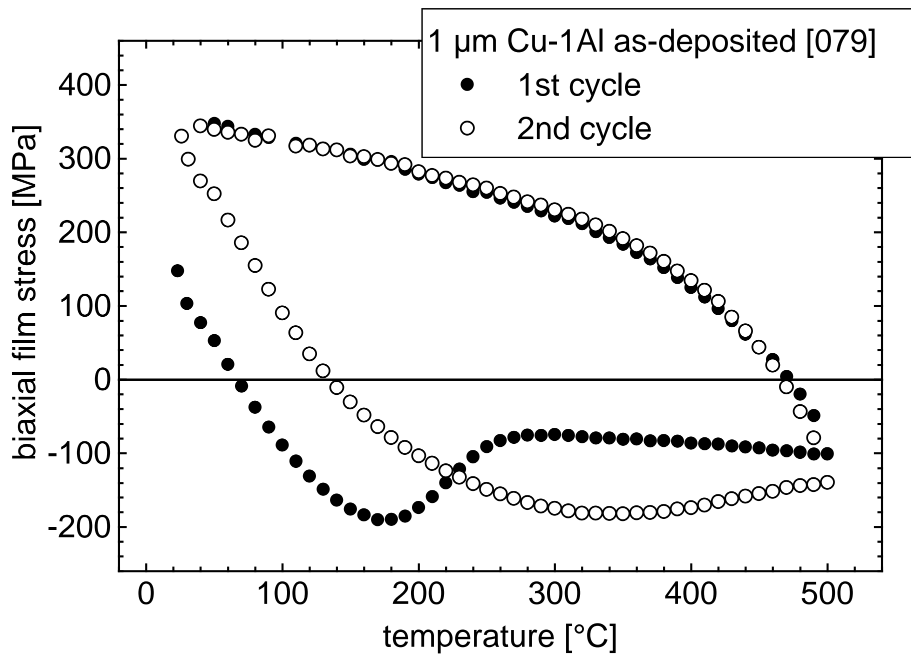

Figure 4-38 Stress-temperature curve for a 1 μm thick as-deposited Cu-1at.%Al film. The stress drop in the first heating cycle is due the stabilization of the film microstructure.

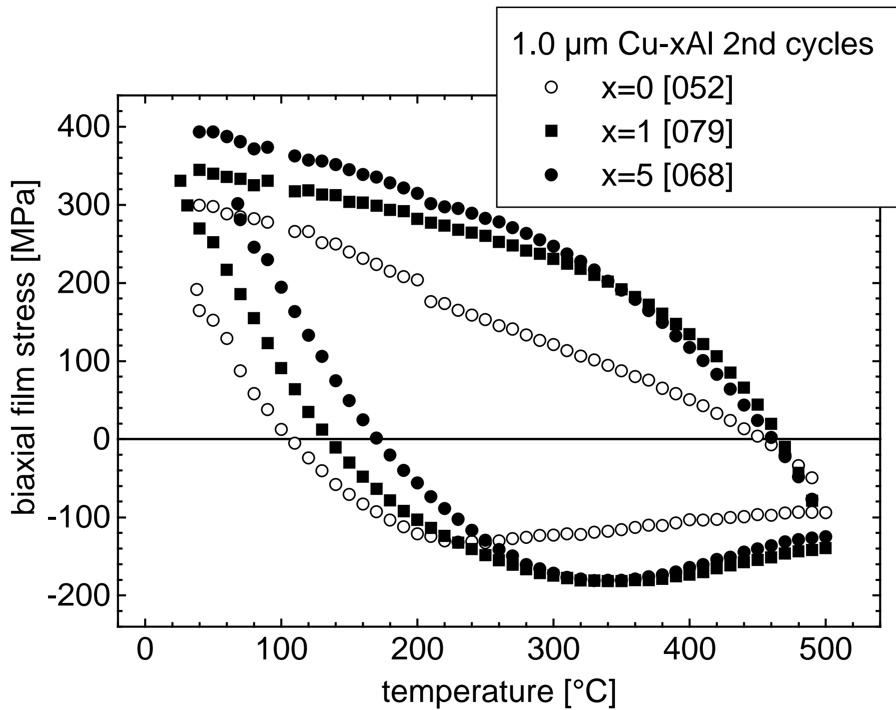

Figure 4-39 Comparison of the second thermal cycles for 1 µm thick pure Cu, Cu-1at.%Al, and Cu-5at.%Al films.

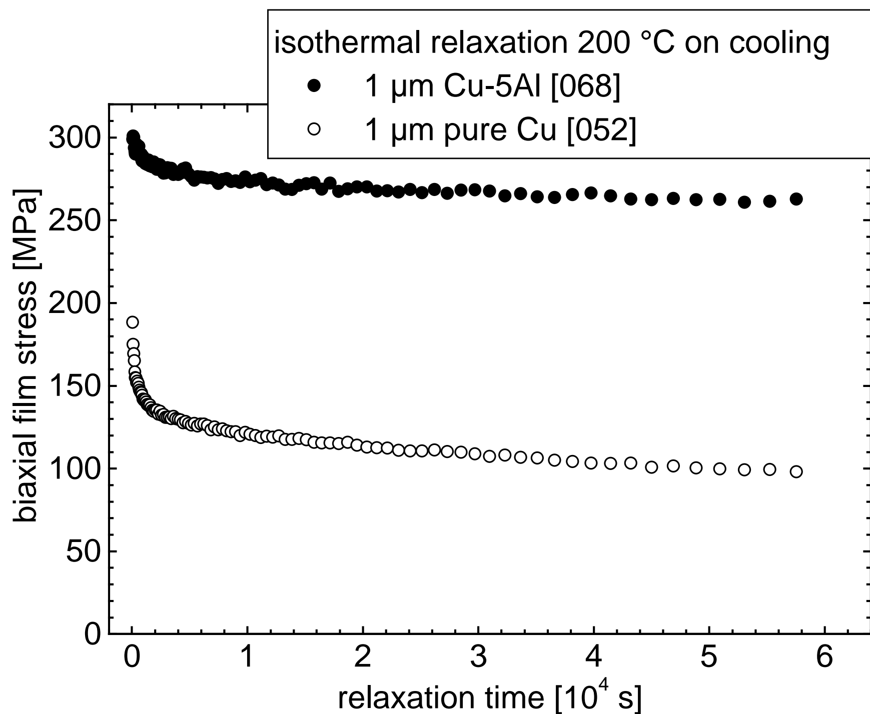

Figure 4-40 Isothermal stress relaxation experiment at 200 °C of a 1 µm thick Cu-5at.%Al film measured during the third cooling cycle. The corresponding curve for the 1 µm thick pure Cu-film is shown for comparison.

Nanoindenter measurements

The nanoindenter was used to determine the room temperature hardness of four 1 μm thick films with different Al content (Figure 4-41). A slight increase of film strength is observed with increasing Al content. The hardening, i.e. the slope of the curves is identical for all films. The difference in hardness between the pure and the 5at.%Al film is approximately 0.3 GPa, which is a 25% increase in hardness upon alloying. The room temperature yield stress measured during thermal cycling (Figure 4-39) increased from 300 MPa for a 1 μm thick pure Cu film to 400 MPa for a Cu-5at.%Al film. The relative increase in yield stress is of the same order as the increase in hardness. The microstructure of these films was not further analyzed.

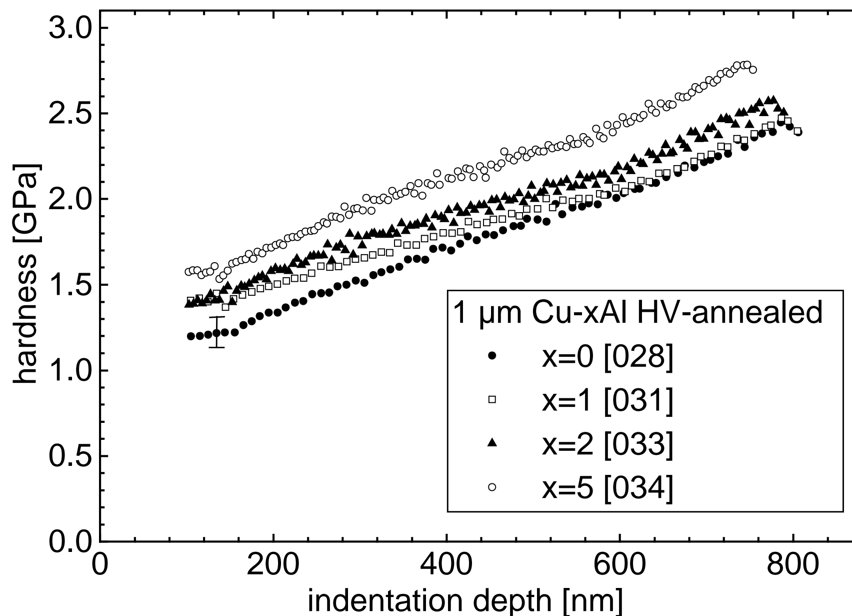

Figure 4-41 Nanohardness vs. indentation depth for 1 μm thick Cu-Al films with different Al content. The films were HV-annealed at 400 °C. Hardness increased with increasing Al content.

Wafer curvature measurements of reactively sputtered films

Wafer curvature measurements were carried out for three Cu-1at.%Al films which were reactively sputtered at different oxygen partial pressures. The stress-temperature curve of the film [081], sputtered at the lowest oxygen pressure of 1 $\times 10^{-5}$ Pa, was similar to the curve of the Cu-1at.%Al film sputtered without oxygen (see Figure 4-38). The film sputtered at an intermediate oxygen pressure of 1 $\times 10^{-3}$ Pa supported the highest stresses of all films presented in this work (Figure 4-42). The stress was compressive in the as-deposited film. The high compressive stress of –350 MPa during the first heating at 200 °C is held responsible for the growth of hillocks in this film (Figure 4-31). The film sputtered at the highest oxygen pressure, 1×10^{-2} Pa, supported only extremely small stresses (Figure 4-43). Also this film was under compressive stress in the as-deposited state. No further research was carried out with reactively sputtered films. Second phases which formed during sputtering had a large influence on grain growth such that the comparison of these films with pure Cu films was difficult.

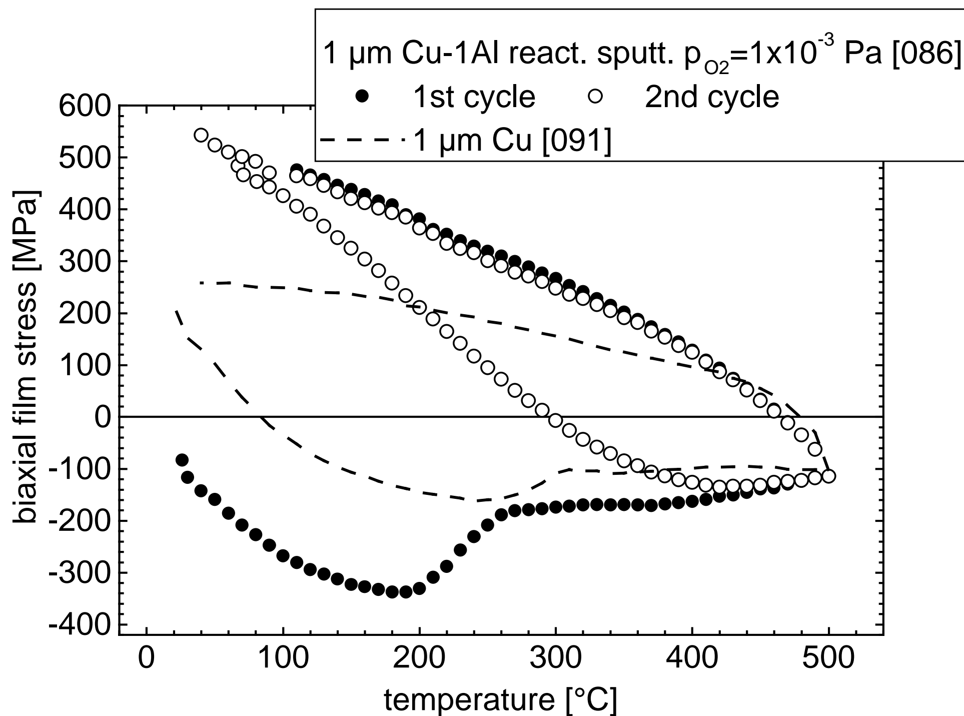

Figure 4-42 The first two thermal cycles of a 1 µm thick reactively sputtered Cu-1at.%Al film. The oxygen pressure was 1×10^{-3} Pa during sputtering. The film was cycled in the as-sputtered state. A small grain size of up to 200 nm was stabilized after thermal cycling (Figure 4-31).

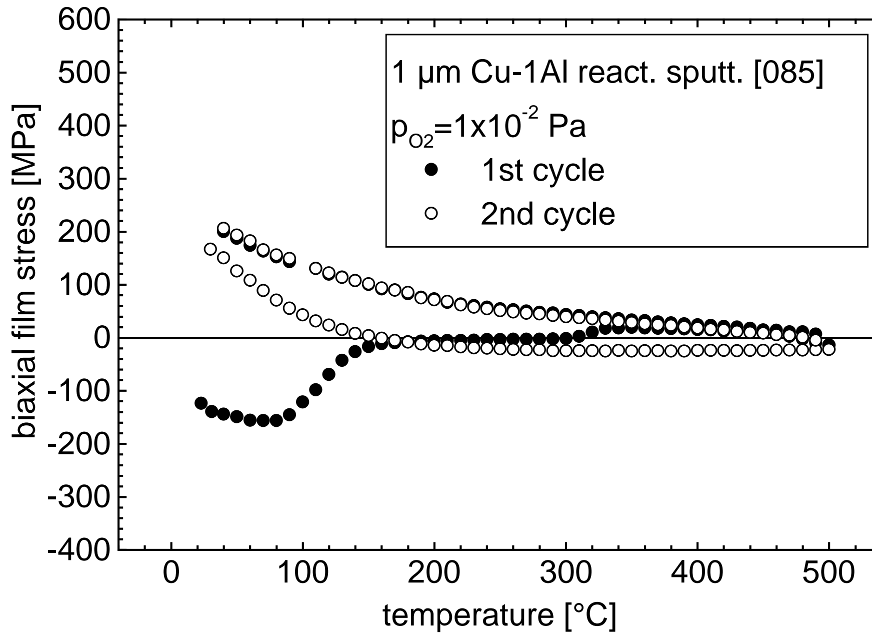

Figure 4-43 First two thermal cycles of a 1 µm thick Cu-1at.%Al film reactively sputtered at an oxygen partial pressure of 1×10^{-2} Pa. Very small and abnormally grown large grains were found in this film.

4.5 Cu-1at.%Y films: Microstructure evolution

The microstructure of Cu-1at.%Y films was investigated. Yttrium is an element with a high oxygen affinity. It is therefore suitable for internal oxidation within Cu. However, Cu and Y are practically not miscible. The films were sputtered and annealed under high-vacuum conditions.

As-deposited 1 µm thick Cu-1at.% Y films were extremely fine grained. TEM investigations with a plan view sample showed that the grains were equi-axed and had grain sizes of 20 to 50 nm. No second phase particles could be observed by TEM in the as-deposited films. Some grains were twinned with twin lamellae only 5 nm wide. Grain size stagnated at 40 to 300 nm after annealing a film to 400 °C. Deposition onto a substrate heated to 400 °C led to a similar microstructure. A several nm thick amorphous layer was formed on top of all annealed films, as could be seen in FIB pictures. A dramatic change in microstructure occurred after annealing at 580 °C for 1 h (Figure 4-44). A few grains grew to 5 µm in diameter while the remaining film stayed fine-grained. The resulting grain size dis-

tribution was bimodal with a size ratio of 100:1 for abnormally grown grains to small "matrix" grains.

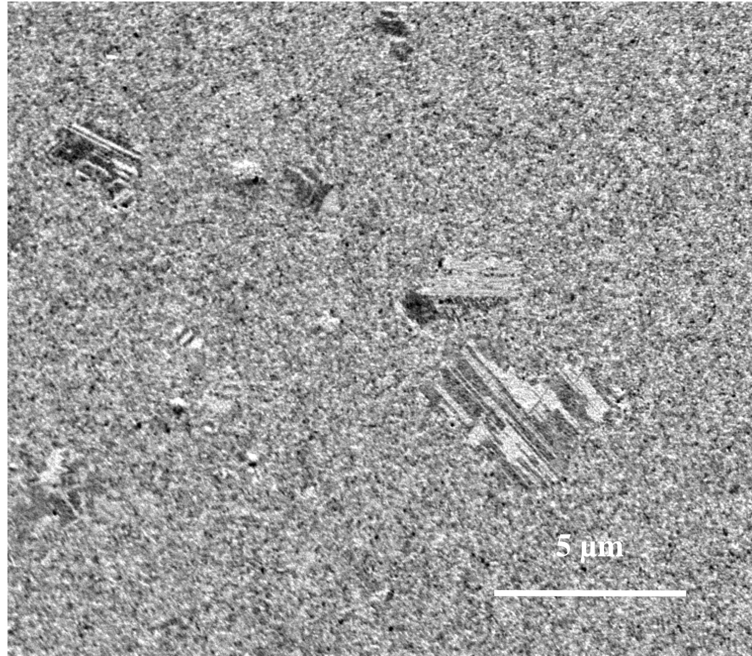

Figure 4-44 FIB micrograph of a 1 µm thick Cu-1at.%Y film, annealed 1 h at 580 °C. Abnormal grain growth is observed. Some highly twinned grains with diameters up to 5 µm have grown into the "matrix" of very small grains. The sample tilt was 30°.

Annealing of a similarly fabricated film for 30 min at a higher temperature of 600 °C led to enhanced abnormal grain growth. Approximately 50% of the film area was occupied by large grains. After annealing at 680 °C for 1 h, the small grains completely disappeared and exclusively large grains, 2 - 10 µm in diameter, were found (Figure 4-45). The large grains were heavily twinned. X-ray analysis (Θ–2Θ scan) showed (100) and (111) texture components in approximately equal fractions (the ratio of their relative intensities was equal to that of a powder sample).

The effect of film thickness was investigated. Films with different thickness were annealed for 30 min at 600 °C. 0.2 and 0.5 µm thick films exhibited a bimodal grain size distribution after annealing. The size of the abnormally grown large grains was about 1 µm in either case. A clearly distinct behavior was found for a 2 µm thick film. A monomodal grain size distribution with grain diameters from 0.5 to 2 µm suggested a normal grain growth mode in this film.

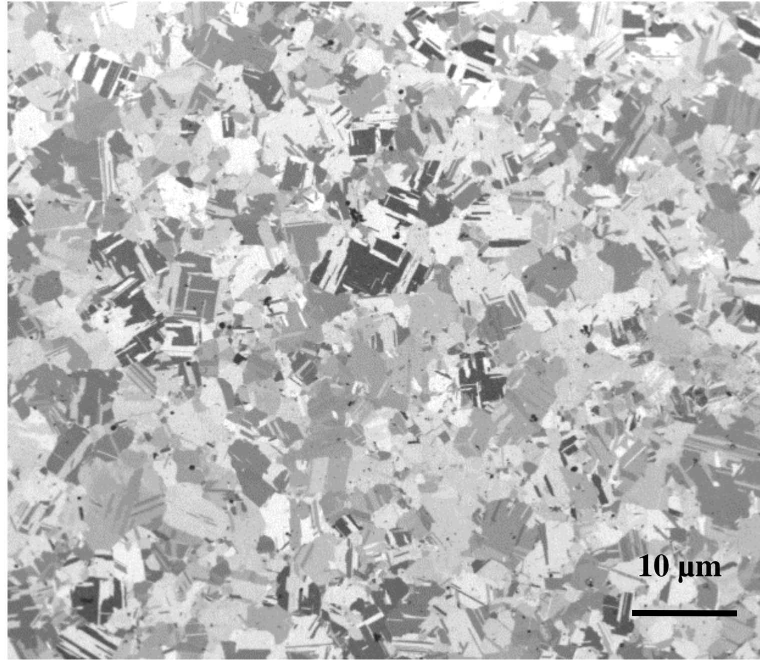

Figure 4-45 FIB micrograph of a 1 µm thick Cu-1at.%Y film, annealed for 1 h at 680 °C. Only very large grains with diameters up to 10 µm are left after annealing. The sample tilt is 0°.

Some films were removed from the substrate to be annealed under stress-free conditions. The aim of these experiments was to find out whether abnormal grain growth was provoked by thermal stress. In a free-standing film, no thermal stresses can develop. However, all films showed the same grain growth behavior as the corresponding films annealed on a substrate. A 1 µm thick free-standing film showed abnormal grain growth like the same film attached to the substrate. A 2.6 µm thick film exhibited a monomodal grain size distribution with grain diameters in the range of the film thickness suggesting normal grain growth. This microstructure was comparable to that of the 2 µm thick film annealed with substrate.

In Figure 4-46, a TEM micrograph of a 2.6 µm thick film is shown, which was annealed for 1 h at 850 °C. Small particles approximately 10 nm in diameter can be seen at twin boundaries.

The mechanical properties of the Cu-Y films were not studied systematically. As for the reactively sputtered Cu-Al films, grain growth was strongly influenced by the alloying element. Alloying effects on the mechanical properties were dominated by indirect effects such as grain boundary strengthening.

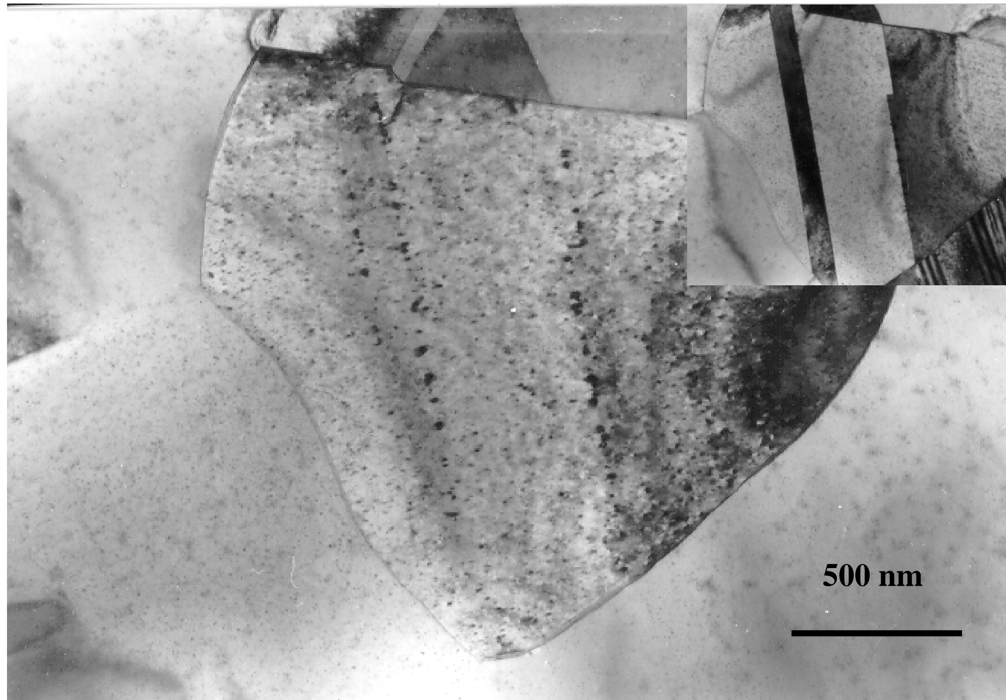

Figure 4-46 TEM bright field micrograph of a 2.6 μm thick Cu-1at.%Y film that was annealed for 1 h at 850 °C. Particles at twin boundaries can be seen. The inserted micrograph was taken with the electron beam adjusted along the <110> zone axis of the grain to bring the twin lamellae into contrast.

4.6 Summary of the results

Pure Cu and dilute Cu alloy thin films were produced by magnetron sputtering on diffusion-barrier coated single crystalline Si substrates. Microstructure evolution upon annealing and oxidation and mechanical film properties were investigated. The most important results were the following:

- Pure Cu films sputtered and annealed under UHV conditions had a large grain size of 2-3 times the film thickness. The films exhibited a strong and sharp (111) texture, and only few twin grains.
- A 1 μm thick Cu-1at.%Al film had the same grain size, texture, and twin density as a pure Cu film after annealing.

- Segregation and external oxidation of Al was observed in oxidized Cu-Al alloy films. No sign for internal oxidation of Al were found in TEM images and in nano-hardness measurements.
- Voids were found on high angle grain boundaries and on grain boundary triple junctions in Cu-Al alloy films which were oxidized at temperatures above 500 °C.
- The thermo-mechanical behavior of pure Cu films was measured with the wafer curvature method. Films sputtered on substrates cleaned in-situ by Ar ion bom-bardment supported large stresses at high temperatures.
- Stress-temperature curves of UHV-annealed 0.3 µm and 0.5 µm thick Cu films had a complex shape characterized by a stress-drop in the compressive stress region and a kink in the cooling curve.
- Yield stresses increased with decreasing film thickness. This effect was less pro-nounced at high temperature.
- Cu-Al alloy films supported higher stresses at high temperature than pure Cu films. The characteristic features found in the curves of the pure Cu films, namely the stress-drop in the heating and the kink in the cooling curve, were absent in the al-loy films.
- High-vacuum sputtered Cu-1at.%Y films showed a complex grain growth behav-ior. As-deposited films were nanocrystalline. Abnormal grain growth was observed during annealing above a threshold temperature of approximately 600 °C. Abnor-mal grain growth occurred also during annealing of free-standing films.

5 Discussion

5.1 Microstructure development in Cu, Cu-Al and Cu-Y films

Understanding of the mechanical behavior of thin films requires a good knowledge of the respective film microstructure. This section is divided into three parts: In section 5.1.1 the microstructure of UHV-sputtered pure Cu films is discussed. The results on the single-phase Cu-Al alloy system and on the two-phase Cu-Y system are discussed in the sections 5.1.2 and 5.1.3, respectively. All films in this work were polycrystalline and were sputtered onto single-crystalline Si substrates with amorphous SiO_x and SiN_x diffusion barriers.

5.1.1 Pure Cu films

In this work, magnetron sputtered Cu thin films were produced for the first time under UHV conditions. Analysis of the copper microstructure following annealing revealed several striking features. These features included a large grain size, a strong and very sharp (111)-texture, and a low twin density. Cu films known from the literature, sputtered under high-vacuum (HV) conditions, exhibited a smaller grain size, a mixed texture, and a high twin density (Gupta et al. 1992, Keller et al. 1998). In this section, a qualitative understanding of the specific UHV-film microstructure is provided.

The small grains in the as-deposited state (Figure 4-1) coarsened upon annealing. Grain growth stagnated at a grain size to film thickness ratio in the range of two to three, depending on the film thickness (see Table 5-1). Stagnation of grain growth was in agreement with the theory of Mullins (1958), which states that a moving grain boundary gets pinned by a groove on the film surface if a critical grain size of the order of two times the film thickness is reached (see section 2.1). Also, the lognormal grain size distributions observed after annealing (Figure 4-3) were in accordance with stagnation induced by grain boundary grooves (Thompson 1990).

After annealing, the grain size was twice as large as the grain size in HV-sputtered films described in literature (see Table 5-1). This is explained by the high film purity, which is attributed to the very clean fabrication conditions. Impurity elements, such as oxygen, incorporated into a growing film can hinder grain growth by segregating to the grain boundaries and thereby lowering grain boundary mobility (so-called impurity drag, Porter and Easterling 1992, p. 136). The low contamination level in the sputtering gas was obtained by a good base pressure of the vacuum system of 1×10^{-8} Pa, and by further purification of the Ar gas by a gettering system. Without purification, the total partial pressure of contamination in the 6N-quality Ar gas would have been 1×10^{-7} Pa. This pressure, which is the product of the working gas pressure of 1×10^{-1} Pa and the atomic fraction of impurity atoms in the gas, would have been one order of magnitude higher than the base pressure of the vacuum chamber.

Marieb (1994) reported similar observations for sputtered Al films. Films produced under ultra-pure fabrication conditions had larger grain sizes than films sputtered under poorer conditions.

Grain size of UHV and HV-sputtered pure Cu films

film type	film thickness [µm]	median grain size [µm]	median grain size / film thickness
UHV-sputtered films (this work)	0.5	1.4	2.8
	1.0	2.4	2.4
	2.0	3.7	1.9
HV-sputtered films (Keller 1996)	0.6	0.9	1.5
	1.0	1.2	1.2

Table 5-1 Median and normalized median grain size for unpassivated Cu films from this work and from the work of Keller (1996). All films were annealed at 600 °C.

The (111)-texture found in the Cu films is explained by surface and interfacial energy minimization. In the fcc structure, the close packed (111)-plane has the lowest surface and interfacial free energy. The change in film energy density, $\Delta F_{s/i}$, associated with grain-growth-induced texture evolution can be written as (Thompson and Carel 1996)

$$\Delta F_{s/i} = \frac{\Delta\gamma_s + \Delta\gamma_i}{t_f}, \qquad (5\text{-}1)$$

where $\Delta\gamma_s$ and $\Delta\gamma_i$ are the differences in average surface and interfacial energies before and after grain growth, respectively, and t_f is film thickness. Thus, the influence of surface and interfacial energies on the energetics of grain growth is increased with decreasing film thickness. Equation (5-1) also qualitatively explains the observed increase in the ratio of d/t_f in Table 5-1 with decreasing film thickness.

The sharpness of the texture and the low twin density in the UHV-processed Cu films are attributed to the purity of the substrate surface, which was cleaned in-situ by Ar ion bombardment before film deposition. The significance of the interface was revealed by investigating the microstructure of a film which was sputtered without substrate cleaning. The (111)-rocking curve of this film was more than 5 times broader than that of a corresponding film prepared with substrate cleaning (Figure 4-5); the twin density in this film was increased by a factor of two (Table 4-2). Substrate cleaning can affect texture formation and twinning in the following way: The minimum in interfacial energy of the (111)-orientation in fcc materials is due to the minimal number of "dangling bonds" in this close packed plane. If reactive species such as water or hydro-carbons are adsorbed on the substrate surface, these dangling bonds are partially saturated. Thus, the interfacial energy is lowered. This can explain the broader texture of the film grown on a surface which was not cleaned by ion-bombardment. It can also explain the increased twin density in this film: a twin lamella within a (111)-grain is (511)-oriented and thus energetically less favorable. However, this effect would be limited by the energy cost of surface free energy which is not lowered by the impurities at the interface. Note that this explanation so far is only hypothetical. In order to verify this argument, direct information about the state of bonding at the interface is required. For future work, high resolution TEM measurements of the film/substrate interface of films sputtered with and without substrate cleaning in side view are proposed.

The interfacial energy may also be responsible for the increase in the ratio of the twin surface area to film area, which was proportional to film thickness (Table 4-2). As shown by equation (5-1), the effect of interfacial energy for the average film energy density scales with the inverse of film thickness. Thus, the relative cost of interfacial energy associated

with twinning is reduced in the thicker films. However, as long as the driving forces for twinning in the Cu films is not understood, this argument remains speculative.

5.1.2 Cu-Al films

Two aims stimulated this study on the microstructure of the Cu-Al films. The first idea was to create a fine dispersion of aluminum-oxide particles within the Cu matrix by internal oxidation of a film consisting of a dilute Cu-Al alloy. This was not achieved; Al segregated at the film surface and was oxidized there. The second aim was to control the microstructure such that grain size and texture in the alloy were the same as in pure Cu films. This goal was reached. After oxidation at temperatures above 500 °C, grain boundary voids were observed in the alloy films. This effect is discussed in section 5.4.

Grain size, texture, and twin grains

With the aim of not affecting grain growth due to alloying, Cu-Al films were annealed *before* a second phase could be formed by oxidation. Thus, film fabrication followed a three-step procedure: Dilute Cu-Al alloy films were sputtered under UHV-conditions. The films were annealed immediately after film deposition in UHV at 600 °C without breaking the vacuum. During grain growth, the Al was in solution (Figure 5-1). The films were oxidized only after the grain structure had been stabilized. For films containing 1 at.% Al, no alloying effects on grain size (Figure 4-25), texture (Figure 4-26 and Figure 4-27), and twinning (Table 4-4) were observed. Thus, solute drag due to dissolved Al atoms was negligible.

The effect of oxidation

After a stable grain size had been achieved by post-deposition annealing, the films were oxidized at high temperatures in order to produce aluminum-oxide particles by internal oxidation. However, internal oxidation was not achieved. The characteristic contrast of small objects observed in TEM (Figure 4-24) could also be observed in pure Cu-films. This contrast is interpreted as coherency strain caused by radiation damage during ion-beam thinning of the TEM samples. A second indication for the absence of internal oxidation was that the nanohardness of an oxidized Cu-Al alloy film was not increased when compared with the hardness of pure Cu films (Figure 4-36). However, it is noted that both indications do not exclude that a “molecular” dispersion of very small particles may have been formed which was neither visible in TEM, nor could strengthen the alloy films.

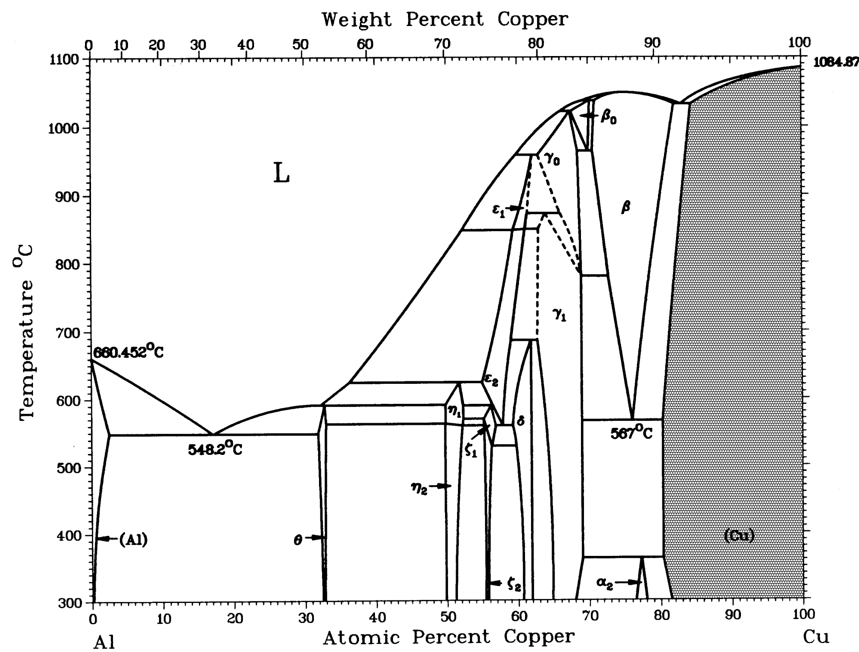

Figure 5-1 The binary phase diagram of Cu and Al shows a large region of solubility of Al on the Cu-rich side. Both Cu and Al possess fcc crystal structure with a lattice mismatch of only 10% (a_{Al} = 4.0 Å, a_{Cu} = 3.6 Å) (from Massalski 1990, p. 142).

Failure of Al internal oxidation is interpreted as a consequence of the self-passivation of the alloy films upon oxidation. It was shown by Auger-depth profiling that part of the Al segregated and oxidized at the film surface (Figure 4-29). The thickness of the aluminum-oxide scale on this 1 µm thick Cu-1at.%Al film was approximately t_o = 1 nm after 10 s oxidation time. After thermal cycling of this film in the wafer curvature apparatus, the thickness increased to t_o = 5 nm. This corresponds to a segregation of 5% or 25% of the total Al content at the surface, estimated from the theoretical density of α-Al_2O_3, ρ = 3.97 g/cm^3 (Morrell 1985, p. 70). The remaining Al atoms were assumed to remain dissolved in solid solution. The segregation of the Al atoms was in accordance with the decrease of the sheet resistance after oxidation (Figure 4-37). Al segregation to the film/substrate interface cannot be excluded, but this was not investigated in this work.

Segregation and external oxidation of Al was also observed in Cu-Al alloy films by Ding et al. (1994). The authors found a thin aluminum-oxide scale on the film surface after annealing in an inert gas atmosphere. The corrosion of Cu films was shown to be drastically reduced by the alloying.

The external oxidation and absence of internal oxidation is explained by the short diffusion paths in a thin film. In bulk alloys, so-called particle free zones are often observed along grain boundaries. The width of these zones is typically in the range of one micrometer (see e.g. Porter and Easterling 1992, p. 304). This is just of the order of the film thickness investigated in this work. One explanation for the formation of a particle free zone is heterogeneous nucleation of the second phase at the grain boundary. The width of the zone would thus be of the same order as the diffusion length, $\bar{x}$, of the second phase element during annealing. The diffusion length can be estimated by the equation, generally applicable to diffusion problems,

$$\bar{x} \approx 2\sqrt{Dt}\ , \tag{5-2}$$

where D is the diffusivity of the solute in the matrix, and t is time. Inserting typical values from an oxidation experiment from this work, a diffusion length of 200 nm is estimated. This is indeed in the range of the film thickness of 1000 nm. For this estimate, an oxidation time t = 100 s, and the diffusivity of Al in Cu (Neumann 1990),

$$D = 8 \cdot 10^{-6} \exp\left(-\frac{181.3 \text{ kJ mol}^{-1}}{RT} \right) \text{m}^2 \text{ s}^{-1},$$

at a temperature of T = 600 °C were used.

A related phenomenon was observed by Kirchner et al. (1997) for thin dilute Al-Si-Ge alloy films. In the thin films, precipitation occurred preferentially at grain boundaries and at the interface between film and substrate, which acted as heterogeneous nucleation sites. This was in contrast to bulk alloys of identical composition where second phase particles were formed within the grains, which were larger than in the films.

Reactively sputtered films

In this work, several Cu-Al films were reactively sputtered with oxygen (section 4.3.2). A maximum grain size of only d = 200 nm was found after thermal cycling of a 1 µm thick film sputtered at an oxygen partial pressure of $p = 1 \times 10^{-3}$ Pa (Figure 4-31). Stagnation of grain growth is interpreted by grain boundary pinning at second phase particles formed during sputtering. Assuming that all Al atoms were oxidized during sputtering, an alumi-

num-oxide particle radius of r_p = 3 nm can be estimated from the Zener pinning model. This was calculated upon insertion of d = 200 nm and f = 0.019 into equation (2-19). The volume fraction, f, of the aluminum oxide was calculated from the theoretical density of α-Al_2O_3, ρ = 3.97 g/cm^3 (Morrell 1985, p. 70). It is noted that the formation of also CuO_x during sputtering cannot be excluded.

The small grain size had a large influence on the yield stress of this film which was σ_y = 550 MPa at 40 °C at the end of a wa fer curvature experiment (Figure 4-42). This was about twice the yield stress found for pure Cu films of the same thickness (see e.g. Figure 4-15. The grain-boundary contribution to the yield stress is obtained assuming that the Hall-Petch relation, equation (2-10), holds:

$$\Delta\sigma_{gb} = \frac{1.12\times10^5 \text{ Nm}^{-3/2}}{\sqrt{200\times10^{-9} \text{ m}}} = 250 \text{ MPa},$$

where the Hall-Petch constant for bulk Cu, k_y = 1.12×10^5 Nm$^{-3/2}$ (Courtney 1990, p. 171), was used. This value matches well with the difference in yield stresses between the pure and the alloy film.

These experiments, which were not continued in this work, showed the importance of annealing films in which no second phase was present to impede grain growth.

5.1.3 Cu-Y films

Y is also an element with high oxygen affinity and can be used as a component for internal oxidation in Cu. However, in contrast to Al, Y has a very low solubility in Cu which is below 0.04 at.% at 860 °C. This can be seen in the binary Cu-Y phase diagram in Figure 5-2. Grain growth of sputtered Cu-1at.%Y films was investigated in this work. The films were sputtered from an alloy target under HV-conditions. As-deposited films were nano-crystalline. Substantial grain growth was inhibited below a threshold temperature of approximately T_{th} = 580 °C. Above this value, abnormal grain growth was observed (section 4.5).

As in the case of the reactively sputtered Cu-Al films discussed above, grain growth was inhibited in these films probably by grain boundary pinning by a second phase. This second phase consisted either of the intermetallic phase Cu_6Y (see Figure 5-2), or of yttria

(Y_2O_3) formed by reaction of Y with the oxygen in the HV-sputtering chamber during film deposition.

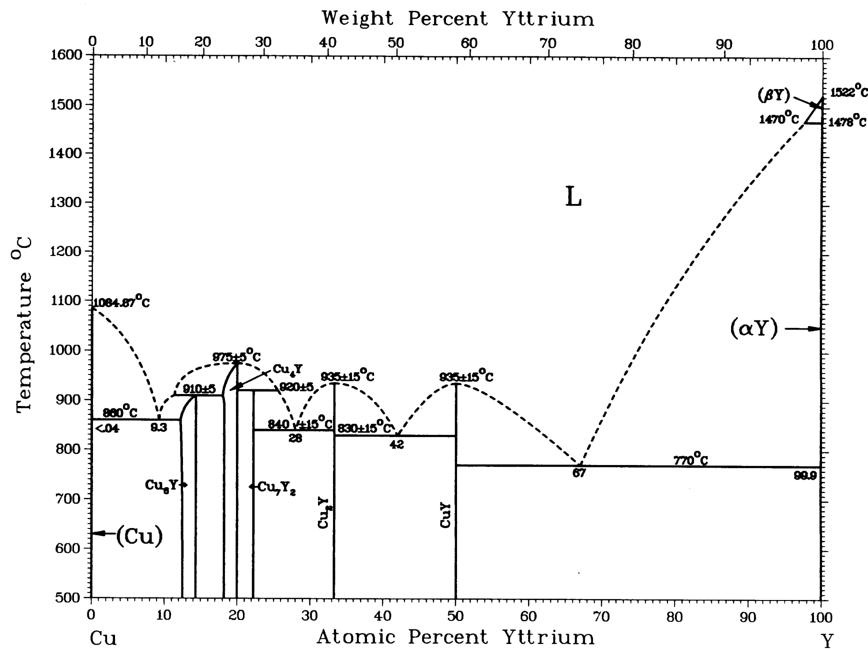

Figure 5-2 The binary phase diagram of the Cu-Y system shows no miscibilty on the Cu-rich side of the diagram (from Massalski 1990, p. 1506).

It was discussed in section 2.1 that two conditions must be fulfilled for abnormal grain growth to occur. These conditions were stagnation of normal grain growth, and an adva n-tage in energy of the abnormally growing grain. Driving forces for abnormal grain growth in thin metal films on Si are surface energy minimization and strain energy minimization (Thompson and Carel 1996). In fcc metal films, these driving forces favor growth of either (111)-oriented or (100)-oriented grains, respectively. No preferential grain orientation was observed in the annealed Cu-Y films. Thus, the triggering mechanism for abnormal grain growth could not be specified from the texture. Strain energy minimization was, however, excluded, because abnormal grain growth was observed also in the free-standing films, which were supposed to be stress-free during annealing.

Note that films with thickness larger than 2 μm did not exhibit abnormal grain growth during annealing. The grain size of these films in the as-deposited state was larger than the grain size of the thinner films, which underwent less substrate heating during sputtering.

This result underlines the importance of the role of the total stored grain boundary energy for abnormal grain growth.

In this work, no systematic study of the mechanical properties of Cu-Y films was carried out for two reasons. First, the post-annealing microstructure was very different from the microstructure of pure Cu films. Particle effects would have been masked by other effects due to microstructure, e.g. by grain boundary strengthening. The second reason was the high annealing temperatures required to obtain substantial grain growth. Annealing temperatures above 600 °C were not acceptable, because film-substrate interdiffusion was reported for Cu films on silicon-nitride in this temperature range.

5.2 Thermo-mechanical behavior of Cu and Cu-Al alloy films

The two most intriguing characteristics of the mechanical behavior of thin metal film are, first, the high stresses supported by these films and, second, the complexity of the stress-temperature curves measured in thermal cycling experiments. In this section, the different shapes of stress-temperature curves of Cu and Cu-Al alloy films are discussed. The yield stress of Cu films as a function of film thickness will be discussed in section 5.3.

In the literature overview in section 2.2.3, the thermo-mechanical behavior of Cu films on Si substrates was classified as Cu-type and Al-type behavior. Unpassivated films exhibited Cu-type stress-temperature curves. Very low stresses were found in these films at high temperatures. The mechanical behavior of Cu films passivated with a capping layer was similar to that of Al films, which is why this behavior was labeled Al-type. High stresses at high temperatures were characteristic of this film type.

This research revealed a third, new type of behavior for unpassivated Cu films, processed under UHV-conditions with pre-deposition substrate cleaning by ion bombardment. These films supported significantly higher stresses at high temperatures than the Cu films currently reported in the literature. In Figure 5-3, this new UHV Cu-type curve is shown in comparison with a representative example of an HV Cu-type curve from the literature. Both films were unpassivated and 1 µm thick.

Al surface segregation and oxidation was observed in this work for Cu-Al alloy films. This led to a self-passivation of the alloy films (section 5.1.2). The self-passivation produced a similar effect on the thermo-mechanical behavior as an artificial passivation layer: Al-type curves with high stresses at high temperatures were found for these films. An example is shown in Figure 5-3, in which the stress-temperature curve of a 1 µm thick self-passivating Cu-1at.%Al film can be compared to the two different Cu-type curves.

Each of the 3 curve types in Figure 5-3 will now be discussed. The Al-type curve shape of self-passivating Cu-1at.%Al films is discussed in section 5.2.1. This curve shape will be shown to be consistent with dislocation glide mechanisms. In section 5.2.2, a new model for constrained diffusional creep in polycrystalline thin films, recently published, is used as a basis for the interpretation of the shape of curves of pure Cu films. Results of this model are applied to simulate the shape of a UHV Cu-type curve. This is the first successful modeling of the thermo-mechanical behavior of a Cu film using a constitutive law for

diffusional creep in a thin film under the constraint of a stiff substrate. The HV Cu-type curve for high-vacuum processed films known from the literature is subject to discussion in section 5.2.3. Understanding of this type is incomplete. However, some experimental evidence for the importance of the film-substrate interface will be discussed.

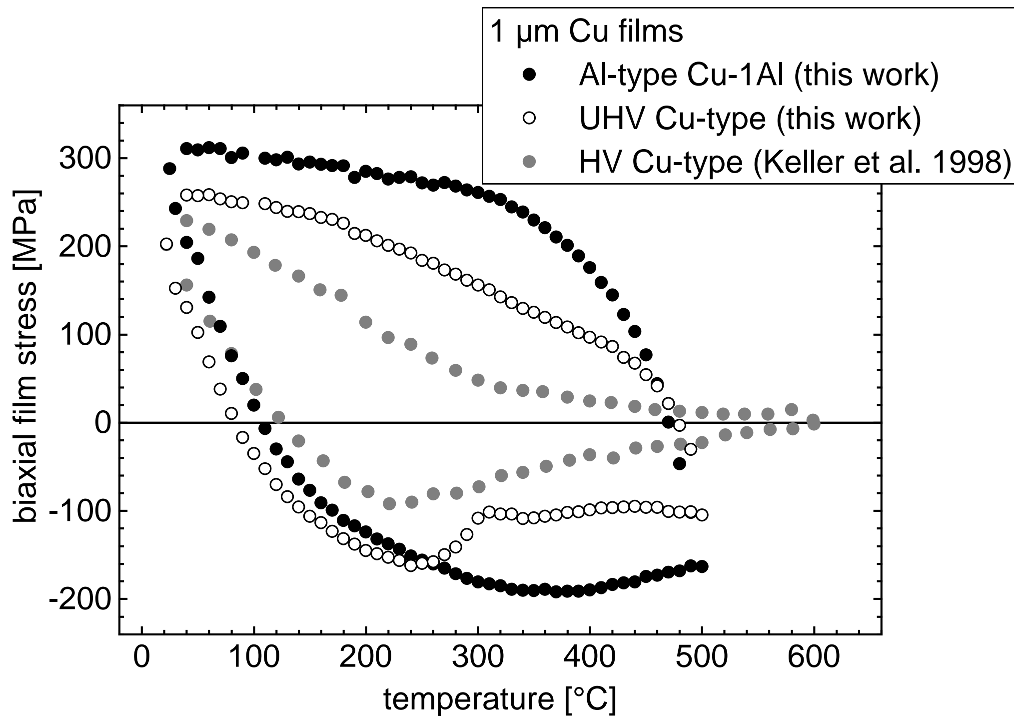

Figure 5-3 Overview over the three different types of thermo-mechanical behavior of 1 µm thick Cu films discussed in this section. The Al-type curve belongs to a self-passivating Cu-1at.%Al film [105] which was oxidized at 400 °C; grain boundaries in this film were not voided. The UHV Cu-type curve belongs to the pure Cu film [091].

5.2.1 Stress relaxation by dislocation glide (Al-type)

Self-passivating Cu-1at.%Al and Al films

In Figure 5-4, stress-temperature curves of a self-passivating Cu-1at.%Al film and of an Al film from the literature are shown for comparison. The stresses have been normalized by the shear moduli of Cu and Al in order to consider the different stiffness of each material. Both films exhibit a very similar thermo-mechanical behavior. This characteristic shape of the stress-temperature curve was labeled Al-type (section 2.2.3). Both films are characte r-ized by an aluminum-oxide surface layer. It was claimed by Thouless et al. (1996) that di f-

fusional relaxation mechanisms were suppressed in passivated noble metal thin films as well as in Al films, which de-facto are passivated due to the dense and thermally stable native oxide.

The similar shape of the curves in Figure 5-4 evidently demonstrates that the deformation mechanisms involved are not creep mechanisms. Creep mechanisms, such as power-law creep or diffusional creep, are based on atomic diffusion, for which the activation energy scales with the melting temperature of the specific material. The melting temperature of Cu (1357 K) is almost 1.5 times the melting temperature of Al (933 K); if both stress-temperature curves could have been described by a mechanism involving atomic diffusion, similarity of the curve shapes would have only been expected if stresses were plotted versus the homologous temperatures, and not versus the un-normalized temperature as in Figure 5-4.

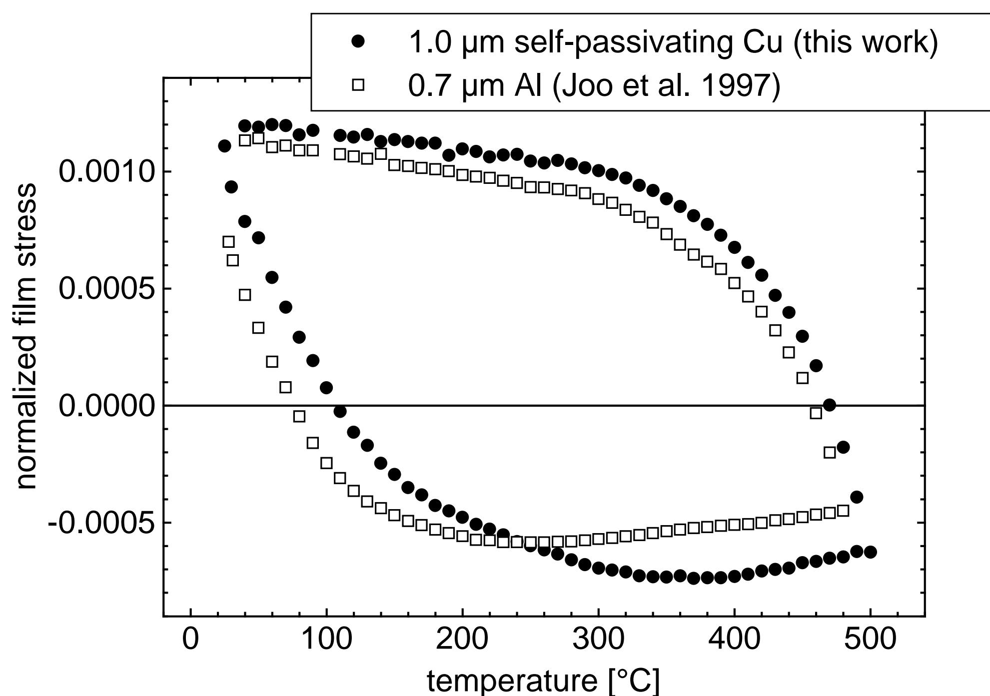

Figure 5-4 Al-type stress-temperature curves for the self-passivating Cu-1at.%Al film [105] from this work and for an Al film from the literature. The stresses are normalized by the respective shear moduli at 300 K (μ_{Cu} = 42.1 GPa, μ_{Al} = 25.4 GPa, Frost and Ashby 1982, p. 21).

Flinn et al. (1987) first proposed that the thermo-mechanical behavior of Al thin films could be described by dislocation glide mechanisms (see section 2.2.3). The constitutive

equation (2-11) for thermally activated glide describes plastic yielding by dislocation glide in the presence of obstacles. The activation energy for obstacle controlled glide for medium strength obstacles in Cu and Al is given by Frost and Ashby (1982, p. 21) as

$$\Delta F = 0.5 \mu b^3 ,$$

where μ is the shear modulus, and b is the Burgers vector of the matrix material. The values for Cu and Al are listed in Table 5-2. The ratio of activation energies for glide in Cu and Al is 1.17, which is closer to unity than the ratio of the activation energies for diffusion, 1.5. This indicates further evidence for the statement made that the curve shape shown in Figure 5-4 was in accordance with dislocation glide.

Activation energies for obstacle controlled dislocation glide

	μ [GPa]	b [Å]	$\Delta F = 0.5\ \mu\, b^3$ [J]
Cu	42.1	2.56	3.5×10^{-19}
Al	25.4	2.86	3.0×10^{-19}

Table 5-2 Shear moduli at 300 K, μ, Burgers vectors, b, and activation energies for obstacle controlled glide, ΔF, after Frost and Ashby (1982) p. 21.

Modeling a stress-temperature curve

The constitutive equation for thermally activated dislocation glide, equation (2-11), was applied to simulate the stress-temperature curve of a 0.5 μm thick self-passivating Cu-1at.%Al film. The agreement of the simulated curve with the experimental data shown in Figure 5-5 is good. Material parameters for bulk Cu were used for the simulation. The model curve was calculated with Mathematica4.0 software (www.wolfram.com) applying the Runge-Kutta routine for the numerical integration of the differential equation,

$$\frac{d\sigma}{dT} + M_f \Delta\alpha + \frac{M_f}{\dot{T}} \dot{\varepsilon}_0 \exp\left[-\frac{\Delta F}{k_B T} \left(1 - \frac{s\sigma}{\hat{\tau}} \right) \right] = 0 , \qquad (5\text{-}3)$$

which is obtained in a straightforward manner by taking the derivative of the film strain balance, equation (2-3), with respect to temperature, under consideration of equations (2-2)

and (2-4), and replacing $\dot{\varepsilon}_{plastic}$ by the constitutive law, equation (2-11). The difference in thermal expansion coefficients is written as $\Delta\alpha = \alpha_{Cu} - \alpha_{Si}$, and $\dot{T}$ is the experimental heating rate. The code for the computer simulation is found in the Appendix B.

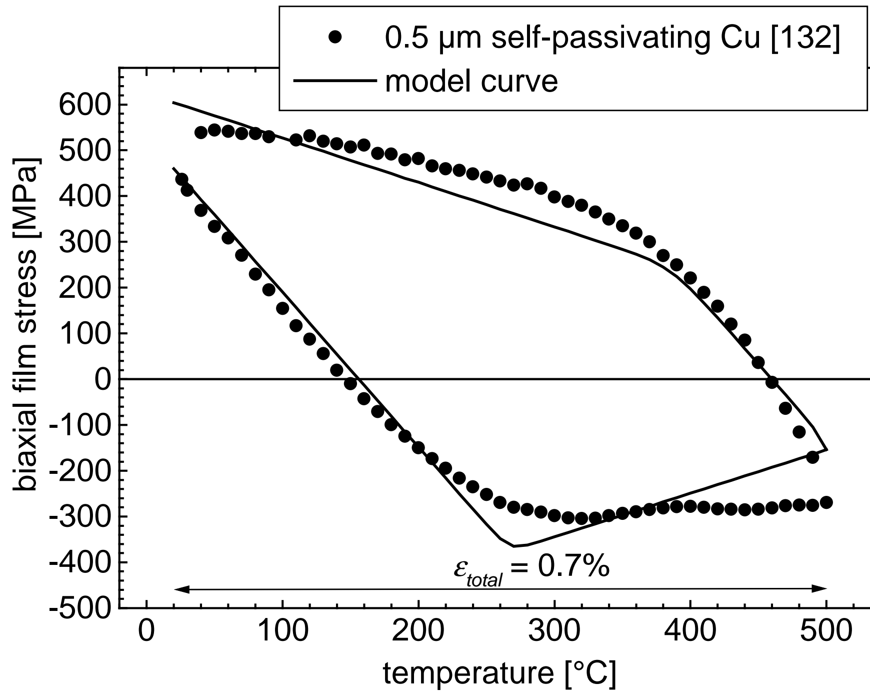

Figure 5-5 Theoretical stress-temperature curve for thermally activated dislocation glide and experimental curve of a self-passivating Cu-1at.%Al film. The model curve is based on equation (2-11) using the parameters for bulk Cu $\dot{\varepsilon}_0 = 1\times10^6$ s^{-1} and $\Delta F = 3.5\times10^{-19}$ J from Frost and Ashby (1982) p. 21, and $\hat{\tau} = 240$ MPa. The parameters $\Delta\alpha = 1.4\times10^{-5}$ K^{-1} and $M_f = 2.6\times10^{11}$ Pa (Appendix A) for 300 K were used for the complete cycle; the experimental heating rate, $\dot{T} = 0.1$ Ks^{-1}, was used. The starting value for the stress at time $t = 0$ was taken from the experiment. The Schmid factor $s = 0.27$ for (111)-orientation was used. The total thermal strain in one cycle is 0.7% (see Appendix A).

The simulation describes well the apparent asymmetry between the flow stress in compression and in tension. In fact, the non-elastic segments of the simulated curve are symmetrical relatively to zero stress; the lower yield stress during heating is due to the temperature dependency of yield stress, which decreases with increasing temperature. The simulation also describes well the increase in flow stress upon cooling. Other authors interpreted this increase as work hardening (Venkatraman and Bravman 1992, Nix 1998).

Work hardening was not included in this simulation as the parameter for the critical-stress, $\hat{\tau}$, was kept constant during the whole cycle.

Two features, however, are not well described by the simulation. The first is the decreasing slope found in the experimental curve upon cooling. The second is the stress plateau in compression between 300 and 500 °C. Both are attributed to the use of only one constant value for the parameter $\hat{\tau}$ for the whole cycle. Although the yield stress of the films is discussed in section 5.3, it is noted at this point that the value $\hat{\tau} = 240$ MPa is very high in comparison to bulk Cu. It is also noted that this value cannot be explained in the frame of the current models. It is almost one order of magnitude higher than the yield stress in shear $\hat{\tau}_{Nix} = 33$ MPa, calculated with the Nix model, equation (2-8a), using the Schmid-factor for (111)-orientation $s = 0.27$. (For the calculation, an oxide thickness of 5 nm was estimated based upon the Auger depth profile for a similar film (Figure 4-29 b). The values for Cu from Table 5-2 were used, as well as the shear moduli $\mu_{Si} = 63.7$ GPa (Frost and Ashby 1982, p. 72), $\mu_{Al2O3} = 155$ GPa for α-alumina (Frost and Ashby 1982, p. 99), and $\nu = 0.33$. The constants β were set to unity (Venkatraman and Bravman 1992), and the angle $\varphi = 70.5°$ was used.)

In section 5.3.3, a new explanation for the thin-film effect on yield stress will be presented, which claims that plastic deformation in a thin film is dislocation source controlled rather than obstacle controlled.

5.2.2 Stress relaxation by constrained diffusional creep (UHV Cu-type)

In Figure 5-6, the stress-temperature curves of an unpassivated Cu film (UHV Cu-type) and of a self-passivating Cu-1at.%Al film (Al-type), both 0.5 μm thick, are shown for comparison. In the unpassivated pure Cu film, a certain amount of stress is relaxed at temperatures above 250 °C, which gives rise to a characteristic stress drop (A) in the heating cycle, and to a kink (B) in the cooling cycle. Both characteristic features are absent in the self-passivating alloy film. In this section, it is shown that the stress relaxed in the pure Cu film (i.e. the shaded region between the two curves in Figure 5-6) is in accordance with a constrained-diffusional creep model. The creep laws applied so far for modeling the high-temperature mechanical behavior of Cu films were based on bulk models (see section 2.2.3 for a literature overview). In contrast to this, constrained diffusional creep is a model derived for the specific geometry of a thin film attached to a stiff substrate (Gao et al. 1999).

In this mechanism, surface atoms are plated into the grain boundaries (tensile stress) or vice versa (compressive stress). Good film adhesion provided, this mechanism relaxes the in-plane stress only at the grain boundaries, thus giving rise to an inhomogeneous stress state in the film.

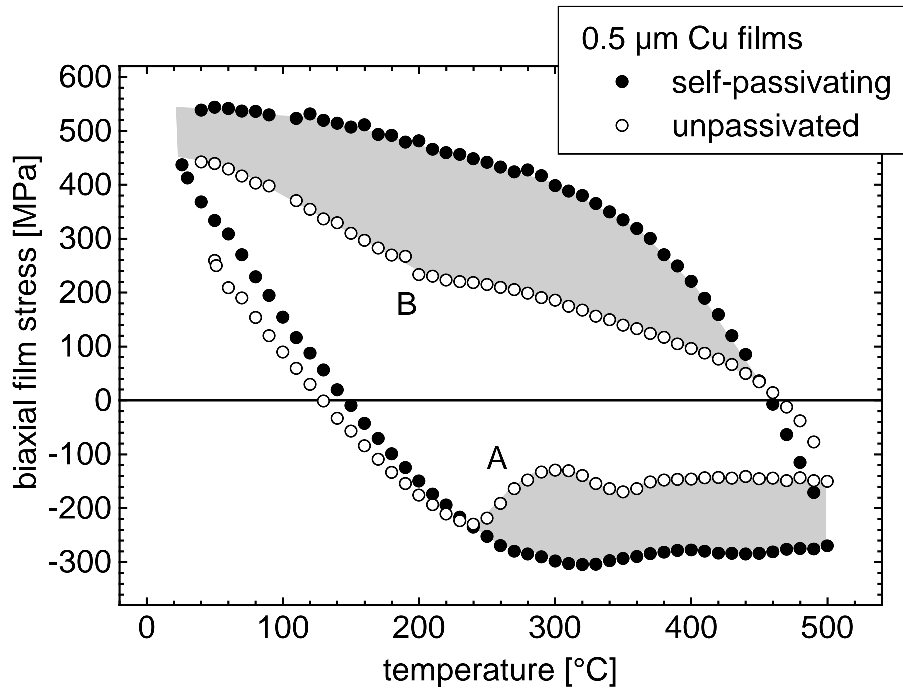

Figure 5-6 Stress-temperature curves of a self-passivating Cu-1at.%Al film [132] (Al-type) and of an unpassivated Cu film [119] (UHV Cu-type). The difference in stress between both curves (the shaded regions) is explained by constrained diffusional creep.

On the left-hand side of Figure 5-7, a schematic of this mechanism for the case of tensile stress is shown. As one pre-condition for this process, surface diffusion must be active because the surface acts as source for grain boundary atoms. This explains the passivation effect: a well adhering capping layer would obstruct diffusion at the film/passivation interface and thus inhibit the source for atoms for diffusional creep. This is schematically shown on the right-hand side of Figure 5-7. In such a case, the evolution of film stress would be determined only by dislocation glide (Al-type behavior).

In this section, the mathematical solution of the transient grain boundary traction under constrained diffusional creep by Gao et al. (1999) is presented first. It provides basic relations for the model developed for the simulation of the evolution of average stress in a Cu film during thermal cycling. Two cases are studied: First, dislocation plasticity is neglected. Stress-temperature curves are calculated with constrained diffusional creep as the

only plastic deformation mechanism. In a second step, dislocation plasticity is added to the simulation. With this model, the stress-temperature curve of a Cu thin film can be correctly described.

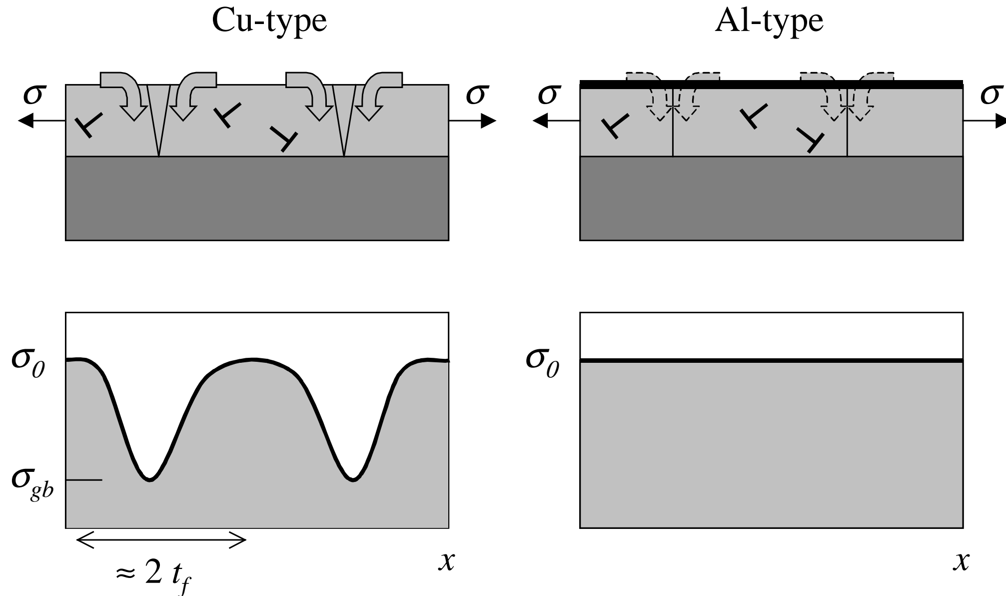

Figure 5-7 Schematic picture of the stress relaxation mechanisms (top) and the resulting stress distributions (bottom) proposed for Cu-type and Al-type mechanical behavior. Stresses are relaxed by glide and constrained diffusional creep in the case of Cu-type behavior. σ_0 denotes the intragranular stress not relaxed by the creep mechanism, and σ_{gb} denotes the average normal grain boundary traction. Stresses are relaxed by dislocation glide alone in the case of Al-type behavior. The schematic stress curves describe the in-plane stress, averaged over film thickness.

Gao's model

Grain-boundary diffusional creep in a foil with a two-dimensional, columnar grain structure was first described by Gibbs (1966). Creep deformation is due to the transport of surface atoms into the grain boundaries under tensile stress, or due to the transport of grain boundary atoms onto the surface under compressive stress. However, the author did not consider a constraining substrate. The creep equation derived by Gibbs (1966) for a free-standing foil is

$$\dot{\varepsilon} = A_{gb} \frac{\Omega \delta D_{gb}}{k_B T d t_f^{\,2}} \sigma , \tag{5-4}$$

where A_{gb} is a constant of approximately 15, Ω is the atomic volume, and δD_{gb} is the grain-boundary width times the grain-boundary diffusivity. In Figure 5-8, a simulated stress-temperature curve for a 0.3 µm thick film based on equation (5-4) is compared with experimental data. The model predicts that the film stress would be fully relaxed above 300 °C. This, however, is in conflict with the experimental data which are shown in the same plot for comparison. The simulation was carried out with Mathematica4.0 software, following the same procedure as described in detail for equation (5-3).

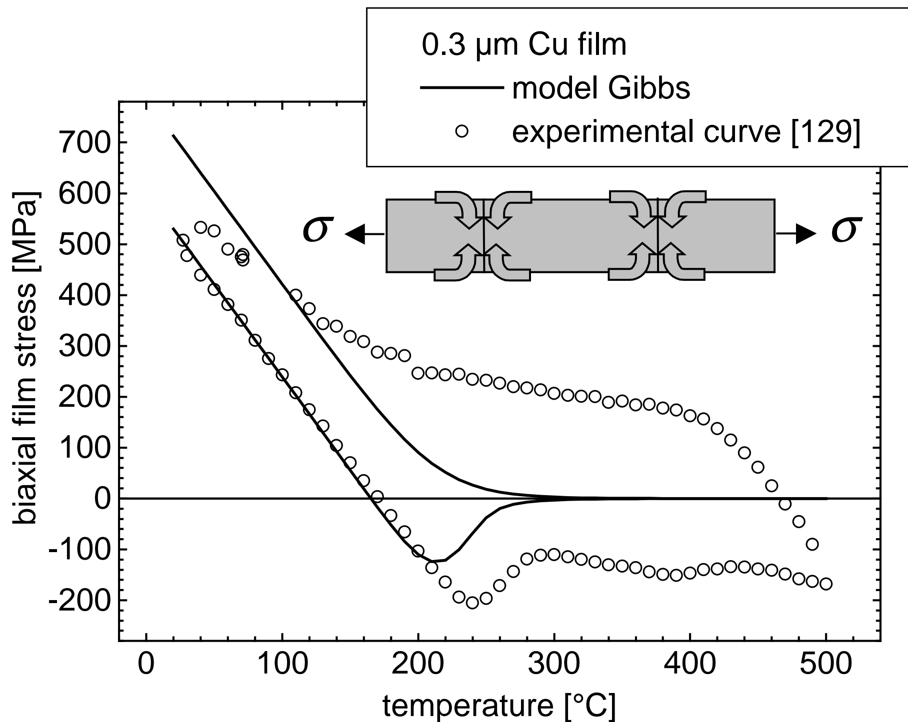

Figure 5-8 Simulated stress-temperature curve for a 0.3 µm thick Cu film using the model after Gibbs (1966) for grain-boundary diffusional creep of a free-standing foil, equation (5-4). The experimental curve of a film on a substrate is shown for comparison. The parameters used for the simulation A_{gb} = 15, $\Omega = 1.18\times10^{-29}$ m^3, $\delta D_{gb} = 5\times10^{-15}$ exp(-104 kJ mole^{-1}/RT) m^{3}s^{-1} (Frost and Ashby 1982, p. 21), and d = 0.9 µm. A schematic for grain boundary diffusional creep of a foil under tensile stress is inserted. The other parameters are the same as in Figure 5-5.

It was pointed out by Jackson and Li (1982) that, in the presence of a constraining substrate, stress could be relaxed only at the grain boundaries, while the stress at the film/substrate interface would remain unchanged. The average film stress would in this case be non-zero, even for fully relaxed grain boundaries.

The first rigorous mathematical analysis of the evolution of the grain boundary traction under constrained diffusional creep in a polycrystalline thin film with columnar grains was presented by Gao et al. (1999). In this analysis, no sliding or diffusion was allowed at the film/substrate interface. Earlier mathematical formulations of this problem (see e.g. Thouless 1993) implicitly allowed the grains to slide freely on the substrate, as Gao et al. point out. The analysis was carried out for the ideal case in which surface diffusion was considered to be very fast, and grain boundary grooving was neglected. The diffusion process, as described by the authors, leads to the formation of diffusion wedges at the grain boundaries, such as shown schematically on the left-hand side of Figure 5-7. The authors modeled a diffusion wedge as an array of climbing edge dislocations, such that Eshelby´s strain-field solution of a single edge dislocation close to a free surface could be used as a Green's function for the exact solution of the grain boundary traction problem.

As a result of the analysis, the traction at the grain boundary resembles that of a mode I crack, showing a stress singularity at the wedge tip at the film/substrate interface. The film stress distribution around a diffusion wedge is inhomogeneous both in the film plane and in the direction normal the film plane: Stress is relaxed more efficiently closer to the film surface and closer to the grain boundary. The intragranular stress remains unaffected by this mechanism. The shear stresses developing at the grain boundaries associated with the gradient in in-plane stress must be sustained by the film/substrate interface. The average grain boundary traction was shown by Gao et al. (1999) to follow an exponential time law. In a first order approximation, it is given as

$$\sigma_{gb}(t) = \sigma_0 \exp\left(-\frac{\lambda t}{t_0} \right), \tag{5-5a}$$

with the stress, σ_0, at the beginning of the relaxation, a characteristic time,

$$t_0 = \frac{4\pi\left(1-\nu^2\right)k_B T t_f^{\ 3}}{E_f \delta D_{gb} \Omega}, \tag{5-5b}$$

where ν and E_f are Poisson's rato and Young's modulus of the film material, and λ is a geometry-dependent constant defined as

$$\lambda = 8.10 + 30.65\frac{t_f}{d} \qquad \text{(for } 0.2 \le \frac{t_f}{d} \le 10\text{)}. \tag{5-5c}$$

Equation (5-5) will be the basis for the simulation of the stress evolution of Cu films during thermal cycling in this work.

The average film stress

The inhomogeneous stress state that develops under constrained diffusional creep is related to an average stress, σ. The average stress is of importance for the experimentalist, because this is the stress determined from the substrate curvature, when Stoney's formula (3-4) is applied. The average stress is a function both of the intragranular stress, σ_0, and of the grain boundary stress, σ_{gb}, as well as of the film thickness to grain size ratio, d/t_f. It was calculated by Gao (1999), using the equation for the energy release rate of a crack tip in a thin elastic film by Xia and Hutchinson (1999), to

$$\sigma = \sigma_0 - (\sigma_0 - \sigma_{gb})\left(\frac{4t_f}{d}\tanh\left[\frac{d}{4t_f}\right]\right). \tag{5-6}$$

Note that equation (5-6) becomes $\sigma = \sigma_0$ for the case of unrelaxed grain boundary stress ($\sigma_{gb} = \sigma_0$), while it has the form

$$\sigma = \sigma_0\left(1 - \frac{4t_f}{d}\tanh\left[\frac{d}{4t_f}\right]\right) \tag{5-7}$$

for fully relaxed grain boundaries ($\sigma_{gb} = 0$). Equation (5-7) is plotted in Figure 5-9. As expected, σ/σ_0 approaches unity for an increasing ratio d/t_f, and σ/σ_0 approaches zero for decreasing d/t_f.

It is noted, that equation (5-7) also describes the average stress in a film consisting of separate islands with island size d (the stress distribution in a grain with vanishing normal traction along the grain boundaries is identical to the stress distribution in an island, where the normal stress along the surface is zero).

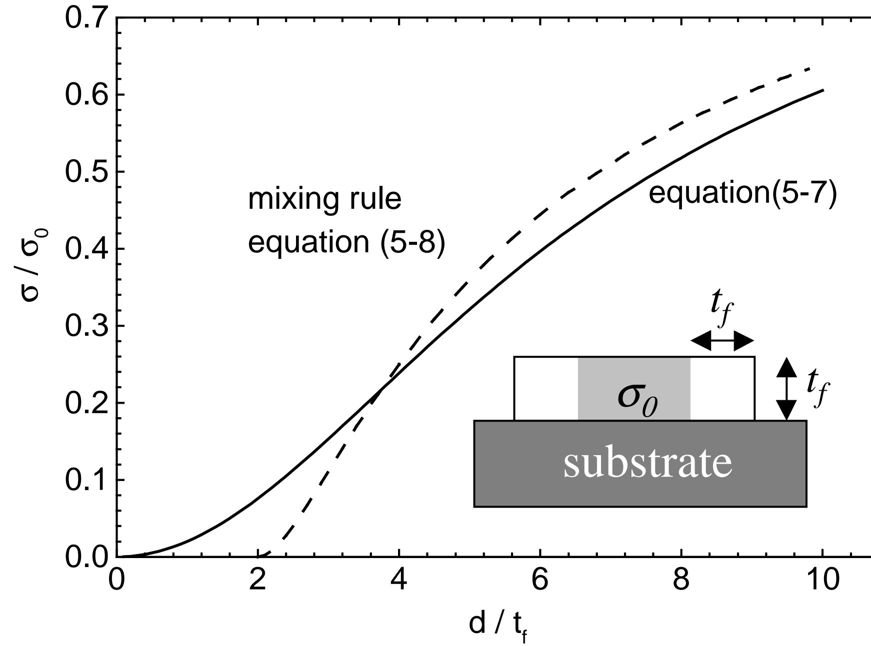

Figure 5-9 The ratio of average stress to intragranular stress, σ/σ_0, plotted versus the grain size to film thickness ratio, d/t_f. Equation (5-7) after Xia and Hutchinson (1999) is compared to a simple geometrical model based on Saint-Venant's principle, equation (5-8). The schematic of an island on a substrate with the simplified stress distribution, upon which equation (5-8) is based, is inserted.

It is further noted, that equation (5-7) can be approximated by a simple geometrical mixing rule, applying Saint-Venant's principle. The resulting equation,

$$\sigma = \frac{\sigma_0 \left(d - 2t_f\right)^2}{d^2}, \tag{5-8}$$

is plotted in Figure 5-9 for comparison. A good agreement with the more exact equation (5-7) is confirmed. Equation (5-8) represents the volume-average of in-plane stress in an island, idealized as a step-function, which is shown in the inserted schematic in Figure 5-9. In-plane stress is zero in a zone along the perimeter of the island. The width of the stress-free zone is equal to the island thickness, t_f, which can be estimated using Saint-Venant's principle. Saint-Venant's principle states that the width of any localized stress concentration due to an externally applied load is of the same length scale as the width of the area under the applied load. The island with vanishing normal traction along the perimeter is

thereby regarded as a grain in a film with unrelaxed boundaries, to which an "external load" of magnitude -σ_0 is applied.

Modeling constrained diffusional creep

The evolution of thermal stress in Cu films during thermal cycling is now described in the limit that constrained diffusional creep, as described by Gao's model, is the only stress relaxation mechanism. At this stage of modeling, plastic yielding by dislocation glide is neglected. Figure 5-10 shows a simulated stress-temperature curve for 0.3 µm thick Cu films with different grain sizes. As a numerical tool, Mathematica 4.0 software was used. Details of the numerical procedure are found in Appendix B. A homogeneous, tensile stress state of 500 MPa at the beginning of the heating cycles was assumed. The intragranular stress, σ_0, was modeled throughout the whole thermal cycle as a thermoelastic line with the slope

$$\frac{d\sigma_0}{dT} = -\Delta\alpha M_f \,, \tag{5-9}$$

as obtained from equations (2-2) - (2-4). Literature values (Appendix A) for $\Delta\alpha$ and M_f for (111)-orientation at 300 K were used for the simulation.

The evolution of the normal grain boundary traction, σ_{gb}, was calculated by numerical integration of the equation

$$\sigma_{gb}(t) = \int_0^t \exp\left[-\lambda \int_\xi^t \left(\frac{d\zeta}{t_0(\zeta)}\right)\right] d\sigma_0(\xi), \tag{5-10}$$

where ξ and ζ are integration parameters (Gao 1999). This equation, which is based upon equation (5-5a), is explicitly derived in Appendix B. The average stress, σ, was calculated with equation (5-6).

Figure 5-10 (a) shows the simulated average, intragranular, and grain boundary stress during thermal cycling for a 0.3 µm thick Cu film with a grain size of 0.9 µm. The curves in this plot are interpreted as follows. Upon heating, stress evolves homogeneously, until grain boundary diffusion sets in at approximately 250 °C. The normal grain boundary traction, σ_{gb}, subsequently relaxes to zero, giving rise to a characteristic stress drop in the av-

erage stress curve. The model assumes that the normal grain boundary traction is relaxed by diffusion of grain boundary atoms to the surface. Following the stress drop between 250 and 300 °C, the average stress again assumes constant slope, but it does not relax to zero because of the unrelaxed intragranular stress. This is in contrast to Gibbs' model, after which the whole film stress would relax to zero as shown in Figure 5-8. The slope of the average stress for fully relaxed grain boundary stress after the stress drop is

$$\frac{d\sigma}{dT} = -\Delta\alpha M_f \left(1 - \frac{4t_f}{d}\tanh\left[\frac{d}{4t_f}\right]\right), \tag{5-11}$$

which is obtained from equations (5-7) and (5-9).

The average stress follows the same line upon cooling until 300 °C, below which the kinetics are insufficient for grain boundary diffusion. According to the constrained diffusional creep model, grain boundary stress in this part of the cooling curve is relaxed by diffusion of surface atoms into the grain boundaries (see Figure 5-7). At the end of the cooling cycle, an inhomogeneous stress state is sustained, in which the grain boundary traction is higher than the intragranular stress.

The grain size to film thickness ratio has a large influence on the average stress, if an inhomogeneous stress state is found in the film due to constrained diffusional creep. This is expressed by equation (5-6). Figure 5-10 (b) shows the simulated stress-temperature curve of a 0.3 μm thick Cu film with a grain size twice as large as the value simulated in Figure 5-10 (a). The average stress, σ, is dominated more strongly by the intragranular stress, σ_0, than it is the case in the smaller grained film. It is noted that the intragranular stress is the same as in (a). Also, the normal grain boundary traction, σ_{gb}, is practically the same as in (a), as it depends only weakly on grain size through the structural parameter, λ, as expressed by equation (5-5c).

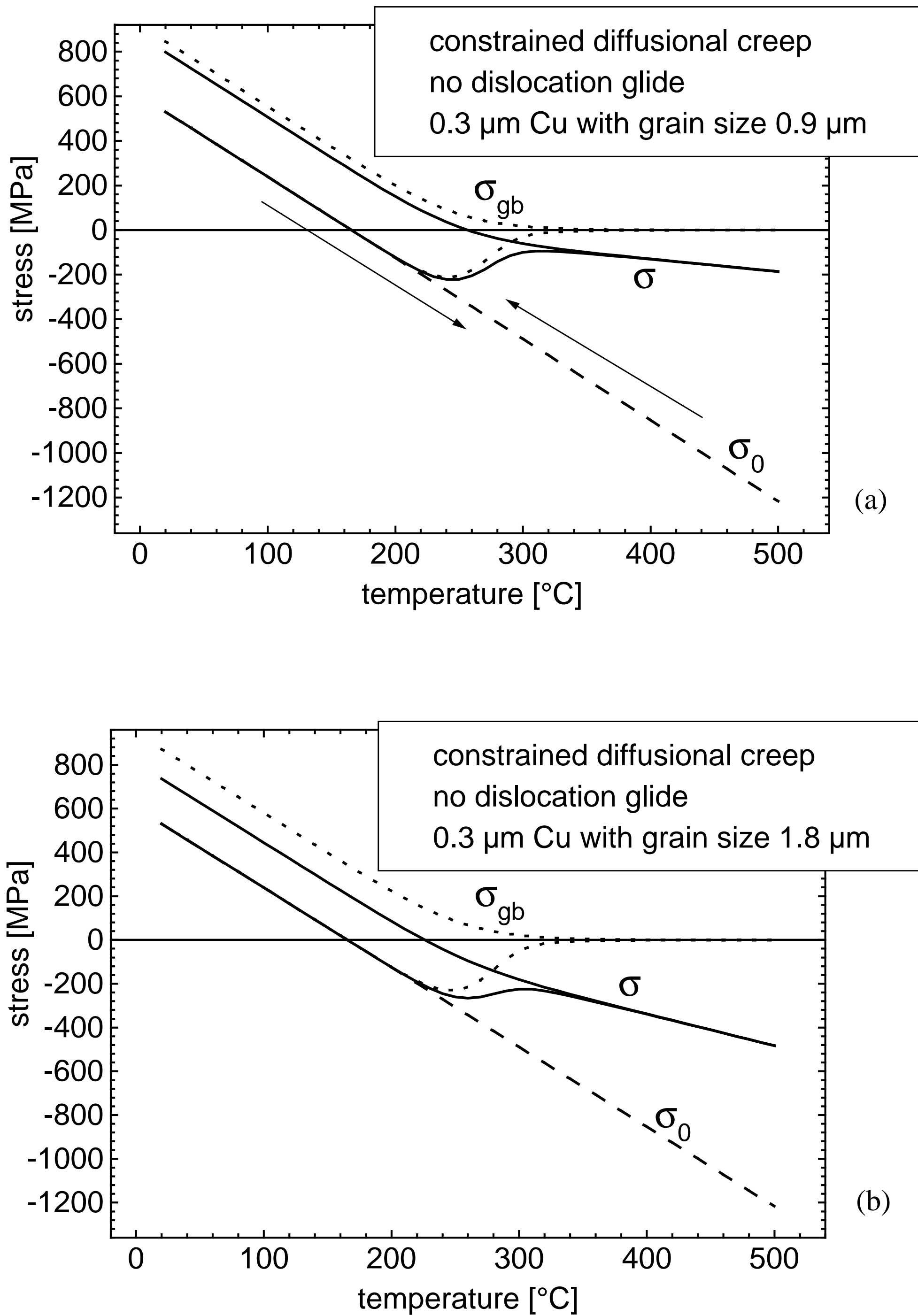

Figure 5-10 Simulated stress-temperature curves for 0.3 µm thick Cu films with constrained diffusional creep as the only plastic deformation mechanism. σ is the average stress, σ_{gb} is the grain boundary stress, and σ_0 is the intragranular stress. The grain size was 0.9 µm in (a), and 1.8 µm in (b). The other parameters were $\Delta\alpha = 1.4\times10^{-5}$ K^{-1}, $M_f = 2.6\times10^{11}$ Pa, $\dot{T} = 0.1$ Ks^{-1}, $\delta D_{gb} = 5\times10^{-15}$ exp(-104 kJ mole^{-1}/RT) m^{3}s^{-1} (Frost and Ashby 1982, p. 21), $\Omega = 1.18\times10^{-29}$ m^3, $E = 1.24\times10^{11}$ Pa, and $\nu = 0.34$, for both simulations.

Comparison with experimental data

In the following, the effect of film thickness on the stress evolution under constrained diffusional creep is studied. Simulated stress-temperature curves are compared with experimental curves for 0.3 µm, 0.5 µm, and 1.0 µm thick Cu films. It is expected that the agreement between simulated and experimental curves becomes worse as the film thickness increases, for plastic film deformation by dislocation glide, neglected in these simulations, becomes easier with increasing film thickness (see section 5.3.1).

In Figure 5-11, the experimental stress-temperature curve for a 0.3 µm thick Cu film is compared to the simulated average-stress curve from Figure 5-10 (a). The stress at the beginning of the heating cycle was adjusted in the simulated curve to fit the experimental stress. The agreement of both curves in the heating cycle is striking, whereas a large discrepancy is found during cooling. Three salient features found in the heating curves are discussed in the following.

First, the experimental curve is perfectly linear between room temperature and 250 °C. The slope matches, within the error of the measurement, that of the simulated curve, which is based on literature data for (111)-textured Cu and which thus was not adjusted to match the experimental data. Consequently, no significant plastic yielding by dislocation glide occurred in the film during this part of the thermal cycle, because the slope of the stress-temperature curve is not further reduced. Second, the modeled characteristic stress drop in compression between 250 and 300 °C is in good agreement with the experimental data. Note that a literature value for the grain boundary diffusivity was used for the simulation (Frost and Ashby 1982, see caption of Figure 5-10). As the third feature, the almost constant slope of the experimental heating curve following the characteristic stress drop in compression is noted. This feature is also described by the model. However, the actual grain size of the film was not known; instead, the grain size parameter was adjusted to fit the experimental slope. Moreover, the true intragranular stress, which could not be measured, would be expected to have relaxed by dislocation glide, such that matching with the experimental data in this segment may be regarded as accidental.

The discrepancy between the cooling curves is also expected to result from neglecting dislocation glide. This will be understood after the discussion of the curve simulations based on both mechanisms, glide and creep, below.

Simulated and experimental stress-temperature curves for 0.5 and 1.0 μm thick Cu films are shown in Figure 5-12. The measured grain sizes from Table 4-1 were used for the calculations.

The modeled heating curves for the thicker films do not match the experimental curves as well as they do for the 0.3 μm thick film in Figure 5-11. The experimental heating curves deviate from the model curves at temperatures well below the onset of creep, indicated by the stress drop. This effect is interpreted as low temperature plastic deformation by dislocation glide. In all three films, the experimental cooling curve exhibits a steeper segment below 500 °C, which is not predicted by the model. This effect also is due to the neglect of dislocation glide, as will be demonstrated below. The model curves for the cooling cycle assume thermoelastic slope at low temperature. This is also in conflict with the experimental curves in which a decreased slope upon cooling indicates plastic flow.

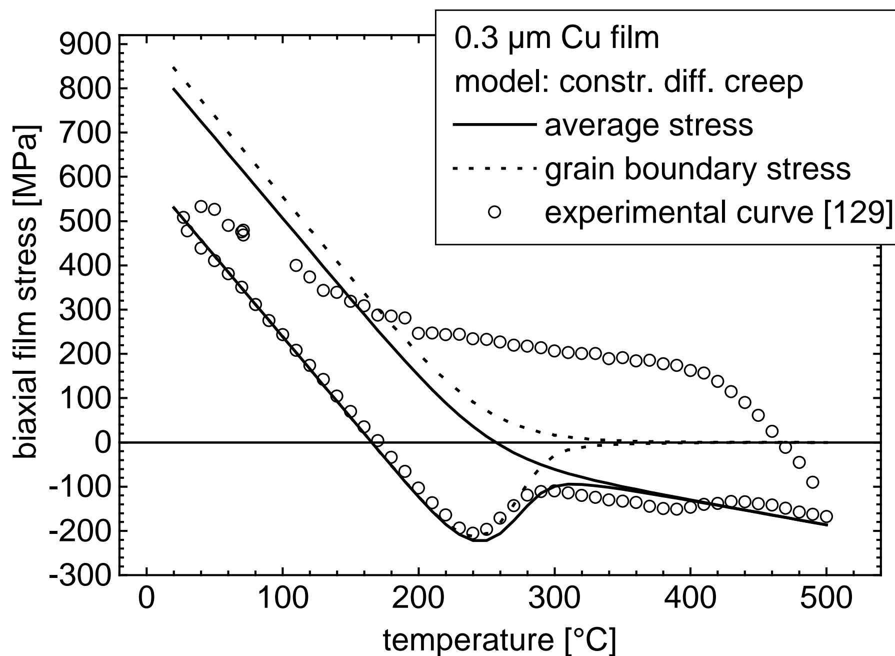

Figure 5-11 Simulated and experimental stress-temperature curves for a 0.3 μm thick Cu film. The simulated curve is the same as in Figure 5-10 (a). It is based upon constrained diffusional creep as only relaxation mechanism. The intragranular stress is modeled purely thermoelastically. Fit parameters are grain size, $d = 0.9$ μm, and activation energy for grain boundary diffusion, $E_a = 104$ kJ mole^{-1}.

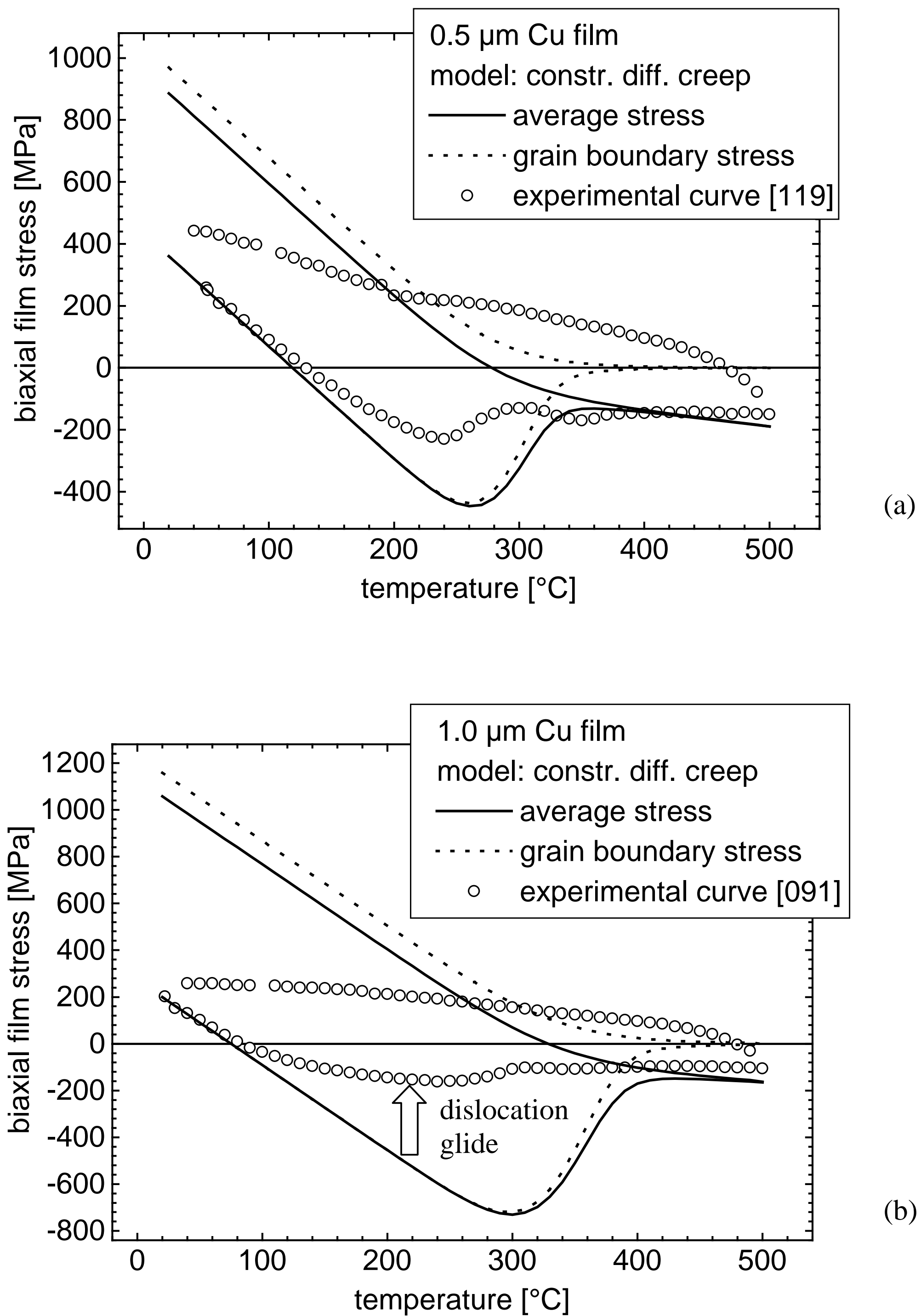

Figure 5-12 Simulated and experimental stress-temperature curves for 0.5 µm (a) and 1.0 µm (b) thick Cu films. The simulations are based upon constrained diffusional creep as the only stress relaxation mechanism: The intragranular stress, which is not shown in this figure, follows the thermoelastic line (see Figure 5-10). Thus, dislocation glide is neglected in theses calculations. The experimental grain size of 1.4 µm for (a) and 2.4 µm for (b) were used for the simulations. The other parameters are the same as given in the caption of Figure 5-10.

The decreasing degree of agreement of experimental and theoretical curves with increasing film thickness is explained by the adverse effect of film thickness on constrained diffusional creep and glide: Creep becomes more effective with decreasing film thickness, while the opposite is the case for dislocation glide. The film thickness dependency of creep is manifested in the time constant for creep, t_0, in equation (5-5b), which scales with the third power of film thickness. This effect is noted in the simulated grain boundary stress in Figure 5-11 and Figure 5-12: the apparent onset of creep in the heating cycle is shifted from 240 °C in the 0.3 μm thick film to 300 °C in the thicker, 1.0 μm thick film. Also, the temperature region in which the grain boundary stress relaxes to zero becomes broader with increasing film thickness. A similar effect is found in the cooling curves, where the temperature at which the grain boundary stress starts to build up is shifted from 300 °C in the 0.3 μm thick film to approximately 450 °C in the 1.0 μm thick film. Note that the increasing effectiveness of grain boundary diffusional creep with decreasing film thickness is related to the similar effect observed in Coble creep in three-dimensional grain structures, for which the creep rate scales with the inverse of the third power of grain size.

Dislocation glide, on the other hand, becomes more effective with growing film thickness. This will be discussed in section 5.3.

In summary, the simulations based on constrained diffusional creep as the only relaxation mechanism described several features of the experimental data quite well, such as the characteristic stress drop in the compressive region in the heating cycle and the linear segment with decreased slope following the stress drop. However, other features such as the steep segment at the onset of cooling were not represented. The agreement of simulated and experimental curves worsened with increasing film thickness, which was explained by the growing effectiveness of dislocation glide. Consequently, dislocation glide was incorporated into the simulations in a next step.

Modeling constrained diffusional creep plus dislocation glide

Figure 5-13 shows the calculated stress-temperature curve for a 0.5 μm thick unpassivated Cu film based upon constrained diffusional creep *and* dislocation glide. The intragranular stress, σ_0, was modeled with the constitutive equation (2-11) for thermally activated dislocation glide. The grain boundary stress, σ_{gb}, was calculated with equation (5-10) for con-

strained diffusional creep. As for the model curves shown above, the average stress, σ, was obtained from both stresses, σ_0 and σ_{gb}, applying equation (5-6). The code for Mathematica4.0 for the calculation is found in Appendix B.

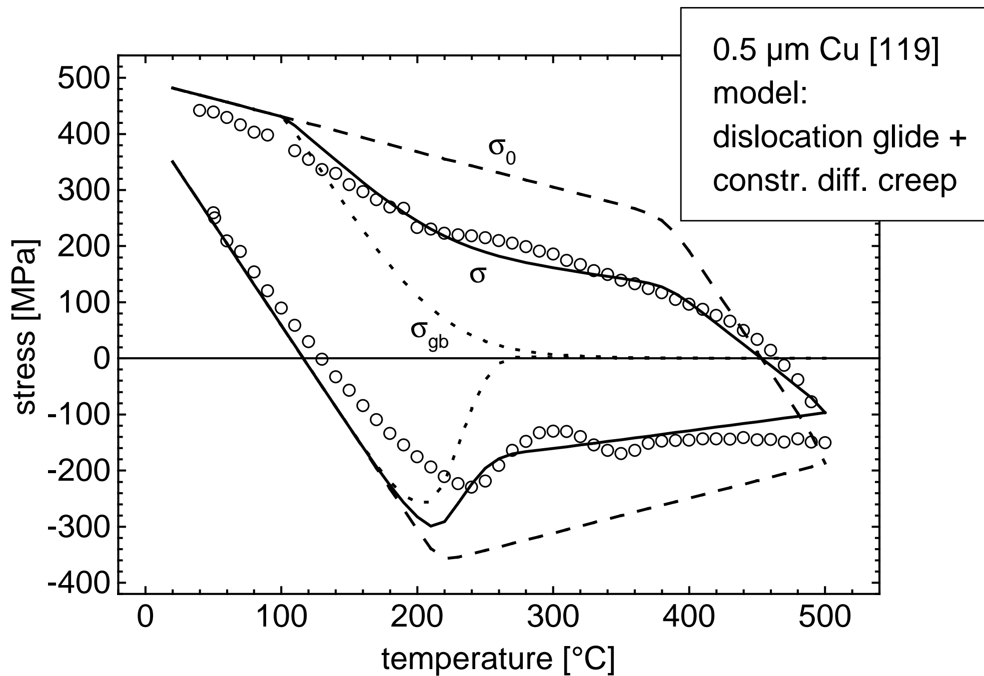

Figure 5-13 Simulated and experimental stress-temperature curves for a 0.5 µm thick unpassivated Cu film. σ_0 was modeled with equation (2-11) for thermally activated dislocation glide with the parameters $\dot{\varepsilon}_0 = 1\times10^3$ s^{-1}, $\Delta F = 3.0\times10^{-19}$ J, and $\hat{\tau} = 180$ MPa. σ_{gb} was modeled on the basis of equation (5-10) for constrained diffusional creep. Fitting parameters were the activation energy for grain boundary diffusion, $E_a = 90$ kJ/mole, and grain size, $d = 4$ µm. The other parameters are the same as in the captions of Figure 5-5 and Figure 5-10.

The calculated stress-temperature curve describes all important features of the experimental curve. Unlike for the calculated curve in Figure 5-12 (a), even the cooling curve fits well to the experimental data. The only significant difference between both cases is the shape of the σ_0-curve, which was modeled linearly in Figure 5-12 (a). Another difference between both models is the grain size parameter; it was set to 4 µm for the evaluation of the average stress in Figure 5-13. If the experimental grain size of 1.4 µm from Table 4-1 was used, the modeled average stress at temperatures above 300 °C would have been too small. However, it is pointed out that the "true" intragranular stress was not known. The grain size parameter is discussed in further detail below.

The activation energy for grain boundary diffusion in Figure 5-13 was set to 90 kJ/mole, which is lower than the value of 104 kJ/mole used in Figure 5-12 (a). The lower activation energy is responsible for the shift of the relaxation of grain boundary stress towards lower temperatures, as can be seen upon comparison of both simulations. Obviously, the average stress curve in Figure 5-13 fits better to the experimental cooling curve than it does for the heating curve. In the latter case, the stress drop is found at a too low temperature. This asymmetry of the experimental curve with respect to the onset of grain boundary diffusion could not be explained. The activation energy for grain boundary diffusion is further discussed below.

Figure 5-14 (a) shows the schematic of a different approach for modeling the stress-temperature curve of an unpassivated Cu film. The basic idea is to describe the intra-granular stress of the unpassivated film by the experimental stress-temperature curve of a self-passivating Cu-Al alloy film with equal film thickness, grain size, and texture. For simplicity, it was assumed that constrained diffusional creep was totally suppressed in the self-passivated film. It was furthermore assumed that the passivation had no influence on dislocation glide. For the numerical calculation, the intragranular stress was described by a 5th-order polynomial fit of the stress-temperature curve of the 0.5 μm thick Cu-1at.%Al film shown in Figure 5-6. In a second step, the grain boundary stress, σ_{gb}, was calculated with equation (5-10) for constrained diffusional creep. Finally, the average stress, σ, was obtained using equation (5-6).

The resulting average stress curve in Figure 5-14 (b) matches the experimental data well. This result supports the statement made earlier, namely that the difference in thermal stress between a self-passivating and the pure Cu film is due to constrained diffusional creep (see Figure 5-6).

As for the curve in Figure 5-13, a larger grain size parameter (4.0 μm) was required to fit the experimental stress in the high temperature regime. The other parameter adjusted was activation energy for grain boundary diffusion. Different activation energies were used for heating and cooling cycles to take into consideration the asymmetry of the experimental with respect to the onset of grain boundary diffusion. Both parameters are discussed in the following.

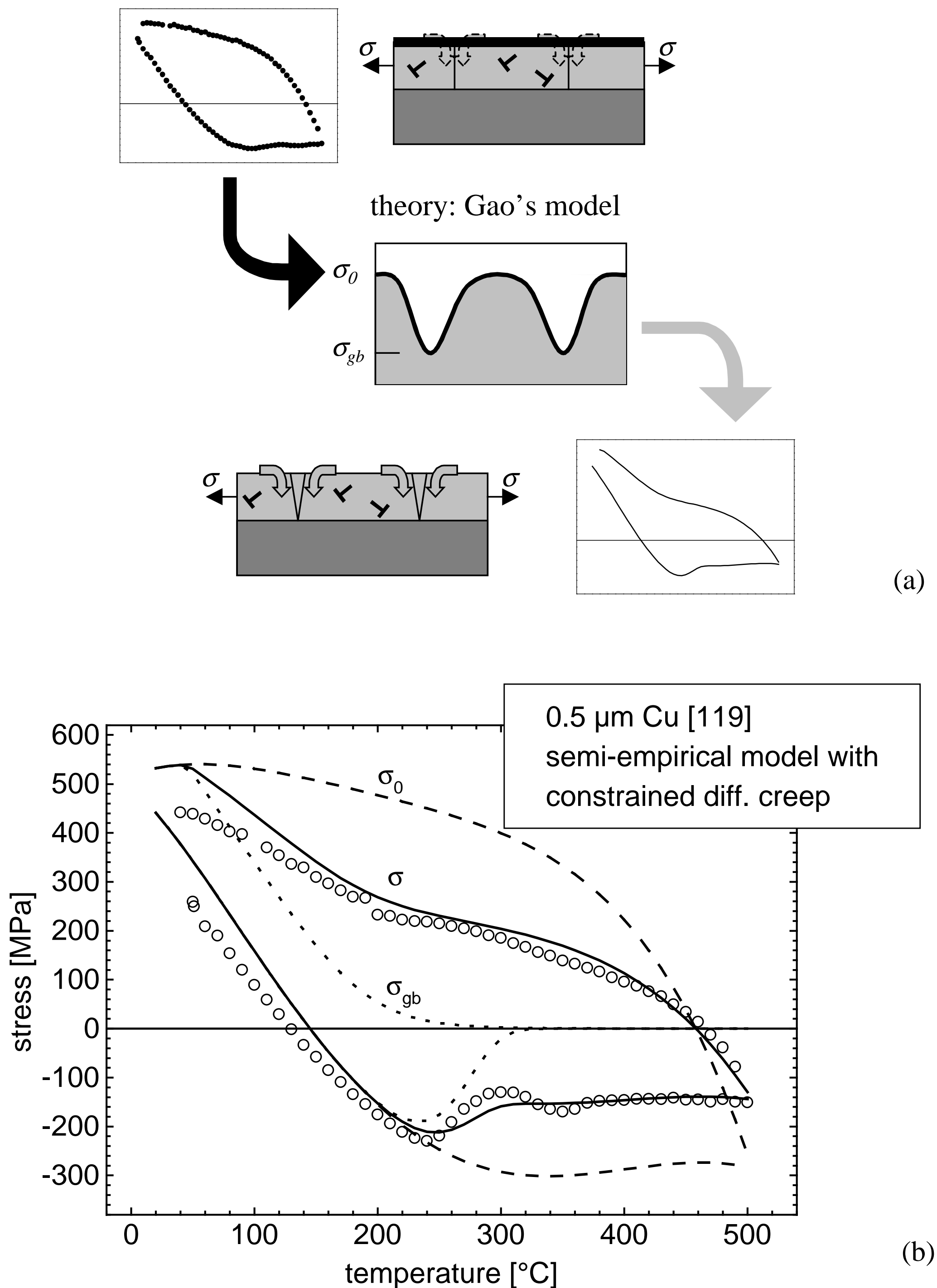

Figure 5-14 (a) Schematic for the semi-empirical approach for modeling the stress-temperature curve of a 0.5 µm thick unpassivated Cu film in (b). The intragranular stress, σ_0, was described by a 5th-order polynomial fit of the experimental stress-temperature curve of a 0.5 µm thick self-passivating Cu-1at.%Al film. The grain boundary stress, σ_{gb}, was modeled on the basis of equation (5-10) for constrained diffusional creep. The activation energies for grain boundary diffusion were E_a = 97 kJ/mole for heating and E_a = 85 kJ/mole for cooling. Grain size was set to 4 µm. The other parameters are the same as in the caption of Figure 5-10.

Two possible explanations for the large grain size parameter are discussed. First, the effective grain size would be higher by a factor of 1.5 if both low angle tilt boundaries with tilt angles below 15° and Σ3-twin boundaries were omitted from the grain boundary statistics. Both types of boundaries have a high degree of structural order if compared to high angle tilt boundaries. The activation energy for diffusion would be too high for a significant amount of mass transport along these boundaries. This view is supported by the absence of creep voids at these types of boundaries in oxidized Cu-Al films (see section 5.4). If the grain boundary statistics from the OIM measurements in Table 4-3 (pure Cu) and Table 4-5 (Cu-1at.%Al) are considered, the correction factor of $f = 1.5$ can calculated on the basis of the equation

$$f = \frac{(N_{HA} - N_{\Sigma 3}) + N_{LA}}{(N_{HA} - N_{\Sigma 3})}, \qquad (5\text{-}12)$$

where $(N_{HA} - N_{\Sigma 3})$ is the number of counts for high angle boundary segments without twin boundary segments and N_{LA} is the number of counts for low angle boundary segments detected in the OIM measurements. For the Cu film (Table 4-3), a factor $f = 1.3$ and for the alloy film (Table 4-5), a factor of 1.6 is found, from which the average was taken. It is noted that these values are based upon only poor statistics due to the small number of grains mapped by the measurement. The alloy film was regarded here because no alloying effect of 1at.%Al on texture was found (see discussion in section 5.1.2).

Taking into account the correction factor $f = 1.5$, an effective grain size of $d_{eff} = f \times d =$ 2.1 μm is obtained. However, this is still too small if compared to the grain size of $d = 3.9$ μm used for the simulation.

A second explanation for this effect may be the existence of a threshold for the grain boundary stress. A threshold stress might be explained by oxidation of the film surface in the furnace of the wafer curvature apparatus. A non-zero grain boundary stress at high temperatures would lead to an increase in average stress, which could then be modeled with a smaller grain size to film thickness ratio (see Figure 5-9).

The second fitting parameter, the activation energy for grain boundary diffusion, is now discussed. The literature on activation energies for grain boundary diffusion in pure Cu shows a large scattering of values. The activation energy reported by Frost and Ashby

(1982, p. 21) is 104 kJ mole^{-1}. Surholt and Herzig (1997) reported on much lower values of 72.47 kJ mole^{-1} and 84.75 kJ mole^{-1} for highest and high purity metals, respectively. The large variety of data is due to the high sensitivity of diffusion in the presence of impurities. The activation energies used for the simulations, 90 kJ/mole in Figure 5-14 (a), and 97 kJ/mole and 85 kJ/mole in (b) fall into this range of literature values. As noted before, the discrepancy between heating and cooling in the experimental curve in Figure 5-14 is not understood.

This remark concerns constrained diffusional creep in the passivated films. It was assumed that constrained diffusional creep was totally suppressed in the self-passivating films because of the suppression of surface diffusion (see schematic in Figure 5-7). However, if diffusion at the film/passivation interface was not totally suppressed, a certain amount of stress could have been relaxed by this creep mechanism. Upon close inspection, the heating curve of the self-passivating film in Figure 5-6 exhibits a small stress drop between 320 and 400 °C, which could be due to this mechanism. In comparison to the pure Cu film, this stress drop is shifted towards higher temperatures. This would be expected if interfacial diffusion had a higher activation energy than grain boundary diffusion, and would therefore become rate limiting. A higher activation energy for interfacial diffusion is expected if bonding between film and oxide is strong, which seems a realistic assumption. However, direct experimental verification of this hypothesis was not within the scope of this work.

As a consequence of the preceding remark, diffusion at the film/substrate interface in the pure Cu films cannot be definitely excluded, either. The two thinner Cu films show a second, smaller stress drop in the heating curves at higher temperature (at 380 °C for the 0.3 µm thick film in Figure 5-11, and at 350 °C for the 0.5 µm thick film in Figure 5-6). This stress drop could be interpreted as the onset of interfacial diffusion, which, in the combination with grain boundary diffusion, would open a second diffusion path for stress relaxation.

It is concluded that the thermo-mechanical behavior of a Cu thin film can be described by two deformation mechanisms, thermally activated dislocation glide and constrained diffusional creep, which selectively relaxes grain boundary traction at high temperature. A recent mathematical description for constrained diffusional creep by Gao et al. (1999) was applied to model stress-temperature curves. Under this mechanism, the average normal

grain boundary stress is relaxed by combined surface and grain boundary diffusion. The intragranular stress is not affected by this mechanism due to the constraint of the substrate. Several questions remained open: It was not completely understood why a grain size pa-rameter three times larger than the experimental grain size had to be used for fitting the ex-perimental data. The asymmetry of the experimental curve with respect to the onset of grain boundary diffusion could not be explained, either. For future work, it is suggested to carry out local strain measurements in order to verify the inhomogeneous stress state re-sulting from constrained diffusional creep.

5.2.3 The vacuum quality effect (HV Cu-type)

In this section, the shape of curves of high-vacuum (HV) sputtered Cu films known from the literature is addressed. These films support lower stresses at high temperature than the UHV-sputtered films from this work discussed in the previous section. In Figure 5-15, UHV and HV Cu-type curves for 1 µm thick Cu films are shown together with the curve of the 1 µm thick Cu film which was sputtered without substrate cleaning by ion bombard-ment. Interestingly, this film exhibits a similar curve shape as the HV-sputtered film from Keller et al., characterized by decreasing stress above 300 °C during heating and lower stresses during cooling. The HV Cu-type curve shape, which is not completely understood, is qualitatively interpreted in the following.

A possible explanation for this vacuum quality effect is poor film adhesion. If bonding at the film/substrate interface is weak, the film can slide under the shear stresses which de-velop near the intersection of the grain boundary and the substrate interface as a result of diffusional creep. As a result, the average film stress would decrease to zero. The situation described is similar to the case of a free-standing film, for which diffusional creep was de-scribed by Gibbs' model (see Figure 5-8). It is pointed out, however, that sliding does not necessarily involve detachment of the film on a macroscopic scale; sliding may occur by diffusive processes, if bonding at the film/substrate interface is weak due to contamination at the interface. This explanation covers the passivation effect observed also in HV-Cu films (see section 2.2.3).

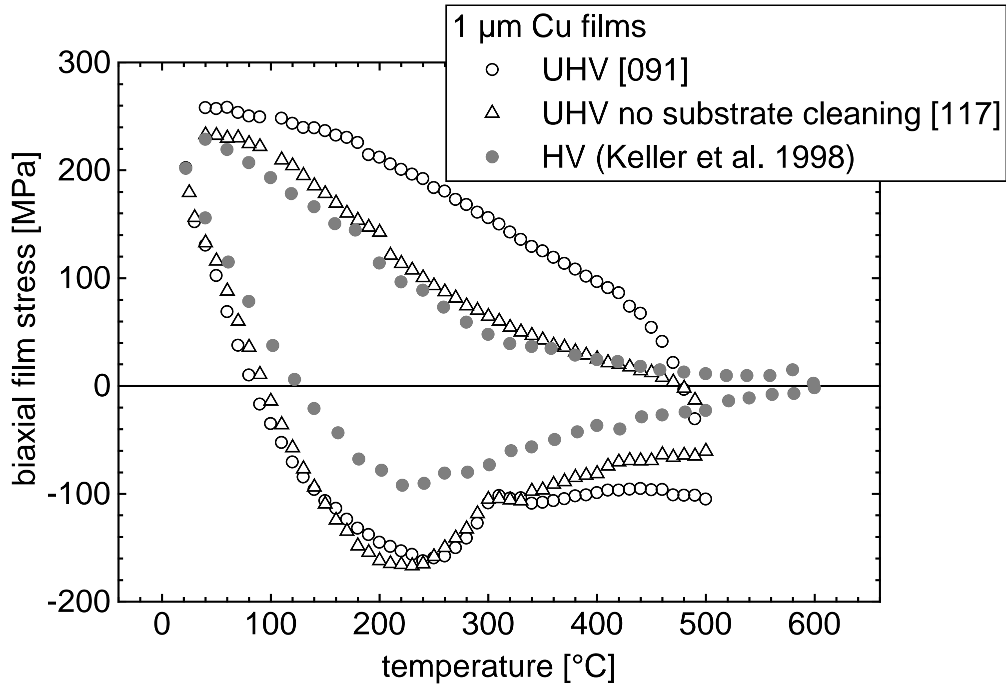

Figure 5-15 Stress-temperature curves for three different 1 µm thick Cu films on Si. Similar curves are found for the HV-film from the literature and the UHV-film produced without substrate cleaning, in which stresses relax towards zero at high temperatures.

A second effect contributing to lower average stresses at high temperature could be the smaller grain size and the weaker texture. HV-films exhibit a smaller grain size to film thickness ratio than UHV-films (Table 5-1). This is associated with lower average stresses if the grain boundaries are relaxed by grain boundary diffusional creep, as shown in Figure 5-9. The texture argument fits to both the HV-film and the UHV-film sputtered without substrate cleaning. The latter was less sharply textured than the film sputtered with substrate cleaning. In Figure 5-16, this difference is shown schematically. The grain boundaries in the less sharply textured film possess a certain twist character, whereas the grain boundaries in the sharply textured film are pure tilt boundaries.

The higher disorder in a twist boundary is associated with a higher grain boundary energy. This leads to higher diffusivity of such a grain boundary (see Nucci et al. (1997) and references therein). Thus, grain boundary diffusional creep is expected to be more effective in the film sputtered without substrate cleaning. The effect of texture on the effective grain size is expected to be even larger in the HV-sputtered films, as boundaries between differently oriented grains always have twist character. Keller (1996) reports a mixed texture of

70% (111)-oriented grains and 30% (100) and randomly oriented grains in a 1 μm thick Cu film.

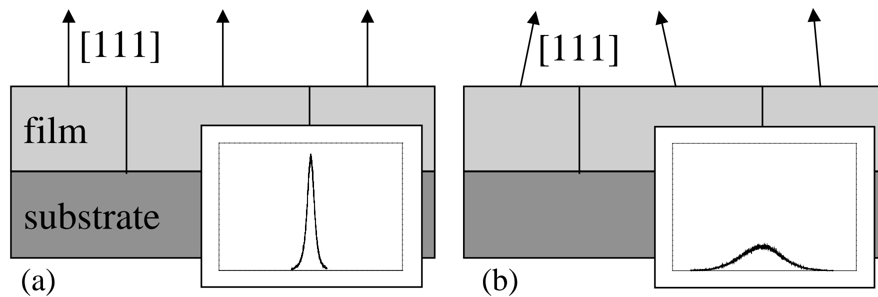

Figure 5-16 A sharp (111)-texture (a) of the 1 μm thick Cu film prepared with substrate cleaning from Figure 4-5 (a), and a less sharp (111)-texture (b) of the appropriate film prepared without substrate cleaning from Figure 4-5 (b).

A different explanation for decreased film stress at high temperatures is buckling. A film can buckle under a compressive stress if it is locally detached from the substrate. Buckling, which may occur on a microscopic scale, leads to too lower average stresses in the film. Upon cooling, the buckles would first have to be flattened out before a tensile stress can be built up in the film. This explanation does however not apply to the present case because it does not cover the passivation effect: the mechanical stability of a thin capping layer is not considered to be sufficient to suppress buckling.

5.3 Yield stress of Cu thin films

In this section, the effect of film thickness on the room temperature yield stress of pure Cu films is discussed. In section 5.3.1, the results from this work are compared to experiments and theoretical considerations in the literature. In section 5.3.2, activation volumes of thermally activated glide in a Cu film are evaluated. The apparent contradiction between the measured small activation volumes and the film thickness effect on yield strength motivates a new model presented in section 5.3.3. The quintessence of this model is that, below a certain critical film thickness, film deformation may become dislocation source controlled rather than obstacle controlled.

5.3.1 The film thickness effect on yield stress

Wafer curvature measurements

In section 5.2.2, the stress evolution in unpassivated Cu films during thermal cycling was discussed. At temperatures above approximately 250 °C, the average film stress was interpreted as a result from dislocation glide and constrained diffusional creep, generating an inhomogeneous stress state within the film. At room temperature, the creep mechanism becomes inactive and film stress is solely determined by dislocation glide. In the literature, it is customary to define the yield stress of a film as the film stress at the end of the cooling cycle in a wafer curvature experiment (see e.g. Venkatraman and Bravman 1992, Keller et al. 1998). In Figure 5-17, three stress-temperature curves of Cu films from this work are plotted together for comparison. The thinner films support higher stresses. The room temperature yield stress is plotted versus the inverse of the film thickness in Figure 5-18 (a). In this plot, corresponding data from HV-sputtered film from Keller et al. (1998) are also included. The data points for UHV and HV-films show good agreement. For the thicker films the yield stress shows a $1/t_f$-dependency. The yield stress of the thinnest, 0.3 µm-thick film is lower than predicted by the $1/t_f$-dependency. The intercept of the line at $1/t_f = 0$ at about 10 MPa is in the range of yield stresses of Cu single crystals (Diehl 1956). The yield stress of the UHV-films are plotted together with the stress at 500 °C, measured at the end of the heating cycle, of the same films on a double-logarithmic scale in Figure 5-18 (b). The slope of n = -0.9 for the room temperature values is close to the value of

n = -1 predicted by the Nix model, equation (2-8). However, the values predicted by this model are too small by a factor of approximately 5 (see the dashed line in Figure 5-18 a).

The stresses at 500 °C for UHV and HV-sputtered films in Figure 5-18 (a) do not fall together on one line. The reader is referred to section 5.2.3, in which this effect is di s-cussed. A second observation is that the thickness dependency of the yield stresses of the UHV films at 500 °C is less pronounced than at 40 °C. This is shown in Figure 5-18 (b), in which the slope the high-temperature stress is n = -0.6. This cannot by explained by the constrained diffusional creep model. This model predicts an opposite trend: the thinner films have a larger grain size to film thickness ratio (section 5.1.1) and should therefore have higher average stresses if the grain boundaries are stress-free (Figure 5-9). From this it is followed that the thickness dependence of the intragranular stresses becomes weaker at high temperatures.

In the following section, the activation volume of the thermally activated dislocation glide is suggested as an alternative concept allowing a deeper insight into the deformation mechanisms responsible for film strength. First, the measurements of film hardness at room temperature are discussed.

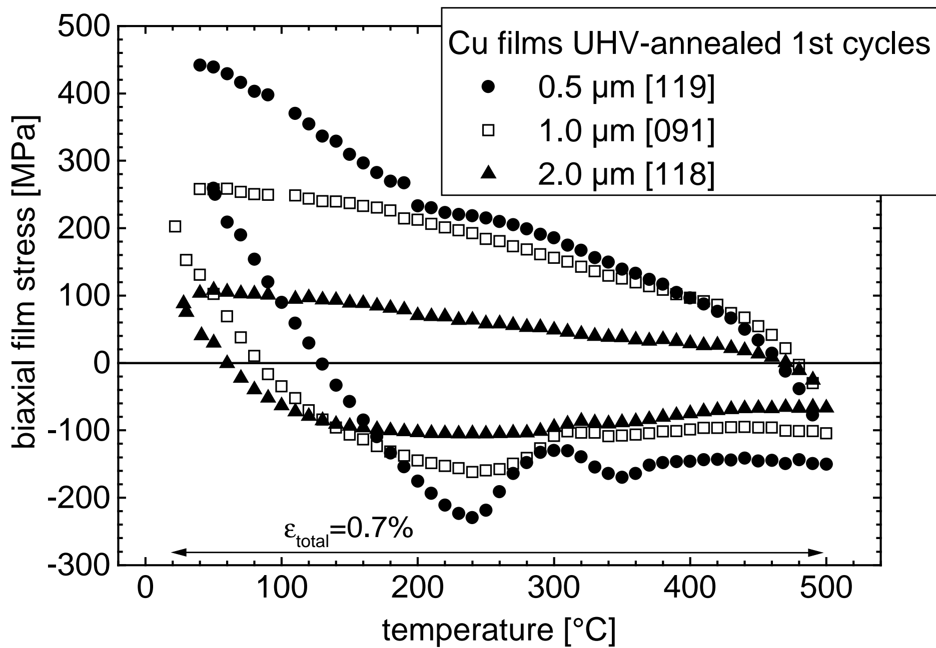

Figure 5-17 Stress-temperature curves for UHV-sputtered and annealed Cu films with different film thickness. Thinner films support higher stresses in the whole temperature range. The total thermal strain in one cycle is 0.7% (see Appendix A).

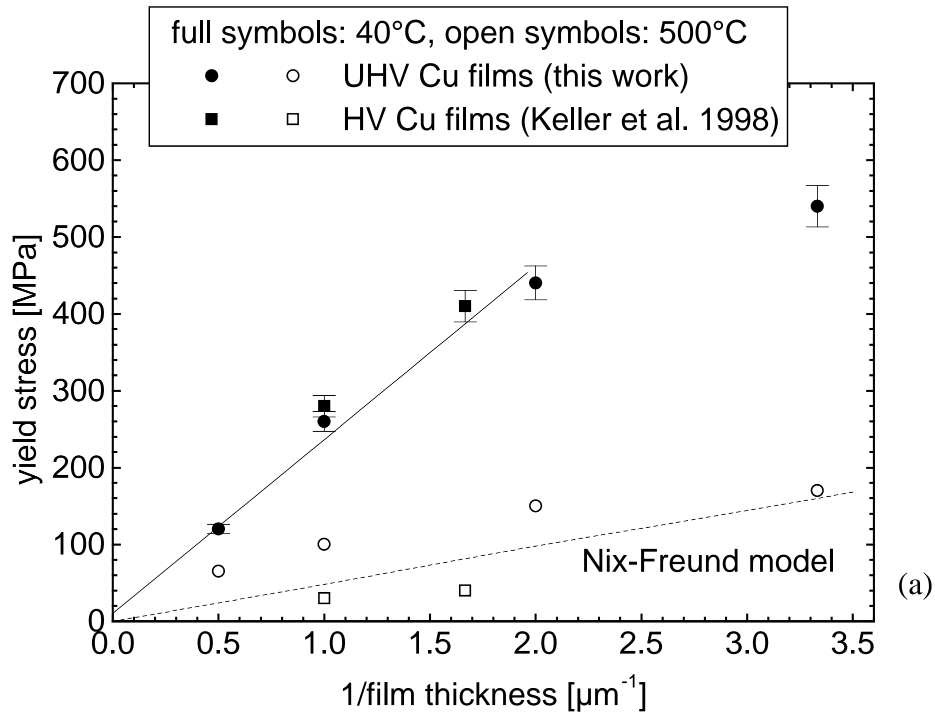

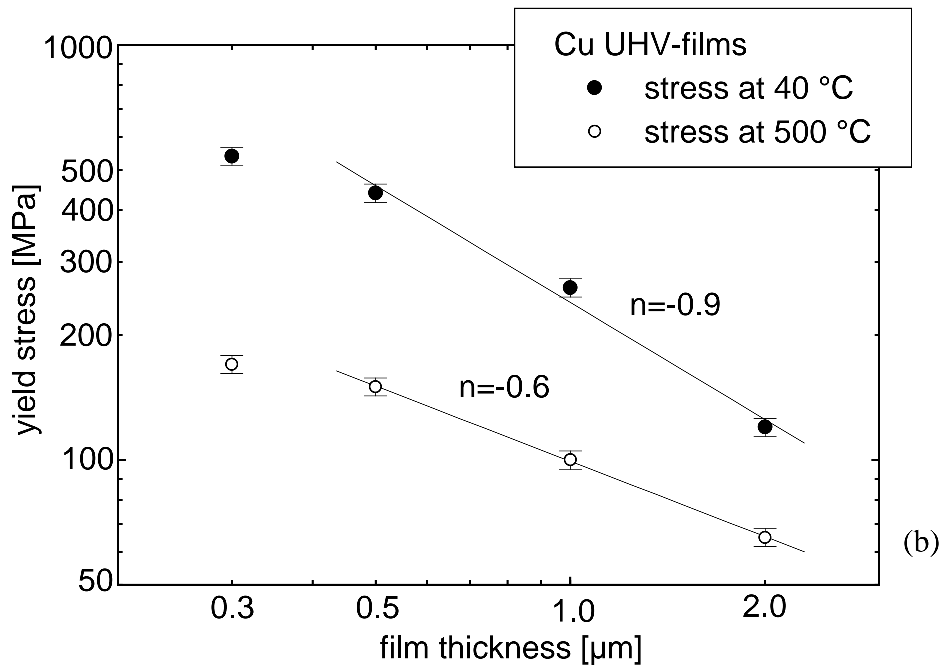

Figure 5-18 (a) Yield stress for Cu films at two different temperatures versus the inverse film thickness. The yield stress predicted by the Nix model, equation (2-8) is shown as the dashed line. (b) The yield stress for the UHV Cu films from (a) are plotted on a double-logarithmic scale. The thickness dependence of yield stress is weaker at 500 °C.

Nanohardness measurements

Film hardness data for annealed pure Cu films were shown in Figure 4-14 and Figure 4-17. Both absolute hardness values and the hardening, i.e. the slope of the curves, increased with decreasing film thickness. Thus, the same trend is observed as for the yield stress in Figure 5-18, which also increases with decreasing film thickness. If the hardness data are plotted versus the normalized indentation depth as shown in Figure 5-19, the slope of all curves becomes equal, as

$$\frac{\mathrm{d}H}{\mathrm{d}h} \approx \frac{1.5\ \text{GPa}}{t_f\ [\mu\text{m}]},$$

where h is the indentation depth. The self-similarity of the hardness versus normalized indentation depth curves in Figure 5-19 is explained by the spreading of the plastic zone under the indenter tip, characterized by a high degree of plastic deformation. A rule of thumb states that the plastic zone radius is about five times the indentation depth, as shown in the inserted schematic in Figure 5-19. Laursen and Simo (1992) showed with finite element modeling that during the indentation of a compliant thin film (Al) on a stiff substrate (Si) the hardness gradually increases from the film hardness to the hardness of the substrate as soon as the plastic zone has reached the substrate.

The absolute film hardness, H, can be defined by extrapolating the curves in Figure 5-19 to zero indentation depth. The film hardness thus defined increases from 0.9 GPa for the 2 μm thick film to 1.5 GPa for the 0.5 μm thick film. Interestingly, the thickness dependency of the yield stress of Cu films measured with the wafer curvature technique was much stronger: the yield stress of the 2.0 μm thick film was approximately 4 times smaller than that of the 0.5 μm thick film (Figure 5-18 a). This is an apparent contradiction to the common rule that hardness and yield stress of a material are proportional as (Tabor 1951)

$$H \approx 3\sigma_y. \tag{5-13}$$

It is concluded that the absolute film hardness is a quantity which cannot be defined properly. The physical reason for this is the limitation of the plastic zone with a high degree of plastic strain to a small volume around the indenter tip. This is in contrast to the plastic deformation under thermal stress in a wafer curvature experiment, which involves the total

film volume such that dislocation glide mechanisms are influenced by the entire film volume.

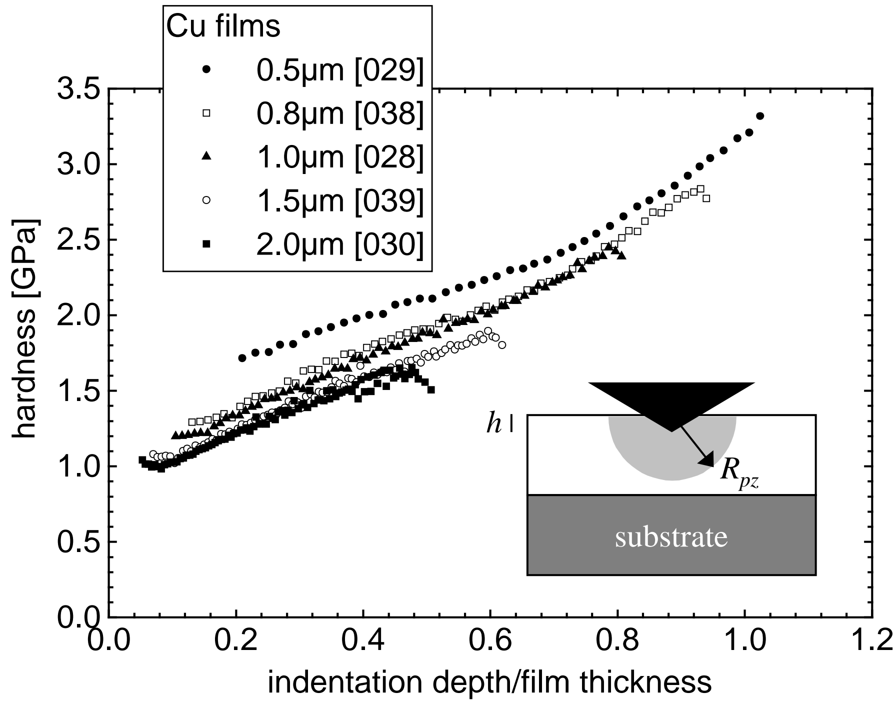

Figure 5-19 Hardness versus normalized indentation depths for annealed pure Cu films, replotted from Figure 4-17. The inserted schematic shows the spreading of the plastic zone with radius R_{pz} underneath the indenter tip. According to a rule of thumb, $R_{pz} \approx 5\,h$, where h is the indentation depth.

5.3.2 Isothermal stress relaxation experiments

One important parameter of the thermally activated glide of dislocations is the activation volume,

$$v^{*} = \frac{\Delta F}{\hat{\tau}}, \tag{5-14}$$

where ΔF is the activation energy and $\hat{\tau}$ is the critical stress defined in equation (2-11). The activation volume is interpreted as the average volume of dislocation structure involved in the activation process (Dieter 1988, p. 313); it can thus be written as

$$v^* = by^* \lambda^*, \tag{5-15}$$

where b is the Burgers vector, y^* is the activation distance which is related to the obstacle size, and λ^* is the length of the pinned dislocation segment.

In this work, activation volumes were determined as a function of temperature from isothermal stress relaxation experiments with the wafer curvature method for 1µm-thick pure Cu (Figure 4-16) and Cu-5at.%Al films (Figure 4-40). The data were analyzed in the following way: During an isothermal creep experiment, thermal stress is constant and elastic strain is gradually converted to plastic strain. The derivation of the total film strain balance, equation (2-3), with respect to time becomes thus

$$\frac{1}{M_f}\left(\frac{\partial \sigma}{\partial t}\right)_T + \dot{\varepsilon}_0 \exp\left(-\frac{\Delta F - s\sigma v^*}{k_B T}\right) = 0, \tag{5-16}$$

where equations (2-4), (2-11), and (5-14) have been considered. For determination of the activation volume, an algebraic conversion of this equation is used as

$$\frac{k_B T}{s} \ln\left(-\frac{\partial \sigma}{\partial t}\right)_T = A + v^* \sigma, \tag{5-17a}$$

with

$$A = \frac{k_B T \ln\left(M_f \dot{\varepsilon}_0\right) - \Delta F}{s}. \tag{5-17b}$$

A more accurate evaluation (see e.g. Dieter 1988, p. 311) would only consider the effective stress,

$$\sigma^* = \sigma - \sigma_\mu. \tag{5-18}$$

In this equation, σ_μ is the athermal yield stress component, which is the amount of stress that cannot be relaxed by thermally activated dislocation glide. However, this transforma-

tion only affects the parameter A, but not the parameter v^* in equation (5-17a), if a stress-independent value for σ_μ is assumed. As a simplification, σ_μ was neglected in the evalu a-tion.

The results for of 1 μm thick pure Cu and Cu-5at.%Al films are shown in Figure 5-20 and in Table 5-3 and are discussed in the following.

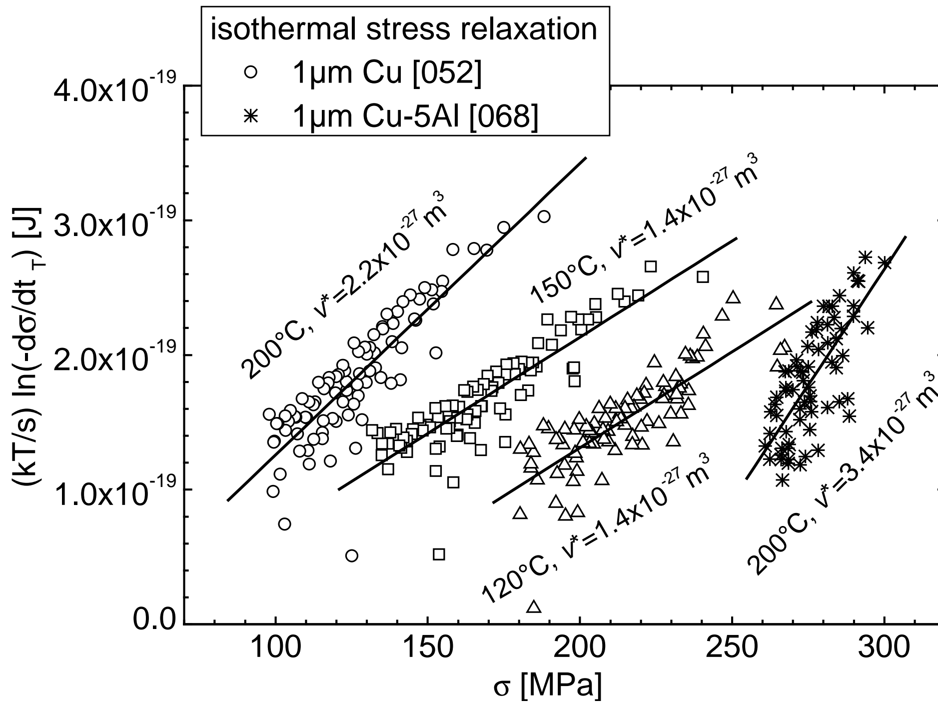

Figure 5-20 Isothermal stress relaxation data from Figure 4-16 and Figure 4-40. The slope of the curves is equal to the activation volume, v^*, according to equation (5-17a).

Activation volumes v^*

	120 °C	150 °C	200 °C
1 μm Cu	1.4×10^{-27} (83)	1.4×10^{-27} (83)	2.2×10^{-27} (131)
1 μm Cu-5at.%Al	-	-	3.4×10^{-27} (203)

Table 5-3 Activation volumes in m^3 determined from the slope of the curves in Figure 5-20. The error of v^* is ±10%. The number in brackets denotes the activation volume in units of b^3, where b is the length of the Burgers vector of Cu, $b = 2.56\times10^{-10}$ m.

The first observation from these data is that measured values for v^* in Table 5-3 are in the same range as the value used for the curve simulation in Figure 5-5,

$$v^* = \frac{3.5\times10^{-19}\ \text{J}}{240\ \text{MPa}} \approx 1.5\times10^{-27}\ \text{m}^3 .$$

From this value, the length of a pinned dislocation segment, λ^*, can be estimated using the geometrical interpretation of the activation volume, equation (5-15); setting obstacle size $y^* = b$, where b is the Burgers vector, one obtains as an upper limit

$$\lambda^* \approx v^*/b^2 = 1.5\times10^{-27}\ \text{m}^3 / \left(2.56\times10^{-10}\ \text{m}\right)^2 = 23\ \text{nm} .$$

This value is two orders of magnitude smaller than the characteristic dimensions of the film, film thickness and grain size. Obviously, this result is in conflict with current models based on energy-balance arguments such as the Nix model, in which plastic yielding is ac-complished by threading dislocation segments with lengths of the order of the film thick-ness (see section 2.2.2). Another observation is that the activation volume for the alloy film at 200 °C is 1.5 times larger than that of the pure Cu film. This effect is not understood.

The measured activation volumes in the thin films are significantly smaller than the activation volumes reported for Cu single crystals. Zeyfang et al. (1974), who investigated thermally activated glide in high-purity Cu single crystals, report values for v^* in the range of 0.1 to 10 $\times10^{-24}$ m^3, depending on strain rate and temperature. These values are more than two orders of magnitude larger than for the films. Thus, the average dislocation length involved in the activation process in single crystals is significantly larger than in the thin films.

Very small activation volumes are reported throughout the literature on fcc metal thin films, both for films on Si substrates and free-standing films. Kobrinsky and Thompson (1999) measured activation volumes in polycrystalline Ag films on Si substrates. The val-ues were in the range of $v^* = 1.0$ to 3.5×10^{-27} m^3 for 250 nm and 860 nm thick films in the temperature range between 25 and 100 °C. As in the present work, activation volumes de-creased with decreasing temperature. Interestingly, the dependency of v^* on the film thick-ness was only small, which is another contradiction to the models based on energy-balance arguments. However, it is noted that more measurements are needed to evaluate the film thickness effect on activation volume more exactly.

The creep of free-standing Cu thin films was investigated by several authors. The activation volumes of these films were in the same range as those found in this work. The value reported by Brotzen et al. (1990) for a 1 µm-thick free-standing Cu film at 90 °C was $v^* = 6.04\times10^{-27}$ m^3. Solonovich (1975) obtained values in the range of $v^* = 10^{-26}$ to 10^{-27} m^3 in a stress range around 300 MPa. The films, which were tested with a membrane-bulge technique, were only 80 nm thick. Il'inskiy et al. (1974) found activation volumes in the range of $v^* = 1$ to 4×10^{-26} m^3 for 25 µm thick evaporated films.

It is concluded from the similarity of the data from films on substrates and free-standing films that the activation volumes in thin films reflect intrinsic film properties, i.e. the dislocation glide mechanisms responsible for plastic film deformation are not influenced by the film/substrate interface as assumed in the Nix model.

As one possible explanation for the small values for v^*, work hardening was suggested (Kobrinsky and Thompson 1999). The dislocation density, ρ, which would be required to obtain a pinning distance in the range of λ^* can be roughly estimated using the equation,

$$\rho \approx \frac{1}{\lambda^{*2}}. \qquad (5\text{-}19)$$

With this equation, the dislocation density associated with a pinning distance of 23 nm is calculated as

$$\rho \approx \frac{1}{(23\ \mathrm{nm})^2} = 1.9\times10^{15}\ \mathrm{m}^{-2}.$$

Dehm and Arzt (1999) reported dislocation densities of $\rho \approx 3\times10^{13}\ \mathrm{m}^{-2}$ in a 0.5 µm thick unpassivated Cu film, which is two orders of magnitude below this value. This dislocation density was determined in TEM studies. Keller et al. (1998) reported on somewhat higher dislocation densities of approximately $\rho \approx 4\times10^{14}\ \mathrm{m}^{-2}$ in a 1 µm thick unpassivated Cu film, which is still one order of magnitude below the estimated value. These values were determined from the broadening of X-ray peaks. Using the same method, Hommel (1999) estimated the dislocation density of Cu films on Capton substrates to $\rho \approx 2\times10^{15}\ \mathrm{m}^{-2}$, which is the same value as estimated from the activation volumes in the present work. The

films had a grain size of 1 µm and had been plastically deformed by 0.5%. The degree of deformation was of the same order as for the thermally cycled films in this work (see Figure 5-17). It is followed that the scattering of the values for dislocation density in the literature indicates little reliability of the data currently available. Thus, the work hardening argument cannot be supported without doubt. Moreover, work hardening cannot account for the thickness dependency of yield stress in thin films because the activation volumes seem to depend only weakly on film thickness. However, more experimental work is re-quired for the study of thermally activated glide as a function of film thickness.

To conclude, very small activation volumes in a 1 µm thick Cu film were measured. The magnitude of the activation volumes suggest dislocation pinning between obstacles only a few 10 nm apart, which is in conflict with current models for the film thickness effect on yield stress. The variation of the activation volumes with film thickness as reported in the literature is only small. Free-standing films are reported to have similar activation volumes as films on substrates. Based on these observations, a new explanation for the film thick-ness effect on yield stress based on a dislocation source argument is proposed in the fol-lowing section.

5.3.3 The role of dislocation sources for the yield stress of thin films

In this section, a new model for the yield stress of thin films is proposed. It accounts both for the thickness dependency of the yield stress and for the small, thickness-independent activation volumes for thermally activated dislocation glide in thin films. In contrast to the energy-balance based models presented in section 2.2.2, film stress is considered as source controlled and not as glide controlled. It is claimed that dislocation *generation* and not the surpassing of obstacles is responsible for the small activation volumes observed in thin films. This assumption is based on recent TEM work by Dehm and Arzt (1999). The authors, who investigated a 0.5 µm thick Cu film on a Si substrate from the present work, observed dislocation emission from Frank-Read type dislocation sources upon in-situ thermal cycling. The extension of the sources was much smaller than film thickness. Dis-location loops were seen to expand until the dislocation vanished at the film/substrate in-terface.

In the following, an equation for the plastic deformation in a thin film under dislocation source control is derived. The equation is based on a modification of the Orowan-Taylor equation for the macroscopic plastic shear strain,

$$\gamma_{plastic} = \rho \, b \, \bar{x} \, , \tag{5-20}$$

where ρ is the mobile dislocation density, b is the Burgers vector and $\bar{x}$ is the average distance over which a dislocation moves during deformation. This equation, which is illustrated in Figure 5-21 (a), is valid for a constant value for ρ, and a value for $\bar{x}$ which is usually much smaller than the macroscopic dimension of the sample. $\bar{x}$ is limited by the distribution and the strength of obstacles on the glide planes.

For the plastic deformation of a thin film under source control (Figure 5-21 b), this equation must be modified. It is assumed that the maximum distance over which a dislocation can move during deformation is given by the film thickness. Thus, equation (5-20) is rewritten as

$$\gamma_{plastic} = \tilde{\rho} \, b \, t_f \, . \tag{5-21a}$$

In this equation, ρ was replaced by an effective mobile dislocation density taking into account dislocation generation,

$$\tilde{\rho} = \rho_{source} \, N \, \bar{l} \, , \tag{5-21b}$$

where ρ_{source} is the dislocation source density, N is the average number of emissions of one source during plastic deformation, and $\bar{l}$ is the average dislocation length in one loop, which can be set $\bar{l} \approx t_f$. For further evaluation of this equation, ρ_{source} is assumed to be independent of film thickness.

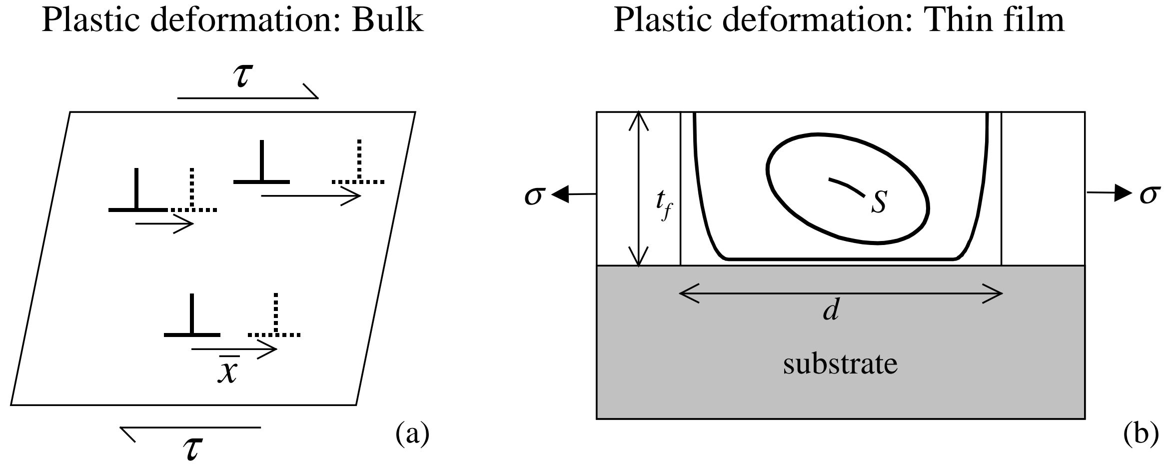

Figure 5-21 Plastic deformation by dislocation glide: (a) bulk behavior (glide controlled) versus (b) thin film behavior (source controlled). *S* is a Frank-Read type dislocation source.

The film stress at the end of the cooling cycle in a wafer curvature experiment, defined as the room temperature yield stress of a film, can be written as

$$\sigma_y = \sigma_{500°C} + M_f \left(\left| \varepsilon_{thermal} \right| - \varepsilon_{plastic} \right), \qquad (5\text{-}22)$$

where equations (2-3) and (2-4) were used. This equation is illustrated in the inserted schematic in Figure 5-22 (a). Note that $\varepsilon_{thermal} < 0$ (equation (2-2)), which is why $\left|\varepsilon_{thermal}\right|$ was used. Inserting equation (5-21) into equation (5-22) gives the equation

$$\sigma_y(t_f) = \sigma_{500°C} + M_f \left(\left| \varepsilon_{thermal} \right| - \frac{1}{s} \rho_{source} \, N \, b \, t_f^{\,2} \right), \qquad (5\text{-}23)$$

where *s* is the Schmid factor. The average number of dislocation loop emissions, *N*, is expected to be dependent on film stress, and therefore implicitly also on film thickness. However, this dependency is not known. For an evaluation of the experimental data, power-law behavior of *N* was assumed, as

$$N = n \, t_f^{\,c}, \qquad (5\text{-}24)$$

where n and c are fit parameters. Inserting equation (5-24) into equation (5-23) yields

$$\left[\sigma_y - \sigma_{500^\circ C}\right]\left(t_f\right) = M_f\left(\left|\varepsilon_{thermal}\right| - \frac{1}{s}\rho_{source}\ b\ n\ t_f^{\ c+2}\right). \qquad (5\text{-}25)$$

Equation (5-25) was fitted to the yield stress data for the Cu films from Figure 5-18. The result is shown in Figure 5-22 (a). For the evaluation, a dislocation source density of 1/µm^3 was assumed. Furthermore, the data for Cu given in the figure caption were used. The resulting thickness dependency of N is plotted in Figure 5-22 (b). An increasing number of emissions with increasing film stress is considered as a reasonable result. The average number of emissions increases from only 1.5 for a 2 µm thick film to 17 for a 0.5 µm thick film. It is assumed that in the range between 1 and 2 µm, plastic behavior would become glide controlled. Thus, thicker films would assume bulk behavior. For very thin films, on the other hand, the high number of emissions would lead to the inhibition of the source due to large back stresses of the dislocations piled up at grain boundaries. Computer simulations based upon discrete dislocation dynamics are currently carried out for a better understanding of these effects (von Blanckenhagen 2000).

To summarize, a new model for the thickness effect on yield stress of thin films was presented. In this model, the role of dislocation source emission for the film thickness effect on yield stress is described. Short dislocation displacements and a small effective dislocation density, which both scale with film thickness, reduce the effectiveness of dislocation sources. The small activation volumes in thin films are connected with the thermal activation of dislocation generation and not with the surpassing of obstacles. Several issues are, however, not understood. It is not clear why only dislocation sources as small as suggested by the activation volumes should be active in thin films; von Blanckenhagen (2000) has recently shown that sources as large as one third of the film thickness would be favored. Furthermore, work hardening was not assumed in the model. TEM observations by Dehm and Arzt (1999) showed that at low temperature dislocation pinning becomes an important process. Work hardening must be added in a more realistic model. Further work is proposed for a direct experimental evaluation of model parameters such as source density and source activity.

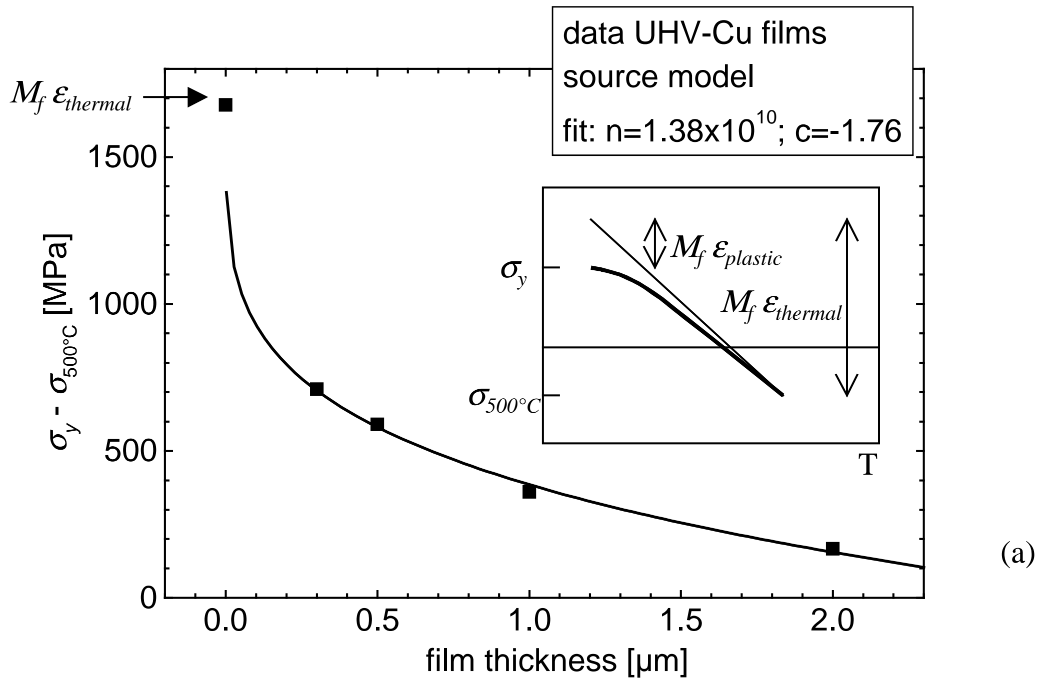

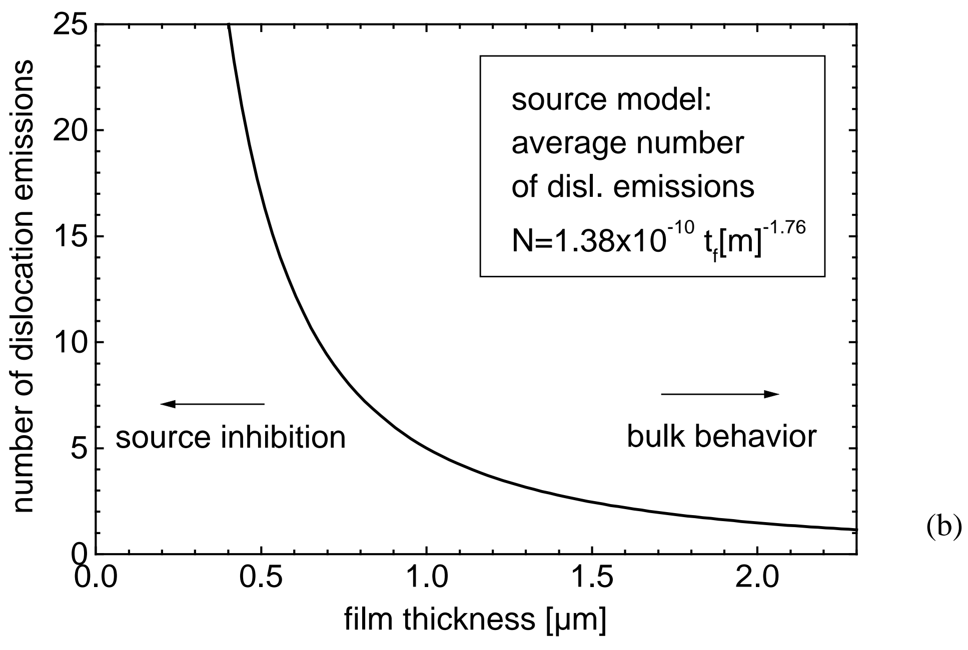

Figure 5-22 (a) Fit of the data from Figure 5-18 to the equation (5-25). For the evaluation of the fit, the following data for Cu were used: b = 2.56 Å, $M_f\left|\varepsilon_{thermal}\right|$ = 3.65 MPa K^{-1} $\times$ 460 K (Appendix A), and s = 0.27. The source density was set to ρ_{source} = 1/µm^3. (b) Plot of the resulting function for N according to equation (5-25).

5.4 Grain boundary voids in oxidized Cu-Al alloy films

Cu-Al alloy thin films which were oxidized at temperatures above 500 °C exhibited voids at grain boundaries and grain boundary triple junctions (Figure 4-19 to Figure 4-23). This is the first time that such a phenomenon has been observed in a two-dimensional grain structure. The morphology of the film surfaces was reminiscent of cross-sections of bulk samples that had undergone creep voiding (see section 2.3.1). It is claimed that the voids observed in the thin films are creep voids, too. A growth mechanism as schematically shown in Figure 5-23 is suggested: During high temperature oxidation of Cu-Al alloy films, Al segregated at the film surface and oxidized (see Auger depth profile in Figure 4-29). Stress-temperature curves of Cu-Al films showed evidence for the suppression of constrained diffusional creep, which was explained as a result of the suppression of surface diffusion in these films (section 5.2.1). After oxidation, the alloy films cooled down in the UHV-deposition chamber, during which a tensile film stress developed. This stress could be measured only ex-situ in the wafer curvature apparatus (Figure 4-34); however, the stress was expected to be similar in UHV. Void growth is claimed to be driven by the te n-sile stress acting upon the grain boundaries. Similar to the case of constrained diffusional creep (Figure 5-7), atomic diffusion into the boundary leads to the relaxation of grain boundary stress. However, no surface atoms as in the case of pure Cu films, but atoms from the void surface are plated into the boundary. The intersection of grain boundary and surface oxide is claimed to be an easy-nucleation site for voiding. In this section, the void size, the plastic strain associated with the voids, void morphology, and the local texture of voided grain boundaries is discussed.

Void size

The volume of one void is estimated using equation (2-17) for the volumetric growth rate of a spherical void located at a grain boundary in a bulk material. As an approximation, thermoelastic stress evolution during cooling is assumed, as

$$\sigma_n(T) = -M_f \Delta\alpha (T - T_{\max}).$$

The total void volume, V, is obtained from integration of the growth rate from the annealing temperature of 600 °C to room temperature, according to

$$V = -\int_{873}^{300} \frac{dV}{dt}(T') \frac{dT}{\dot{T}} = 5.5\times10^{-19}\ \text{m}^3.$$

For the integration, the parameters from the caption of Figure 5-8 were applied. The grain boundary thickness times grain boundary diffusivity from Frost and Ashby (1982 p. 21), $\delta D_{gb} = 5\times10^{-15} \exp(-104\ \text{kJ mole}^{-1}/RT)\ \text{m}^3\text{s}^{-1}$ was used. Integration was carried out numerically with Mathematica4.0 software. The geometrical factor on the right hand side of equation (2-17) was approximated by 0.3, which fits to a large range of values for r_v and l_v. Taking into account a hemispherical void shape as shown in Figure 5-23, a void radius of $r_v \approx 600$ nm is calculated from $V = 5.5\times10^{-19}\ \text{m}^3$. This value is of the same order as $r_v \approx 200$ nm for voids located at grain boundaries and $r_v \approx 500$ nm for voids located at triple junctions, which can be seen in Figure 4-19.

It is concluded that realistic volumes for creep voids are estimated if a bulk model was applied. The use of a bulk model is justified because of the similarity of the voiding mechanisms in the bulk and in a thin film.

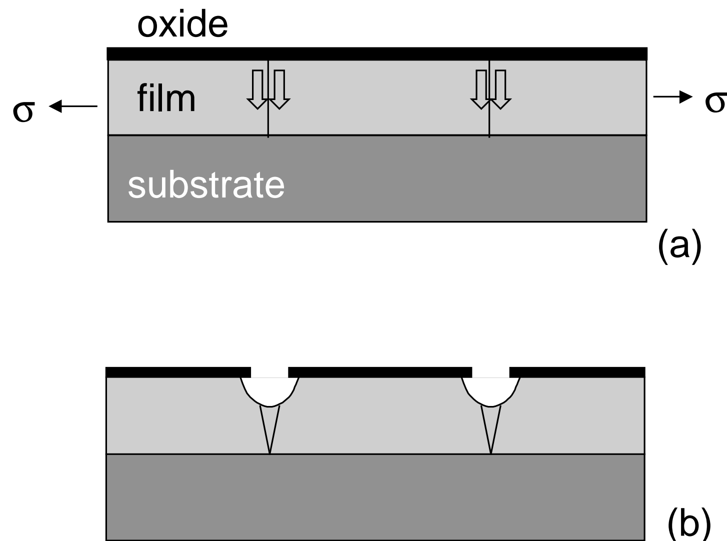

Figure 5-23 Model for the growth of grain boundary voids in a two-dimensional grain structure. Voids are nucleated at the intersection of grain boundaries under tensile stress with a surface oxide. Atoms from the void are transported by grain boundary diffusions into the boundary which leads to a relaxation of the grain boundary stress.

Total plastic strain

In the following, the plastic strain associated with the voids is discussed. It is assumed that all atoms from the voids were plated into the grain boundaries. Thus, the plastic strain associated with the voids, ε_{voids}, can be calculated from the equation,

$$\varepsilon_{voids} = \frac{1}{2}\frac{V_{voids}}{V_{film}} \quad , \tag{5-26}$$

where V_{voids} is the total void volume and V_{film} is the film volume of a specific region. The total void volume was evaluated from FIB micrographs using equation (3-3). The pre-factor ½ in equation (5-26) is explained by the two-dimensional strain in a film. Note that the same equation is used for the strain released due to hillock growth. Values for ε_{voids} for different films are presented in Table 5-4. Increasing plastic strain with decreasing Al-atomic fraction is observed. The films with numbers [108] to [110] were oxidized under identical conditions (see Appendix C for the detailed parameters). This effect has been so far not understood. A second observation is that the plastic strain decreases with decreasing oxidation temperature. This effect can be understood qualitatively: the grain boundary diffusivity decreases with decreasing temperature; the time during which the diffusivity is sufficiently high also decreases.

Plastic strain ε_{voids} for 1 µm thick oxidized Cu-Al films

film number	at.% Al	oxidation temp.	ε_{voids} / 10^{-3}
[108]	0.5	600 °C	2.2 ± 0.3
[109]	1.0	600 °C	1.5 ± 0.2
[110]	2.0	600 °C	1.3 ± 0.2
[102] [(a)]	1.0	600 °C	1.8 ± 0.3
[106]	1.0	500 °C	0.3 ± 0.1

Table 5-4 Strain relaxed by the voids, ε_{voids}, calculated with equation (5-26) for several 1 µm thick Cu-Al films. [(a)]The very large holes seen in Figure 4-22 were ignored for this calculation. This film had been annealed after oxidation for 6 h at 550 °C.

Void morphology

In Figure 5-24, two different types of grain boundary voids are shown. Voids in films which cooled down under UHV were equi-axed; voids at triple junctions were faceted, which is explained by the anisotropy of surface free energy. On the other hand, voids in the film oxidized and cooled down under inert gas in the wafer curvature apparatus were crack-like.

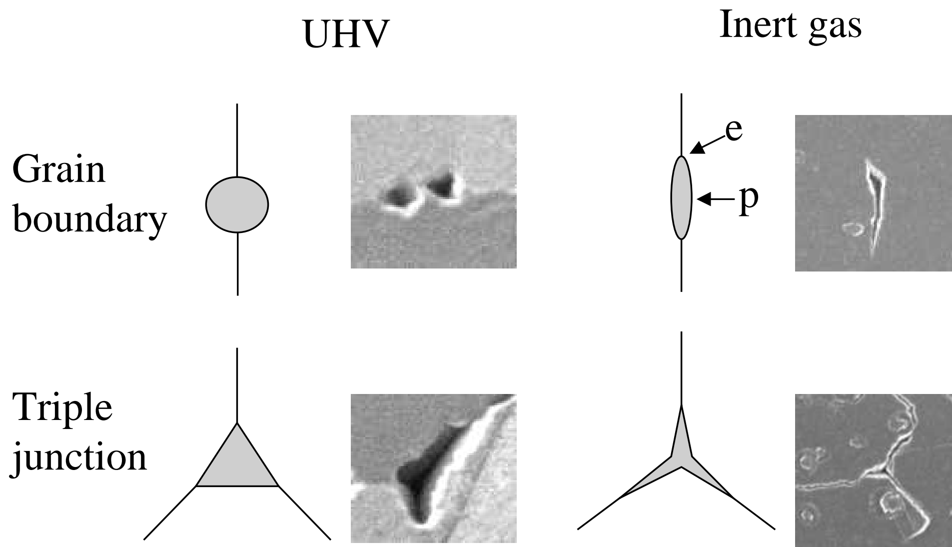

Figure 5-24 Schematic for the different void shapes found at grain boundaries and triple junctions in oxidized Cu-Al alloy films. Different shapes were found depending on the post-oxidation annealing conditions. Crack-like voids were found in the film oxidized and cooled down under inert gas in the wafer curvature apparatus. "e" and "p" denote equator and pole of the void (see text).

This effect is explained by the ratio of the rates of void-surface and grain boundary diffusion. Oxidation during thermal cycling in the wafer curvature apparatus is expected to decrease diffusivity on the void surface. A similar effect is known from creep voids in bulk metals, where both types of shape are observed as well. It was found that spherical voids are formed if grain boundary diffusion is rate limiting, while crack-like voids grow if surface diffusion is rate limiting (Cocks and Ashby 1982). In the case of high surface diffusivity, atoms are rapidly redistributed within the void such that the void surface remains spherical. This surface is associated with the smallest surface to volume ratio and is therefore energetically preferred. If, on the other hand, surface diffusion is rate limiting, the void becomes flatter and more crack-like, until the curvature difference at the void surface

between the "pole" (p) and the "equator" (e) is sufficient to drive a surface flux matching the atomic flux from the void into the grain boundary (see schematic in Figure 5-24): the radius of curvature, R, at the equator is smaller than the radius of curvature at the equator, which, according to equation (2-16), is associated with a lower chemical potential, f, at the equator.

Note that two different surface diffusivities were discussed in the context of void *growth* and void *shape*: the former was provoked by the suppression of diffusion on the *film* surface, while the latter was determined by diffusion on the *void* surface.

Local texture at grain boundaries

Grain boundary voids in the oxidized Cu-Al films were only found at high-angle bounda-ries with tilt angles >15°. Low angle boundaries and twin boundaries were not voided. This is seen in Figure 4-28, in which a FIB micrograph of a specific film area is compared with a grain boundary orientation map. It is argued that the more highly ordered low angle and twin boundaries have a smaller grain boundary energy and, thus, lower diffusivity. A similar observation was reported by Nucci et al. (1997), who studied stress voiding in pas-sivated copper lines. The authors found voids only at grain boundaries with higher misori-entation angles. This was considered by the authors as indirect evidence for increased dif-fusivity at these boundaries.

It is concluded that voiding occurred at grain boundaries in oxidized Cu-Al alloy thin films as a result of the tensile stress which develops in a film after annealing in combination with the suppression of surface diffusion due an aluminum-oxide segregation layer. This result emphasizes the importance of the fact that the heat treatment of metal thin films on Si sub-strates is always associated with stresses in the film.

6 Summary and conclusions

The high mechanical stresses found in metal thin films represent a serious reliability issue in modern semiconductor industry. Many layers of structured thin metal films are nowadays integrated in a computer chip where they interconnect the tens of millions of transistors. The recent trend towards the miniaturization of devices for mechanical, chemical, and biological application will call for new thin film materials with further improved performance, which is why research on alloying effects in small dimensions will become important.

In this work pure Cu and dilute Cu-Al alloy films in the thickness range of 0.3 to 2.0 µm were deposited by magnetron-sputtering on diffusion-barrier coated Si substrates. For the first time, such films were sputtered and annealed under ultra high vacuum (UHV) conditions. In-situ substrate cleaning by Ar ion bombardment was carried out before film deposition to ensure a good interface quality. Several films were oxidized under controlled conditions. Furthermore, Cu-1at.%Y films were sputtered and annealed under high vacuum (HV) conditions. The microstructure of the films was characterized primarily by focused ion beam microscopy. The thermo-mechanical properties of Cu and Cu-Al films were measured during thermal cycling with the wafer curvature method.

The aim of this research work was to characterize the predominant deformation mechanisms in pure Cu and Cu alloy films. A thermally stable second phase should be produced in the alloy films by selective oxidation of the alloying element. The specific role of the surface and of the film/substrate interface for film deformation was studied. The main results of this work are the following:

Film fabrication under UHV-conditions had a large effect on the microstructure evolution upon annealing. This research revealed for the first time that UHV-sputtered and annealed pure Cu films on in-situ ion-beam cleaned Si substrates had a large grain size between 2 and 3 times the film thickness, a very strong and sharp (111) texture, and a low twin density. This type of microstructure has so far not been observed for HV-sputtered Cu films in

the literature. It was accounted for by the high film purity and by a clean film/substrate interface. This result emphasizes the high sensitivity of the evolution of thin film microstructure to contamination resulting from the fabrication process.

One important aspect of this work was to what extent film microstructure evolution is affected by alloying. Microstructure evolution in the single-phase Cu-Al system and in the two-phase Cu-Y system was investigated. Comparison of an annealed 1 µm thick Cu-1at.%Al film, produced by magnetron co-sputtering under UHV-conditions, with a corresponding pure Cu film revealed no effect of the Al on grain size, texture, and twinning. This was accounted for by the solubility of Al in Cu. Grain growth in the two-phase Cu-Y system on the other hand was different from that observed in Cu and Cu-Al films. Normal grain growth was inhibited and abnormal grain growth was observed during annealing of Cu-Y films at temperatures above 600 °C.

One aim of this work, the *internal* oxidation of dilute Cu-Al alloy films, was not achieved: TEM investigation did not reveal particles; the nanohardness of oxidized alloy films was not increased compared to that of a pure Cu film. The failure of internal oxidation was attributed to the short diffusion lengths in a thin film. Al surface segregation and external oxidation led rather to a self-passivation of these films. This shows that alloying recipes, successfully applied in bulk metals, do not necessarily lead to the same result in the limited geometry of a thin film.

Stress-temperature curves were measured for pure Cu and for self-passivating Cu-Al films. The UHV-sputtered Cu films supported much higher stresses at high temperatures than the HV-sputtered Cu films known from literature. This effect was attributed to good film adhesion. The characteristic stress-temperature curve was modeled successfully using a recent mathematical solution for constrained diffusional creep in a thin polycrystalline film on a substrate (Figure 6-1). According to this model, the in-plane stress at the grain boundaries is relaxed at high temperatures by combined surface and grain boundary diffusion, giving rise to diffusion wedges at the grain boundaries. The intragranular stress is not relaxed by the creep mechanism due to the constraint of the substrate. Therefore, the average stress does not relax to zero at high temperatures. The significance of this result lies in the fact that it constitutes the first clear identification of diffusional creep in a thin film under the constraint of a substrate.

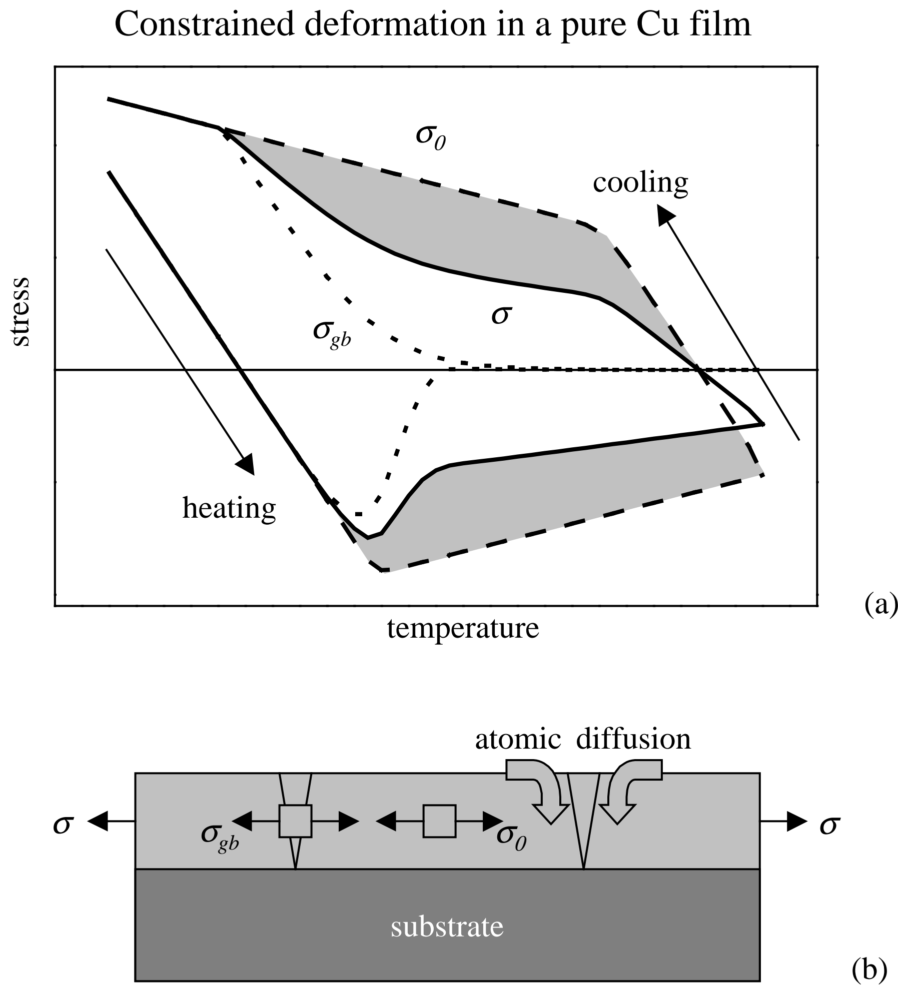

Figure 6-1 A central result of the present work: (a) Schematic picture of the stress evolution in a pure Cu film during thermal cycling. The plot shows the intragranular stress, σ_0, determined by dislocation glide, the average normal grain boundary traction, σ_{gb}, which is relaxed by constrained diffusional creep, and the average stress, σ. The shaded area between the σ_0 and the σ curve is equal to the average stress relaxed by diffusional creep. (b) Schematic of the constrained diffusional creep mechanism under tensile stress.

The characteristic features in the stress-temperature curves of pure Cu films, which were attributed to high-temperature stress relaxation by constrained diffusional creep, were not found in the corresponding curves of the self-passivating Cu-Al alloy films. This was explained by suppression of surface diffusion in these films, which was essential for diffusional creep. The stress-temperature curve of a Cu-Al film, which was similar to that of a pure Al film if stresses were normalized by the respective shear moduli, was modeled successfully by thermally activated dislocation glide. It was pointed out that Al films, which were studied in the literature, are de-facto passivated films due to the dense native oxide.

Cu-Al alloy films oxidized at temperatures above 500 °C exhibited voids at grain boundaries and grain boundary triple junctions. Voids were found only at high angle grain boundaries with high diffusivity. This effect was interpreted as creep voiding, which was observed for the first time in a two-dimensional grain structure. Void growth was explained by grain boundary diffusion under the tensile stress acting on the grain boundaries, which is built up upon cooling after oxidation. Suppression of surface diffusion by the dense and thermally stable aluminum-oxide surface layer was essential for this process: grain boundaries in an oxidized *pure* Cu film were not voided. This result shows that heat treatment of a film on a substrate is always connected to the generation of large stresses, which can lead even to deterioration of the film.

Finally, it was observed that the room-temperature yield stress of Cu films, measured in wafer curvature experiments, increased with decreasing film thickness. The values were in accordance with the yield stress of HV-sputtered Cu films from the literature. The magnitude of the yield stress was five times larger than that predicted by a current energy-balance based model (the Nix model). The small activation volumes for 1 μm thick Cu and Cu-Al films, measured during isothermal stress-relaxation experiments, suggested dislocation pinning with a pinning distance of only a few 10 nm. This was apparently a contradiction to the film-thickness dependency on yield stress. In a new approach to the thickness effect on the yield stress, it was suggested that the yield stress of thin films was dislocation source controlled rather than glide controlled.

The approach taken in this work could in future be supported by additional work in the following areas: X-ray micro-beam diffraction experiments may be employed to verify the inhomogeneous stress state resulting from constrained diffusional creep.

The stress-temperature curve of HV-sputtered Cu films from the literature, characterized by vanishing stresses at high temperature, could be described in this work only qualitatively. Interfacial sliding in the HV-sputtered films, for which indirect evidence was also found in a UHV-film sputtered without substrate cleaning, could be explained by contamination at the film/substrate interface. It is suggested to incorporate sliding at the film/substrate interface into a diffusional creep model for thin films.

Finally, extensive TEM work is needed to further study the action of dislocation sources in thin films upon thermal cycling. Important parameters such as the dislocation source density and the number of dislocation emissions from one source as a function of

film thickness are still needed for a quantitative evaluation of the source model presented in this work.

The results from this work emphasized the importance of interfacial phenomena both for the mechanical behavior of thin films and for alloying in small dimensions. Diffusional creep is constrained by the substrate which markedly improves film strength at high tem-perature. A second interface due to a film passivation further inhibits diffusional creep be-cause of the blocking of surface diffusion. In both cases, strong bonding at the interfaces is crucial for the effectiveness of the constraint. Plastic film deformation at low temperature is inhibited probably due to the confinement of the distance over which a dislocation can move by the small film dimensions. All three examples demonstrate that film strengthen-ing can be achieved without reinforcement of the film matrix. However, as creep voiding in the oxidized Cu-Al films showed, thermal stress generation must be considered if new alloying strategies are applied. It is concluded that future research in the field of alloying in small dimensions must focus on the tailoring of interface properties if specific mechanical film properties are to be achieved.

Literature

Adams, J. H., and authors. (1990). Metals handbook Vol. 2: Properties and selection - non-ferrous alloys and special-purpose materials, ASM International, Cleveland, Ohio.

Arzt, E. (1998). “Size effects in materials due to microstructural and dimensional constraints: a comparative review.” Acta Mater., 46(16), 5611-26.

Bader, S., Flinn, P. A., Arzt, E., and Nix, W. D. (1994). “Mechanical strength and microstructure of oxygen ion-implanted Al films.” J. Mater. Res., 9(2), 318-27.

von Blanckenhagen, B. (2000). unpublished results.

Brotzen, F. R. (1994). “Mechanical testing of thin films.” Internat. Mat. Rev., 39(1), 24-45.

Brotzen, F. R., Rosenmayer, C. T., Cofer, C. G., and Gale, R. J. (1990). “Creep of thin metallic films.” Vacuum, 41(4-6), 1287-90.

Chang, Y. A., and Himmel, L. (1966). “Temperature Dependence of the Elastic Constants of Cu, Ag, and Au above Room Temperature.” J. Appl. Phys., 37(9), 3567-72.

Cocks, A. C. F., and Ashby, M. F. (1982). “On creep fracture by void growth.” Progr. Mat. Sci., 27(3-4), 189-244.

Courtney, T. H. (1990). Mechanical behavior of materials, McGraw-Hill, New York.

Dehm, G., and Arzt, E. (1999). “In-situ transmission electron microscopy study of dislocations in a polycrystalline Cu thin film constrained by a substrate.” Appl. Phys. Lett., in press.

Diehl, J. (1956). “Zugverformung von Kupfer-Einkristallen.” Z. Metallk., 47(5), 331-43.

Dieter, G. E. (1988). Mechanical Metallurgy, McGraw-Hill, London.

Ding, P. J., Lanford, W. A., Hymes, S., and Murarka, S. P. (1994). “Effects of the addition of small amounts of Al to copper: Corrosion, resistivity, adhesion, morphology, and diffusion.” J. Appl. Phys., 75(1), 3627-31.

Ernst, F., Pirouz, P., and Heuer, A. H. (1991). "HRTEM study of a Cu/Al_2O_3 interface." Phil. Mag. A, 63(2), 259-77.

Flinn, P. A. (1991). "Measurement and interpretation of stress in copper films as a function of thermal history." J. Mater. Res., 6(7), 1498-501.

Flinn, P. A., Gardner, D. S., and Nix, W. D. (1987). "Measurement and interpretation of stress in aluminum-based metallization as a function of thermal history." IEEE Trans. Electr. Dev., ED-34(3), 689-99.

Fromm, E., and Gebhardt, E. (1976). "Gase und Kohlenstoff in Metallen." Reine und angewandte Metallkunde in Einzeldarstellungen, Springer, Berlin.

Frost, H. J., and Ashby, M. F. (1982). Deformation-mechanism maps, Pergamon Press, Oxford.

Gao, H. (1999). personal communication.

Gao, H., Zhang, L., Nix, W. D., Thompson, C. V., and Arzt, E. (1999). "Crack-like grain-boundary diffusion wedges in thin metal films." Acta Mater., 47(10), 2865-78.

Gibbs, G. B. (1966). "Diffusion Creep of a Thin Foil." Phil. Mag., 13, 589-93.

Gupta, J., Harper, J. M. E., Mauer, J. L., Blauner, P. G., and Smith, D. A. (1992). "Focused ion beam imaging of grain growth in copper thin films." Appl. Phys. Lett., 61(6), 663-5.

Haefer, R. A. (1987). Oberflächen- und Dünnschicht-Technologie, Springer, Berlin.

Haessner, F. (1978). "Recrystallization of Metallic Materials." , Riederer, Stuttgart.

Harper, J. M. E., Cabral Jr., C., Andricacos, P. C., Rice, P. M., Beyers, R. B., Locke, P. S., and Klepeis, S. J. (1999). "Mechanisms for Microstructure Evolution in electroplated Copper Thin Films." Polycrystalline Metal and Magnetic Thin Films, D. E. Laughlin, K. P. Rodbell, O. Thomas, and B. Zhang, eds., MRS Symp. Proc. Vol. 562, Pittsburgh, PA.

Harper, J. M. E., Gupta, J., Smith, D. A., Chang, J. W., Holloway, K. L., Cabral, C. J., Tracy, D. P., and Knorr, D. B. (1994). "Crystallographic texture change during abnormal grain growth in Cu-Co thin films." Appl. Phys. Lett., 65(2), 177-9.

Häussler, G., Daut, H. H., Schiller, S., Heisig, U., Goedicke, K., and Hempel, W. (1979). "Dispersion-strengthened copper-based materials formed by high rate magnetron/plasmatron sputtering." Thin Solid Films, 63(1), 131-6.

Hommel, M. (1999). "Röntgenographische Untersuchung des monotonen und zyklischen Verformungsverhaltens dünner Metallschichten auf Substraten," PhD dissertation, Universität Stuttgart.

Hull, D., and Rimmer, D. E. (1959). “The growth of grain-boundary voids under stress.” Phil. Mag., 4, 673-87.

Il'inskiy, A. I., Palatnik, L. S., Lakh, G. Y., and Nguen, T. A. (1974). “Thermal activation analysis of copper foils and films.” Fizika Metallov i Metallovedenie, 38(1), 217-19.

Jackson, M. S., and Li, C.-Y. (1982). “Stress relaxation and hillock growth in thin films.” Acta Met., 30(11), 1993-2000.

Joo, Y.-C., Müllner, P., Baker, S. P., and Arzt, E. (1997). “Mechanical properties of Al-Cu films with various heat treatments.” Materials Reliability in Microelectronics VII, J. J. Clement, R. R. Keller, K. S. Krisch, J. E. Sanchez Jr., and Z. Suo, eds., MRS Symp. Proc. Vol. 473, Philadelphia, PA, 409-14.

Keller, R.-M. (1996). “Thermomechanisches Verhalten und Mikrostruktur dünner, polykristalliner Kupferschichten,” PhD dissertation, Universität Stuttgart.

Keller, R.-M., Baker, S. P., and Arzt, E. (1998). “Quantitative analysis of strengthening mechanisms in thin Cu films: effects of film thickness, grain size, and passivation.” J. Mater. Res., 13(5), 1307-17.

Keller, R.-M., Baker, S. P., and Arzt, E. (1999). “Stress-temperature behaviour of unpassivated thin copper films.” Acta Mater., 47(2), 415-26.

Kirchner, S., Kraft, O., Baker, S. P., and Arzt, E. (1997). “Microstructure and mechanical properties of thin Al-Si-Ge films.” Thin Films: Stresses and Mechanical Properties VI, W. W. Gerberich, H. Gao, J.-E. Sundgren, and S. P. Baker, eds., MRS Symp. Proc. Vol. 436, Pittsburgh, PA, 21-6.

Kobrinsky, M. J., and Thompson, C. V. (1999). “Activation volume for inelastic deformation in polycrystalline Ag thin films.” accepted by Acta Mater.

Kupcis, O. A., Ramaswami, B., and Woo, O. T. (1973). “The effect of particle size on the yield stress of Cu-Al_2O_3 crystals.” Acta Met., 21(8), 1131-7.

Laursen, T. S., and Simo, J. C. (1992). “A study of the mechanics of microindentation using finite elements.” J. Mater. Res., 7(3), 618-26.

Lempenauer, K., and Arzt, E. (1992). “ODS alloys: abnormal grain growth in a temperature gradient.” Z. Metallk., 83(6), 423-8.

Leung, O., and Nix, W. D. (1999). unpublished results.

Longworth, H. P., and Thompson, C. V. (1991). “Abnormal grain growth in aluminum alloy thin films.” J. Appl. Phys., 69(7), 3929-40.

Majumder, K. S. (1977). “The structure-property relationships in evaporated thick films of alumina-dispersed copper.” Thin Solid Films, 42(3), 343-52.

Marieb, T. (1994). “Observations of void nucleation and growth in passivated metal lines,” PhD dissertation, Stanford University.

Massalski, T. B. (1990). “Binary Alloy Phase Diagrams.” , ASM International, Ohio.

Meijering, J. L. (1971). “Internal Oxidation in Alloys.” Advances in Materials Resarch, H. Herman, ed., Wiley, New York, 1-81.

Morrell, R. (1985). Handbook of properties of technical and engineering ceramics I, Her Majesty's Stationery Office, London.

Movchan, B. A., Demchishin, A. V., and Badilenko, G. F. (1977). “Effect of substrate temperature and amount of strengthening phase on density and mechanical properties of thick Ni-ZrO2 condensates.” Thin Solid Films, 40(1-3), 237-46.

Mullins, W. W. (1958). “The effect of thermal grooving on grain boundary motion.” Acta Met., 6, 414-27.

Nagorka, M. S., Levi, C. G., and Lucas, G. E. (1995). “Novel oxide-dispersion-strengthened copper alloys from rapidly solidified precursors: Part 1. Microstructural development.” Metall. & Mater. Trans. A, 26A(4), 859-71.

Neumann. (1990). Landolt-Börnstein New Series, H. Mehrer, ed., Springer, Berlin.

Nix, W. D. (1989). “Mechanical properties of thin films.” Metall. Trans. A, 20A(11), 2217-45.

Nix, W. D. (1998). “Yielding and strain hardening of thin metal films on substrates.” Scripta Mat., 39(4-5), 545-54.

Nucci, J. A., Keller, R. R., Field, D. P., and Shacham-Diamand, Y. (1997). “Grain boundary misorientation angles and stress-induced voiding in oxide passivated copper lines.” Appl. Phys. Lett., 70(10), 1242-4.

Ohring, M. (1992). The materials science of thin films, Academic Press, Boston.

Oliver, W. C., and Pharr, G. M. (1992). “An improved technique for determining hardness and elastic modulus using load and displacement sensing indentation experiments.” J. Mater. Res., 7(6), 1564-83.

Porter, D. A., and Easterling, K. E. (1992). Phase Transformations in Metals and Alloys, Chapman and Hall, London.

Riedel, H. (1987). Fracture at high temperatures, Springer, Berlin.

Riege, S. P., Thompson, C. V., and Frost, H. J. (1998). "The effect of particle-pinning on grain size distributions in 2D simulations of grain growth." Grain Growth in Polycrystalline Materials III, Proc. Third Int. Conf. Grain Growth ICGG-3, H. Weiland, B. L. Adams, and A. D. Rollett, eds., TMS - Miner. Metals & Mater. Soc., Warrendale, PA, 295-301.

Rösler, J., and Arzt, E. (1990). "A new model-based creep equation for dispersion strengthened materials." Acta Met., 38(4), 671-83.

Sautter, F. K. (1963). "Electrodeposition of Dispersion-Hardened Nickel-Al_2O_3 Alloys." J. Electrochem. Soc., 110(6), 557-60.

Solonovich, I. I. (1975). "Mechanism of creep of vacuum-deposited polycrystalline copper films in the temperature interval 20-150 degrees C." Fizika Metallov i Metallovedenie, 40(3), 633-7.

Stoney, G. G. (1909). "The Tension of Metallic Films deposited by Electrolysis." Proc. Roy. Soc., A82, 172-5.

Surholt, T., and Herzig, C. (1997). "Grain boundary self-diffusion in Cu polycrystals of different purity." Acta Mater., 45(9), 3817-23.

Suzuki, Y., Wajima, M., and Asai, O. (1986). "The characteristics of Ag-Al_2O_3 films electrodeposited from thiocyanate solutions." Trans. Jap. Inst. Met., 27(3), 215-22.

Tabor, D. (1951). The Hardness of Metals, Clarendon Press, Oxford.

Thompson, C. V. (1990). "Grain growth in thin films." Annual review of materials science, R. A. Huggins, J. A. Giordmaine, and J. B. Wachtman Jr., eds., Palo Alto, 245-68.

Thompson, C. V. (1993). "The yield stress of polycrystalline thin films." J. Mater. Res, 8(2), 237-8.

Thompson, C. V. (1994). "Grain growth in polycrystalline thin films." Polycrystalline Thin Films: Structure, Texture, Properties and Applications, K. Barmak, M. A. Parker, J. A. Floro, R. Sinclair, and D. A. Smith, eds., MRS Symp. Proc., Pittsburgh, PA, 3-12.

Thompson, C. V., and Carel, R. (1996). "Stress and grain growth in thin films." J. Mech. Phys. Solids, 44(5), 657-73.

Thornton, J. A. (1977). "High rate thick film growth." Ann. Rev. Mater. Sci., 7, 239-60.

Thouless, M. D. (1993). "Effect of surface diffusion on the creep of thin films and sintered arrays of particles." Acta Met., 41(4), 1057-64.

Thouless, M. D., Gupta, J., and Harper, J. M. E. (1993). “Stress development and relaxation in copper films during thermal cycling.” J. Mater. Res., 8(8), 1845-52.

Thouless, M. D., Rodbell, K. P., and Cabral, C. J. (1996). “Effect of a surface layer on the stress relaxation of thin films.” J. Vac. Sci. Tech. A, 14(4), 2454-61.

Venkatraman, R., and Bravman, J. C. (1992). “Separation of film thickness and grain boundary strengthening effects in Al thin films on Si.” J. Mater. Res., 7(8), 2040-8.

Vinci, R. P., Zielinski, E. M., and Bravman, J. C. (1995). “Thermal strain and stress in copper thin films.” Thin Solid Films, 262(1-2), 142-53.

Wagner, C. (1961). “Theorie der Alterung von Niederschlägen durch Umlösen.” Z. Elektrochem., 65(7/8), 581-91.

Xia, Z. C., and Hutchinson, J. W. (1999). “Crack patterns in thin films.” to be published.

Yang, J. C., Kolasa, A. B., Gibson, J. M., and Yeadon, M. (1998). “Self-limiting oxidation of copper.” Appl. Phys. Lett., 73(19), 2841-3.

Zener, C., quoted by Smith, C. S. (1949). Trans. TMS-AIME, 175, 15.

Zeyfang, R., Buck, O., and Seeger, A. (1974). "Thermally activated plastic deformation of high-purity copper single crystals." phys. stat. sol. (b), 61, 551-61.

Appendix

A: Thermoelastic data for Cu on Si

In this appendix, temperature-dependent elastic constants for Cu are tabulated in Table A-1. The temperature-dependent linear thermal expansion coefficients of Cu and Si as well as the thermoelastic slope for Cu films on Si are tabulated in Table A -2. In Figure A-1, normalized values for the differential thermal expansion coefficient for Cu and Si, the b i-axial modulus for a (111)-oriented Cu film, and the corresponding thermoelastic slope for a Cu film on a Si substrate are plotted versus temperature.

Elastic constants for Cu

T [K]	C_{11} [10^{11}Pa]	C_{12} [10^{11}Pa]	C_{44} [10^{10}Pa]	M_{111}[10^{11}Pa]	M_{100}[10^{11}Pa]
300	1.700	1.225	7.580	2.63	1.16
350	1.675	1.215	7.450	2.59	1.13
400	1.655	1.205	7.310	2.55	1.11
450	1.635	1.195	7.180	2.51	1.08
500	1.615	1.185	7.040	2.48	1.06
550	1.595	1.175	6.910	2.44	1.04
600	1.575	1.165	6.770	2.40	1.02
650	1.555	1.155	6.630	2.36	0.99
700	1.535	1.145	6.500	2.32	0.97
750	1.515	1.135	6.360	2.28	0.95
800	1.495	1.125	6.230	2.24	0.93

Table A-1 Elastic constants for Cu from Chang and Himmel (1966). The biaxial moduli, M_{111} and M_{100}, are defined in the equations (2-5) and (2-6).

Thermoelastic constants for Cu films

T [K]	α_{Cu} [10^{-5} K^{-1}]	α_{Si} [10^{-6} K^{-1}]	$\Delta\alpha$ [10^{-5} K^{-1}]	$M_{111}\Delta\alpha$ [MPaK^{-1}]	$M_{100}\Delta\alpha$ [MPaK^{-1}]
300	1.67	2.616	1.41	3.70	1.63
400	1.76	3.253	1.44	3.66	1.59
500	1.83	3.614	1.47	3.64	1.56
600	1.89	3.842	1.51	3.61	1.53
700	1.96	4.016	1.56	3.62	1.51
800	2.04	4.151	1.63	3.65	1.51
mean value:			*1.50*	*3.65*	*1.56*

Table A-2 Thermal expansion coefficients, α, and differential thermal expansion coefficient, $\Delta\alpha = \alpha_{Cu} - \alpha_{Si}$, from Adams et al. (1990) and thermoelastic slope for Cu in (111) and (100) orientation.

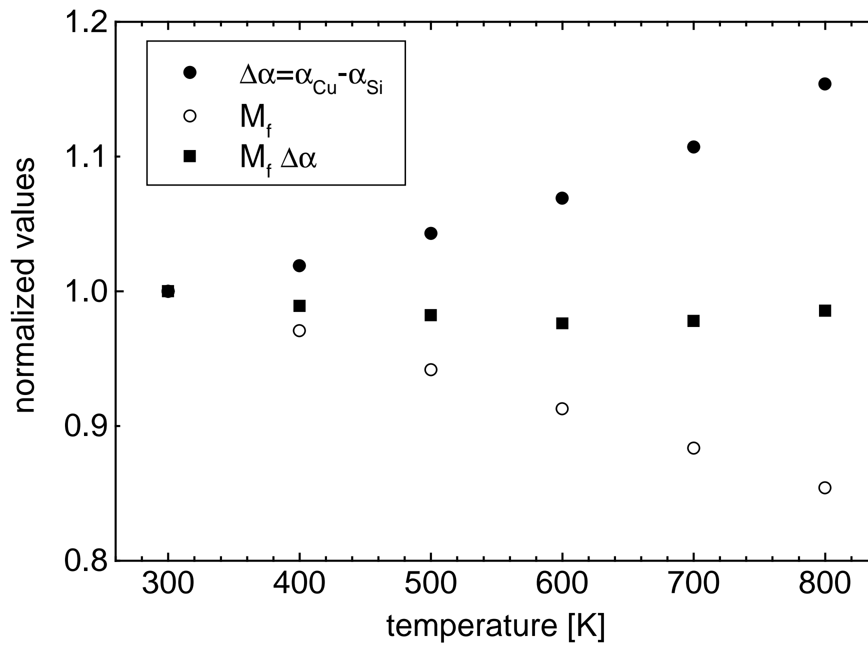

Figure A-1 Differential thermal expansion coefficient, $\Delta\alpha$, for Cu and Si, biaxial modulus for Cu in (111)-orientation, M_{111}, and thermoelastic slope, $M_{111}\Delta\alpha$. All values are normalized with respect to the value at 300 K.

B: Modeling constrained diffusional creep

In the following a detailed derivation of equation (5-10) is presented. It is shown how this equation is applied to model the evolution of the average normal grain boundary stress during a heating cycle in a wafer curvature experiment under the control of thermoelastic deformation. The code for the simulation of a thermal cycle under dislocation glide and constrained diffusional creep with Mathematica4.0 software is found at the end of Appendix B.

Derivation of equation (5-10)

Equation (5-5a) for the grain boundary traction under constrained diffusional creep is valid only for constant intragranular stress, σ_0, and constant temperature. For modeling the grain boundary stress evolution under thermal cycling, this equation must be changed (Gao 1999). First, the effect of a non-constant stress, σ_0, is considered. For this case, equation (5-5a) has to be written as

$$\sigma_{gb}(t) = \int_0^t \exp\left[-\lambda \frac{(t-\xi)}{t_0}\right] d\sigma_0(\xi) \quad . \tag{B-1}$$

In this equation, the exponential term acts as a Green's function describing the response of the grain boundary stress at time t to an increment in stress, $d\sigma_0(\xi)$, at the time $t = \xi$. However, in a wafer curvature experiment not only σ_0 but also temperature is time dependent. Thus, the Green's function in equation (B-1) is time dependent, which is why a second integration becomes necessary which leads to equation (5-10).

It is important to understand the role of $d\sigma_0$ in equation (5-10) if a thermal cycle is modeled. If the intragranular stress, σ_0, is subject to any relaxation mechanisms, two cases must be distinguished: if film stress is homogeneous (low temperatures), $d\sigma_0$ is described by the change in intragranular stress. However, if the grain boundary stress is relaxed, $d\sigma_0$ is described by the thermoelastic stress, for the grain boundary stress is *below* the yield stress. This was considered in the simulation of the cooling cycle in Figure 5-14 (see Mathematica4.0 code below).

Application of equation (5-10) for thermoelastic σ_0

A wafer curvature cycle can be modeled with constrained diffusional creep as the only stress relaxation mechanism (see Figure 5-10 to Figure 5-12). For such a case, $d\sigma_0$ in equation (5-10) is written as

$$d\sigma_0(t) = \left(\sigma_0^{start}\delta(t) - M_f \Delta\alpha\dot{T}\right)dt\,, \tag{B-2}$$

where σ_0^{start} is the stress at the beginning of the heating cycle, and $\delta(t)$ is Dirac's delta function. For the simulation, variables are changed from time to temperature, according to

$$dt = dT/\dot{T}\,. \tag{B-3}$$

The grain boundary traction during heating is obtained upon insertion of equation (B-2) into equation (5-10) under consideration of equation (B-3), as

$$\sigma_{gb}(T) = \sigma_0^{start}\exp\left[-\lambda\int_{Tstart}^{T}\frac{d\zeta}{\dot{T}t_0(\zeta)}\right] - M_f\Delta\alpha\dot{T}\int_{Tstart}^{T}\exp\left[-\frac{\lambda}{\dot{T}}\left\{\int_{\zeta}^{T}\frac{d\xi}{t_0(\xi)}\right\}\right]\frac{1}{\dot{T}}d\zeta\,. \tag{B-4}$$

The integrals were solved numerically with Mathematica4.0 software. In order to reduce the computing time, the integral

$$\int_A^B\frac{d\zeta}{t_0(\zeta)} \tag{B-5}$$

was tabulated as an interpolated function, $f(A, B)$, using 50 K temperature steps.

Mathematica4.0 code for the simulation of a stress-temperature curve under the control of thermally activated dislocation glide and constrained diffusional creep (Figure 5-14 a)

```
(* simulation of stress-temperature curve for 500 nm Cu on Si: thermally
activated dislocation glide and constrained diffusional creep (Gao's
model) - SI units *)



(* experimental parameters *)

Tstart = 293;     (* temperature range of thermal cycle *)
Tmax = 773;
Tdot = 0.1;       (* heating rate *)

tf = 500*10^-9;   (* film thickness *)
d = 4*10^-6;      (* grain size *)
M = 2.6*10^11;    (* biaxial modulus (111) - textured Cu *)
deltaalpha = 1.4*10^-5;
      (* differential thermal expansion coefficient Cu-Si *)

s  = 0.27  ;      (* Schmid factor for (111) - oriented grain *)


(* create intragranular stress curve *)

(* creep law: thermally activated dislocation glide, equation (2-11) *)

epsdot[sig_, T_] := Sign [sig]* epsdot0*
    Exp[-DeltaF/(k T) * (1 - s Abs[sig] / taubar)] ;

epsdot0 = 1*10^3;
DeltaF = 3*10^-19;
taubar = 180*10^6;

k = 1.38*10^-23;

(* solve differential equation heating cycle, equation (5-3) *)

NDSolve[{sig'[T] == - M deltaalpha - 1/Tdot * M * epsdot[sig[T], T],
    sig[Tstart] == 350*10^6}, sig, {T, Tstart, Tmax},
      Method -> RungeKutta ];

heatstress[T_] := Evaluate [sig[T] /. %] ;

(* solve differential equation, cooling cycle *)

NDSolve[{-sig'[T] == M deltaalpha - 1/Tdot * M * epsdot[sig[T], T],
    sig[Tmax] == Part[heatstress[Tmax], 1]}, sig, {T, Tmax, Tstart},
      Method -> RungeKutta];

coolstress[T_] := Evaluate [sig[T] /. %];

(* differentiate to obtain d-sigmanaught for creep law below *)

DTheatstress[T_] := Evaluate[D[Part[heatstress[T], 1], T]];
DTcoolstress[T_] := Evaluate[D[Part[coolstress[T], 1], T]];
```

```
(* calculate grain boundary stress under constrained diffusional creep *)

(* paramters required for Gao's model *)

tnaught[T_] := 4 Pi k T tf^3 / (Eb deltaDB[T] Omega); (* time constant
    for diffusion, equation (5-5b) *)

deltaDB[T_] := 5*10^-15 Exp[-90000 / R / T];
      (* grain boundary diffusivity *)

R = 8.314;
Omega = 1.18*10^-29;    (* atomic volume of Cu *)
Eb = ECu / (1 - nu^2);  (* plane strain elastic modulus Cu *)
ECu = 124*10^9;
nu = 0.34;
lambda = 8.1 + 30.65 tf/d;     (* geometry factor, equation (5-5c) *)

(* evaluate according to equation (B-5) *)
inttnaught =
    FunctionInterpolation[NIntegrate[1/tnaught[x], {x, T1, T2}],
        {T1, Tstart, Tmax, 50}, {T2, Tstart, Tmax, 50}];


(* heating cycle *)

(* define intragranular stress *)

sigmanaught[T_] := Part[heatstress[T], 1];     (* intragranular stress *)

(* calculate grain boundary traction, equation (5-10) *)

sigmagb[T_] :=
    sigmanaught[Tstart] Exp[-lambda/Tdot inttnaught[Tstart, T]] +
      NIntegrate[Exp[-lambda/Tdot inttnaught[Theta, T]]
        DTheatstress[Theta], {Theta, Tstart, T}];

(* calculate average stress, equation (5-6) *)

sigma[T_] := sigmanaught[T] - (sigmanaught[T] - sigmagb[T])
    *(4 tf/d Tanh[d/(4 tf)]);

(* plot all stress components for heating cycle *)

Plot[{sigma[T], sigmanaught[T], sigmagb[T]}, {T, Tstart, Tmax}]

(* make a table to export data for origin *)

Clear[stream];
stream = OpenWrite["sigmaheat.dat"];
Write[stream, Table[{T - 273, sigma[T]/10^6, sigmanaught[T]/10^6,
    sigmagb[T]/10^6}, {T, Tstart, Tmax, 10}]];
Close[stream]


(* cooling cycle *)

Tdot = -0.1;      (* cooling rate *)

sigmanaught[T_] := Part[coolstress[T], 1];     (* intragranular stress *)
```

```
(* calculate grain boundary traction, equation (5-10) *)

sigmagb[T_]:=
    Min[ NIntegrate[Exp[-lambda/Tdot inttnaught[Theta, T]]
      (-M deltaalpha ), {Theta, Tmax, T}], Abs[sigmanaught[T] ]];


(* calculate average stress, equation (5-6) *)

sigma[T_] := sigmanaught[T] - (sigmanaught[T] - sigmagb[T])
    *(4 tf/d Tanh[d/(4 tf)]);

(* plot all stress components for cooling cycle *)

Plot[{sigma[T], sigmanaught[T], sigmagb[T]}, {T, Tstart, Tmax}]

(* make a table to export data for origin *)

Clear[stream];
stream = OpenWrite["sigmacool.dat"];
Write[stream, Table[{T - 273, sigma[T]/10^6, sigmanaught[T]/10^6,
      sigmagb[T]/10^6}, {T, Tstart, Tmax, 10}]];
Close[stream]
```

C: List of Cu and Cu-Al films

In this appendix, details on the fabrication of all Cu and Cu-Al alloy films are listed.

Pure Cu films

Nr.	Thick.	Material	Annealing	Oxidation
[028]	1.0 µm	Cu	400 °C/1 h HV	-
[029]	0.5 µm	Cu	400 °C/1 h HV	-
[030]	2.0 µm	Cu	400 °C/1 h HV	-
[038]	0.8 µm	Cu	400 °C/1 h HV	-
[039]	1.5 µm	Cu	400 °C/1 h HV	-
[044]	1.0 µm	Cu	-	-
[052]	1.0 µm	Cu	500 °C sub. curv.	-
[091]	1.0 µm	Cu	600 °C/10 min UHV	-
[097]	1.0 µm	Cu	600 °C/10 min UHV	1 10^{-3} Pa/2 min/600 °C
[104]	1.0 µm	Cu	600 °C/10 min UHV	-
[111]	2.0 µm	Cu	600 °C/10 min UHV	-
[117]	1.0 µm	Cu *	600 °C/10 min UHV	-
[118]	2.0 µm	Cu	600 °C/10 min UHV	-
[119]	0.5 µm	Cu	600 °C/10 min UHV	-
[129]	0.3 µm	Cu	600 °C/10 min UHV	-

* sputtered without substrate cleaning

Cu-Al alloy films

Nr.	Thick.	Material	Annealing	Oxidation
[031]	1.0 µm	Cu-1at.%Al	400 °C/1 h HV	-
[033]	1.0 µm	Cu-2at.%Al	400 °C/1 h HV	-
[034]	1.0 µm	Cu-5at.%Al	400 °C/1 h HV	-
[068]	1.0 µm	Cu-5at.%Al	500 °C sub. curv.	-
[079]	1.0 µm	Cu-1at.%Al	500 °C sub. curv.	-
[081]	1.0 µm	Cu-1at.%Al	500 °C sub. curv.	1×10^{-5} Pa react. sputt.
[085]	1.0 µm	Cu-1at.%Al	500 °C sub. curv.	1×10^{-2} Pa react. sputt.
[086]	1.0 µm	Cu-1at.%Al	500 °C sub. curv.	1×10^{-3} Pa react. sputt.

[094]	1.0 µm	Cu-1at.%Al	600 °C/10 min UHV	1×10^{-3} Pa/10 s/600 °C
[095]	1.0 µm	Cu-1at.%Al	600 °C/10 min UHV	-
[096]	1.0 µm	Cu-1at.%Al	600 °C/10 min UHV	1×10^{-3} Pa/2 min/600 °C
[102]	1.0 µm	Cu-1at.%Al	500 °C/10 min UHV	1×10^{-5} Pa/30 min/500°C
[105]	1.0 µm	Cu-1at.%Al	600 °C/10 min UHV	1×10^{-5} Pa/6 h/400 °C
[106]	1.0 µm	Cu-1at.%Al	600 °C/10 min UHV	1×10^{-3} Pa/2 min/600 °C **
[108]	1.0 µm	Cu-.5at.%Al	600 °C/10 min UHV	1×10^{-4} Pa/7 min/600 °C
[109]	1.0 µm	Cu-1at.%Al	600 °C/10 min UHV	1×10^{-4} Pa/7 min/600 °C
[110]	1.0 µm	Cu-2at.%Al	600 °C/10 min UHV	1×10^{-4} Pa/7 min/600 °C
[116]	1.0 µm	Cu-1at.%Al	600 °C/10 min UHV	600 °C sub. curv.
[132]	0.5 µm	Cu-1at.%Al	600 °C/10 min UHV	-

** 6 h annealing at 550 °C after oxidation

D: List of symbols

A	grain area (m^2)
A_{gb}	geometrical constant
b	Burgers vector length (m)
C_{ij}	component of stiffness matrix (N/m^2)
c	fit parameter
c_B	concentration of element B
c_O	oxygen solubility
$D_{B,\,O}$	diffusivity of element B, oxygen (m^2/s)
d	grain size (m)
d_{50}	median grain size (m)
d_{max}	maximum grain size (m)
E_a	activation energy for grain boundary diffusion (J/mole)
E_f	Young's modulus of film material (N/m^2)
f	chemical potential (J)
	also: correction factor for effective grain size
	also: volume fraction of second phase
f_0	chemical potential inside a grain (J)
H	hardness (N/m^2)
h	indentation depth (m)
k_B	Boltzmann's constant (1.380658×10^{-23} J/K)
k_y	Hall-Petch constant ($N/m^{3/2}$)
L_p	mean particle distance (m)
$\bar{l}$	average dislocation length in a loop
l_v	half the distance between two voids (m)
M_f	biaxial film modulus (N/m^2)
M_s	biaxial substrate modulus (N/m^2)
N	number of source emissions during deformation
$N_{HA,\,LA,\,\Sigma3}$	number of high angle grain boundary, low angle grain boundary, and Σ3-twin boundary segments

n	fit parameter
	also: half the valency of cation
p	pressure (N/m^2)
p_n	pressure on grain boundary due to its curvature (N/m^2)
p_Z	pinning force on a grain boundary (N/m^2)
R	radius of grain boundary curvature (m)
	also: radius of substrate curvature (m)
	also: radius of surface curvature (m)
	also: universal gas constant (8.3145 J/K/mole)
R_S	sheet resistance (Ohms)
r_p	mean particle radius (m)
r_0	mean particle radius at time zero (m)
r_v	void radius (m)
s	Schmid factor
T	temperature (K)
T_0	temperature at which a film is free of thermal strain (K)
T_m	melting temperature (K)
T_{start}	starting temperature in thermal cycle
T_{th}	threshold temperature for abnormal grain growth (K)
$\dot{T}$	heating/cooling rate (K/s)
t	time (s)
t_0	time constant for constrained diffusional creep (s)
$t_{f,\ s,\ o}$	film, substrate, and oxide layer thickness (m)
V	void volume (m^3)
$V_{film,\ voids}$	total film volume, void volume (m^3)
V_m	molar volume of particle (m^3/mole)
v^*	activation volume (m^3)
$\bar{x}$	diffusion length (m)
	also: dislocation glide distance (m)
y^*	activation distance (m)

$\alpha_{f,\ s}$	linear thermal expansion coefficient of film, substrate (1/K)
$\beta_{f,\ o}$	constants of the order of unity
ΔF	activation energy for obstacle controlled dislocation glide (J)
ΔG^{0}	oxygen affinity (J/mole)
$\Delta\alpha$	differential thermal expansion coefficient (1/K)
δD_{gb}	grain boundary thickness times grain boundary diffusivity (m^3/s)
$\varepsilon_{elastic}$	elastic strain
$\varepsilon_{plastic}$	plastic strain
$\varepsilon_{thermal}$	thermal strain
ε_{voids}	plastic strain due to voids
$\dot{\varepsilon}_{plastic}$	plastic strain rate (s^{-1})
$\dot{\varepsilon}_0$	pre-exponential factor for obstacle controlled dislocation glide (s^{-1})
φ	angle between glide plane normal and film normal
$\gamma_{plastic}$	plastic shear strain
$\gamma_{s,\ i}$	surface, interfacial free energy (J/m^2)
λ	angle between Burgers vector and film normal
λ^*	length of the pinned dislocation segment (m)
μ	shear modulus (N/m^2)
$\mu_{f,\ s,\ o}$	shear moduli of film, substrate, oxide (N/m^2)
ν	Poisson's ratio
ρ	density (kg/m^3)
	also: dislocation density ($1/m^2$)
	also: specific resistivity (Ohms m)
$\tilde{\rho}$	effective mobile dislocation density ($1/m^2$)
ρ_{source}	dislocation source density ($1/m^3$)
σ	average film stress (N/m^2)
	also: lognormal standard deviation
σ^*	effective stress (N/m^2)
σ_0	intragranular stress (N/m^2)
σ_{gb}	average normal traction on grain boundary (N/m^2)
σ_n	normal stress component on grain boundary (N/m^2)

σ_y	yield stress (N/m^2)
σ_μ	athermal yield stress component (N/m^2)
τ	shear stress (N/m^2)
$\hat{\tau}$	athermal flow stress (N/m^2)
ξ	coordinate of internal oxidation front (m)
	also: integration parameter
ζ	integration parameter
Ω	atomic volume (m^3)